UNIVERSITÉ DU QUÉBEC À MONTRÉAL

THÈSE PRÉSENTÉE À L'UNIVERSITÉ DU QUÉBEC À CHICOUTIMI
COMME EXIGENCE PARTIELLE
DU DOCTORAT EN RESSOURCES MINÉRALES
OFFERT À
L'UNIVERSITÉ DU QUÉBEC À MONTRÉAL
EN VERTU D'UN PROTOCOLE D'ENTENTE AVEC
L'UNIVERSITÉ DU QUÉBEC À CHICOUTIMI

PAR

ALEXANDRE BEAULIEU

PROPRIÉTÉS INVARIANTES D'ÉCHELLE ET ANISOTROPES DE MORPHOLOGIES D'ÉROSION FLUVIATILE

MAI 2004

Bibliothèque
Paul-Émile-Boulet

UQAC
Université du Québec
à Chicoutimi

Mise en garde/Advice

Afin de rendre accessible au plus grand nombre le résultat des travaux de recherche menés par ses étudiants gradués et dans l'esprit des règles qui régissent le dépôt et la diffusion des mémoires et thèses produits dans cette Institution, **l'Université du Québec à Chicoutimi (UQAC)** est fière de rendre accessible une version complète et gratuite de cette œuvre.

Motivated by a desire to make the results of its graduate students' research accessible to all, and in accordance with the rules governing the acceptation and diffusion of dissertations and theses in this Institution, the **Université du Québec à Chicoutimi (UQAC)** is proud to make a complete version of this work available at no cost to the reader.

L'auteur conserve néanmoins la propriété du droit d'auteur qui protège ce mémoire ou cette thèse. Ni le mémoire ou la thèse ni des extraits substantiels de ceux-ci ne peuvent être imprimés ou autrement reproduits sans son autorisation.

The author retains ownership of the copyright of this dissertation or thesis. Neither the dissertation or thesis, nor substantial extracts from it, may be printed or otherwise reproduced without the author's permission.

UNIVERSITÉ DU QUÉBEC À MONTRÉAL

THESIS PRESENTED AT UNIVERSITÉ DU QUÉBEC À CHICOUTIMI
AS A PARTIAL REQUIREMENT
OF MINERAL RESSOURCES DOCTORATE
OFFERED TO
UNIVERSITÉ DU QUÉBEC À MONTRÉAL
IN ACCORDANCE TO AN AGREEMENT PROTOCOL WITH
UNIVERSITÉ DU QUÉBEC À CHICOUTIMI

BY

ALEXANDRE BEAULIEU

SCALING AND ANISOTROPIC PROPERTIES OF EROSIONAL LANDFORMS

MAI 2004

REMERCIEMENTS

Je remercie avant tout ma directrice de thèse Hélène Gaonac'h, qui par son soutien, ses précieux conseils et ses encouragements, m'a permis de mener à terme cet ouvrage. La formation scientifique qu'elle m'a donnée est d'une grande qualité et me sera utile tout au long de ma carrière de chercheur. Je remercie également Jean-Claude Mareschal, qui m'a offert un soutien en tant que co-directeur, sur l'analyse statistique et la programmation informatique. Je suis aussi très reconnaissant envers Shaun Lovejoy pour sa collaboration au niveau de la partie théorique de cette étude.

Je remercie les membres de mon jury, Claude Hillaire-Marcel, Alessandro Forte et Jeffrey K. Weissel d'avoir bien voulu accepter de réviser cette thèse. Merci aux gens du laboratoire de géophysique, Chantal Gosselin, Pascal Audet, Jean-François Leclerc-Cloutier et Roxanne Gratton, et tout particulièrement à Evelise Bourlon, qui m'a souvent donné des conseils à plusieurs niveaux, et à Dany Harvey pour ses conseils informatiques et pour m'avoir aidé au début de ma thèse. Merci à tous les gens du GEOTOP que je n'ai pas nommés. Je remercie aussi Jean-François Hélie, Guillaume St-Onge et André Poirier pour leurs encouragements soutenus tout au long de mon séjour au GEOTOP et pour leur amitié. Merci à tous mes amis pour leur soutien moral.

Un gros merci à ma famille pour son appuie tout au long de cette aventure. Je tiens à remercier de tout mon cœur ma copine, Véronique Drouin, pour son amour immense, son soutien inconditionnel et pour avoir cru en moi. Je lui dédie cette thèse, à elle et à l'enfant qu'elle porte.

Enfin, j'exprime toute ma gratitude au FCAR, au CRSNG, au GEOTOP et à l'UQÀM pour le soutien financier qu'ils m'ont fourni.

Table des matières

Remerciements iii

Table des matières iv

Liste des tableaux vii

Liste des figures viii

Résumé xi

Abstract xiii

Introduction générale 1

1. Introduction 1

2. Problématique 3
   2.1 L'invariance d'échelle 3
   2.2 L'anisotropie invariante d'échelle 6

3. Objectifs 9

4. Description des chapitres 10
   4.1 Chapitre 1 10
   4.2 Chapitre 2 11
   4.3 Chapitre 3 12

5. Conclusions 13

Références 15

Chapitre I 19
Scaling of differentially eroded surfaces in the drainage network of the Ethiopian plateau ....

Abstract 20

1. Introduction 21

2. Area description, data set and method 26
   2.1. Geological setting 26

    2.2. Remotely sensed data 27

  3. Results 28
    3.1. Power spectrum 28
    3.2. Multifractal analysis 30

  4. Discussion 33

  5. Conclusion 37

  Acknowledgements 40

  References 41

Chapitre II 59
  Scale-invariant anisotropy investigation of remotely sensed images of river networks .....

  Abstract 60

  1. Introduction 61

  2. The data 65

  3. Methodology 68

  4. Results 74

  5. Discussion 78

  6. Conclusion 81

  References 84

Chapitre III 100
  Quantification of the anisotropic behaviour with scale: a new way to characterize surface morphologies .....

  References 109

Conclusions générales 117

  Références 122

Appendice A: Méthodologie 123

Appendice B: CD-ROM 126

Glossaire 128

Liste des tableaux

Chapitre I

Table 1. Spectral characteristics of the Landsat TM sensor....45
Table 2. Power spectrum analysis results....46
Table 3. Multifractal analysis results....47

Chapitre II

Table 1. Averaged estimates of the statistical scaling parameters of the analyzed images and their error....90

Liste des figures

Chapitre I

Figure 1. Geological map of Ethiopia (modified from Mhor and Zanettin, 1988) showing the location of the Landsat TM image (large square) and the ERS-1 image (small square) 50

Figure 2. Subsections of the Landsat TM image, BNC and PLA areas. The image is a color-composite of bands 3, 4 and 5 51

Figure 3. BNC and plateau PLA represented by different remotely sensed images. (a) Landsat TM2 BNC, (b) ERS-1 BNC, (c) Landsat TM2 PLA, and (d) ERS-1 PLA. Landsat images are enhanced for a better visualisation 52

Figure 4. Power spectrum analyses for the Landsat and ERS-1 data sets over the BNC and PLA areas. ○ =ERS-1 BNC with a slope (β)=0.55, ●= ERS-1 PLA with a slope(β)=0.20, ∇ =Landsat TM2 BNC with a slope(β)=0.94 and +=Landsat TM2 PLA with a slope(β)=0.36 53

Figure 5. Plot of the substraction of SWIR and VIS spectrum for BNC and PLA areas. ◊=Landsat TM7-TM2 PLA and ■=Landsat TM7-TM2 BNC. For PLA and BNC, slopes are 0.48 and 0.17, respectively, and the correlation coefficients 0.91 and 0.97, respectively 54

Figure 6. Plot of SWIR versus VIS β values for 256 by 256 pixels subsections of BNC (Δ) and PLA (▼) areas 55

Figure 7. $\langle(\varepsilon_\Lambda^\eta)_\lambda^q\rangle$ versus $\log_{10}(\lambda)$ for various η values and for q=2 for Landsat TM5 BNC area. For each η value, we observe a linear trend in the $\log_{10}$-$\log_{10}$ diagram. The scaling in each case is exhibited from 120 m (λ=256) to 30 km (λ=1). Δ η=2.00, ◊ η=1.58, × η=1.26, ○ η=1.00 56

Figure 8. Plot of $\log_{10}|K(2,\eta)|$ versus $\log_{10}\eta$ for Landsat TM5 BNC area, exhibiting universal multifractality over approximately η=0.04 and η=1. The slope α= 1.91. 57

Figure 9. Landsat TM5/TM7-ratioed images (similar enhancement) of BNC and PLA areas showing the relative content and distribution of clay minerals 58

Chapitre II

Figure 1. a) Location of the two selected regions in the Loess Plateau of China. The ASTER flight over the Yellow River (Huang He River) contains 8 scenes, overall representing 60 km by 485 km; the CL and CY images were chosen in this section. The other ASTER flight is partly on the Taihang Mountains and is made of 5 scenes, overall representing 60 km by 304 km; the CM images were taken from this area. Map is modified after Derbyshire (2001). b) Location of the Utah data set (UT). The dark rectangle shows portion of the ASTER flight, which is composed of 3 scenes, and is 60 km by 184 km. Map modified after Dickinson et al. (1985)..93

Figure 2. Examples of the drainage pattern in each data groups. (a) the CL group containing 17 images, the ASTER data have been collected on October 1, 2000. (b) CY group containing 5 images, same ASTER scenes as (a). (c) the CM group containing 16 images, the ASTER data have been collected 10, 2001. (d) the UT group containing 7 images, the ASTER scenes were acquired on October 19, 2000. Each image is 512 by 512 pixels and is 15.36×15.36 km^2.........94

Figure 3. Example of the fitted contours in a CY FT image. The contours shown at the bottom is a magnification of the small square in the top image. In a FT image, the small structures are depicted by the large contours, and the large ones by the small contours; they are also orthogonal to the real structures............95

Figure 4. Plot of $\log_{10} E(k)$ versus $\log_{10} k$ for selected images of each group, they are shifted for a better visualization, see table 1 for average β values............96

Figure 5. Plot of $\zeta(l)$ versus the scale log of the scale l for the FT and SF methods on the four different image groups (UT, CM, CL and CY) (120 meters corresponds to $\ln(l)$=4.7)..97

Figure 6. a) Plot of ζ_1 values versus the β values estimated from the FT method for the different groups. The large symbols represent the averaged values of each field. b) Plot of θ_1 values (in radians) versus the β values estimated from the FT method for the different groups..98

Figure 7. Plot of ζ(960 m)values versus the β values estimated from the FT method for the different data ensembles..99

Chapitre III

Figure 1. Images chosen, "canyon" and "plateau", on the Landsat TM scene acquired on January 5, 1985, with solar elevation of 42° and azimuth angle of

134°. The scene is a color-composite of bands 3, 4 and 5. The size of subset is 1024 by 1024 pixels, which is about 30 km square. Images chosen on TERRA ASTER scenes, acquired on June 11, 2001, with solar elevation of 60° and azimuth angle of 149°are of the same size and resolution (averaged form initial resolution of 15 meters). 113

Figure 2. (**a**) The two-dimensional spectral density (FT) of Landsat TM canyon area in the SWIR spectrum range. In this Fourier image, the large structures are represented in the center and are orthogonal to ones in the real space. The graph (**b**) represent the isotropic analysis of the FT, the isotropic energy spectrum log($E(k)$) versus log (k), the slope being β [$E(k) \propto k^{-\beta}$]. In the image, two circles ("balls") are drawn (A and B), their energy density is represented in the graph to demonstrate the scale representation of these isotropic "balls" on which the values are ensemble-average.......... 114

Figure 3. Contours drawn on the FT (**a**) and the SF (**b**) images of the Landsat TM plateau area in the SWIR spectrum range. The figure **c** and **d** are the contours drawn in the respective zooms of **a** and **b** (white square). In **a**, only the structures from 30 to 360 meters in size are represented; in **b** the exhibited structures are from 2190 to 12690 meters. The zooms **c** and **d** are representing respectively the structures 360 to 15360 meters from **a** and 30 to 2190 meters from **b**.......... 115

Figure 4. The four diagrams show the variation of ellipticity ($\zeta(l)$) versus the scale/size of the structures $ln(l)$. The values obtained for the extra TERRA ASTER data sets for the canyon area are $\zeta_1 = 0.13, 0.16$ for FT VIS and SWIR and $\zeta_1 = 0.17, 0.15$ for SF VIS and SWIR. The values for the TERRA ASTER plateau area are $\zeta_1 = 0.09, 0.24$ for FT VIS and SWIR and $\zeta_1 = 0.13, 0.22$ for SF VIS and SWIR. 116

RÉSUMÉ

Les propriétés statistiques invariantes d'échelle isotropes et anisotropes de morphologies terrestres d'érosion fluviatile ont été caractérisées dans cette étude à l'aide d'images satellitaires. En premier lieu, les propriétés invariantes d'échelle isotrope de différentes sections du réseau de drainage du Plateau éthiopien ont été déterminées à partir d'images de régions spectrales variées des satellites Landsat TM 5 et ERS-1. Ensuite, une méthode a été développée pour évaluer les propriétés anisotropes invariantes d'échelle de surfaces d'érosion fluvio-tectonique. Deux types de réseau de drainage ont alors été choisis: le réseau de la Rivière Jaune sur le Plateau de Lœss en Chine et celui de la Green River dans le Utah aux États-Unis. Dans cette deuxième partie, des images du visible du satellite TERRA ASTER ont été analysées. Enfin, la méthode de caractérisation de l'anisotropie indépendante de l'échelle a été appliquée sur les données du Plateau éthiopien afin de mieux y cerner les processus impliqués; les données satellitaires Landsat TM 5 et TERRA ASTER ont été utilisées pour cette partie de la recherche.

Les deux régions sélectionnées sur le Plateau éthiopien, "plateau" et "canyon", possèdent des degrés d'érosion très différents. Une première distinction des propriétés invariantes d'échelle isotropes a été trouvée à l'aide d'images Landsat TM 5 dans le visible et d'images ERS-1 dans les micro-ondes. Cette différence a été liée au degré d'érosion mécanique entre ces deux régions, "plateau" (peu érodé) et "canyon" (très érodé). Une deuxième différence statistique a été révélée par les analyses d'invariance d'échelle isotrope des images Landsat TM 5 dans l'infrarouge moyen, qui sont plus sensibles aux argiles. Cette distinction est associée à la présence d'une couche d'altération des minéraux sur le "plateau", couche qui n'est pas retrouvée dans la région "canyon" à cause de l'érosion mécanique plus importante. Ainsi, ces analyses statistiques révèlent la présence active de deux processus distincts agissant sur le Plateau éthiopien, soit l'érosion mécanique et l'érosion chimique.

L'étude de l'anisotropie sur des images de réseaux fluviaux a permis de trouver des différences statistiques significatives entre les différents réseaux de drainage. Les analyses de l'anisotropie montrent aussi que celle-ci doit être caractérisée dans un cadre d'invariance d'échelle. Les analyses d'invariance d'échelle isotrope (paramètre β) permettent de différencier les images très dendritiques (densité de drainage très élevée) du réseau de drainage du Plateau de Loess chinois des autres images moins densément dendritiques. Cependant, elles ne donnent pas la possibilité de distinguer les images du Utah de celles de la Chine où l'érosion est plus poussée et

les réseaux plus développés. Dans ce cas, les propriétés anisotropes distinctes reliées aux différentes lithologies des régions permettent de les différencier. De plus, l'anisotropie invariante d'échelle permet de distinguer les images de différentes parties d'un même réseau, par exemple le Plateau de Loess chinois, qui présente des contrastes associés au degré de maturité (ou au développement) du réseau et aux différences lithologiques et structurales régionales. Les analyses effectuées sur l'anisotropie du réseau de drainage du Plateau éthiopien ont confirmé les différences associées aux processus d'érosion et d'altération chimique des sols.

Dans l'ensemble, cette étude montre la portée de l'utilisation des images satellitaires en relation avec les analyses d'invariance d'échelle sur les champs de données. Les analyses statistiques anisotropes des structures sur une grande gamme d'échelles complémentent de façon adéquate les analyses isotropes. La méthode développée dans cette étude est d'utilisation relativement simple et pourrait fournir une caractérisation quantitative plus systématique échelle par échelle des surfaces terrestres et des processus dynamiques sous-jacents.

ABSTRACT

The isotropic and anisotropic scale invariant statistical properties of erosional landforms were characterized in this study with remote sensing images. Firstly, the isotropic scale invariant properties of different sections of the Ethiopian Plateau were analyzed in images of various spectral ranges from the satellites Landsat TM 5 and ERS-1. A method was then developed for characterizing the scale invariant anisotropic properties of fluvio-tectonical erosional surfaces. Two types of drainage network have been chosen: the Yellow River network on the Loess Plateau in China and the Green River network in Desolation Canyon in Utah, USA. In this case, images in the visible spectrum from the TERRA ASTER satellite were used for the analyses. Finally, the method developed for the characterization of anisotropy was applied to the Ethiopian Plateau data in order to better understand the involved processes. In this case, Landsat TM 5 and TERRA ASTER data were used in this case.

The two regions selected on the Ethiopian Plateau, "plateau" and "canyon", possess very different erosion degrees. A first distinction between the isotropic scale invariant properties was found with the Landsat TM images in the visible and also with ERS-1 in the microwave. This difference was linked to the variation in the mechanical erosion degree between the two regions, "plateau" (less eroded) and "canyon" (more eroded). A second difference between the regions was revealed by the isotropic scale invariant analyses of Landsat TM 5 images in shortwave infrared length, which are more sensitive to clay minerals. This second distinction is associated to the presence of a mineral alteration layer on the "plateau", layer that is not found in the "canyon" region because of the more intense mechanical erosion in this area. Hence, these statistical analyses reveal the presence of two active processes acting differentially on the Ethiopian Plateau: mechanical erosion and chemical erosion.

The investigation of anisotropy on images of river networks permitted the finding of significant statistical differences between the different drainage networks. The analyses of anisotropy also showed that it must be characterized in the scale invariant framework. Isotropic scale invariant analyses (β values) allow the differentiation of the very dendritic (very high drainage density) images of the Chinese Loess Plateau from the other less densely dendritic images. However, they do not allow the distinction of images of Utah from those of China where the erosion is more advanced and the networks are more matures. In this case, these regions must be differentiated using the distinct anisotropic properties linked to the different lithologies of the respective regions. Moreover, the scale invariant anisotropy allows to distinguish images from different parts of the same network, such as the Chinese Loess Plateau, which shows contrasts linked to the degree of maturity (or to the level of development) of the network and to regional lithological and structural differences. The analyses on anisotropy made on the drainage network of the Ethiopian Plateau have confirmed the differences associated to mechanical erosion and chemical alteration of soil processes.

Overall, this study demonstrates the impact of using remote sensing data together with scale invariant analyses on data fields. Anisotropic statistical analyses of structures over a wide range of scales usefully complement the isotropic analyses. The method developed in this study is relatively simple to use, and could give a more systematic "scale by scale" quantitative characterization of terrestrial surfaces and the underlying dynamical processes.

Introduction générale

1. Introduction

L'existence de structures géologiques complexes et la variabilité des champs de données en géophysique ont poussé à considérer comme incontournable l'aspect non linéaire des mécanismes dynamiques sous-jacents agissant sur une grande gamme d'échelles. Les différentes morphologies et structures, caractérisant la surface terrestre, résultent de phénomènes naturels produisant des changements extrêmes dans l'espace et dans le temps. Cette variabilité aboutit à des événements catastrophiques tels des inondations, des ouragans, des raz-de-marée, des éruptions volcaniques, etc. Une caractéristique fondamentale de la variabilité est qu'elle se produit sur une grande gamme d'échelles allant du millimètre à des milliers de kilomètres selon le phénomène observés. L'approche standard considère l'homogénéité des processus et/ou de la variabilité; par exemple, autour d'une valeur moyenne, à une seule échelle, alors que la variabilité même des phénomènes change selon la résolution d'observation (Schertzer and Lovejoy, 1995). L'objectif est donc de trouver des caractéristiques indépendantes de l'échelle d'observation.

Les morphologies terrestres et les processus qui en sont responsables tels que la tectonique des plaques, le volcanisme, l'érosion et la sédimentation ont souvent fait l'objet de modèles incorporant des lois d'invariance d'échelle ("scaling" et "multiscaling") (e.g., Chase, 1992; Turcotte, 1997; Pelletier, 1999). L'étude de la géométrie et des propriétés invariantes d'échelle des réseaux fluviatiles est particulièrement riche dans la littérature scientifique (e.g., Tarboton et al., 1988; La

Barbera et Rosso, 1989; Dodds et Rothman, 2000). La topographie est un champ de données qui a aussi fait l'objet d'investigations sur ces propriétés statistiques (Lavallée et al., 1993; Weissel et al., 1994; Pecknold et al., 1997; Veneziano et Iacobellis, 1999). Les données télédétectées sont bien adaptées à l'étude de la surface de la Terre et tout particulièrement sa topographie variable et ses structures complexes. Les données télédétectées permettent d'obtenir plusieurs représentations de la même région terrestre à l'aide des régions du spectre électromagnétique. Elles donnent la possibilité de quantifier les différentes propriétés d'une morphologie donnée: la topographie, l'albédo, l'humidité, la végétation, la composition des sols, le type de lithologie, la chaleur de la surface, la rugosité de la surface, etc. Cependant, ces caractéristiques doivent être interprétées avec précaution. La présence de zones urbaines pourrait par exemple biaiser des analyses statistiques. Des variations importantes de types de végétation, de lithologie, de conditions d'ensoleillement, de conditions atmosphériques sont toutes autant de causes possibles d'interprétations biaisées voire erronées. C'est pourquoi il est important de connaître ces limites pour bien choisir en conséquence les images à analyser. Dans la présente étude, nos efforts ont porté à sélectionner des images satellitaires dans des régions lithologiques homogènes avec peu de végétation et de zones urbaines. Peu d'études ont porté sur l'utilisation des données télédétectées pour la caractérisation des propriétés statistiques invariantes d'échelle des différentes morphologies terrestres, et particulièrement celles résultant des processus d'érosion fluviatile. De plus, les paramètres statistiques, tels que la dimension fractale, obtenus sur ces surfaces, sont rarement utilisés dans un but de distinction des différentes morphologies et des processus associés et auraient avantage à être exploités dans ce sens.

Enfin, l'orientation préférentielle des structures observées dans la nature est très peu étudiée en lien avec les échelles impliquées. Cet aspect anisotrope des structures fait pourtant partie intégrante de l'évolution dynamique des mécanismes sous-jacents. Un cours d'eau par exemple se développe suivant un réseau de fracture orienté s'il le peut plutôt que d'évoluer dans toutes les directions. Il a été démontré par Schertzer et Lovejoy (1985) et Lovejoy et Schertzer (1985) que l'anisotropie peut être incluse dans les lois de "scaling" et de "multiscaling".

2. Problématique

2.1 L'invariance d'échelle

Le principe de l'invariance d'échelle fait appel à une hypothèse de base selon laquelle les processus dynamiques non linéaires se répètent sur une gamme d'échelles plus ou moins grande et produisent des morphologies à toutes les échelles. Une telle hypothèse implique une symétrie invariante d'échelle; les structures de toutes tailles (petites, moyennes et grandes) ont des points en commun, elles font partie d'une même famille. Les paramètres physiques décrivant ces processus tels que l'élévation, l'intensité d'albédo et le rayonnement infrarouge thermique sont alors des lois de puissance en fonction la résolution spatiale; les exposants de ces lois sont invariants d'échelle, donc indépendants de l'observateur (Laferrière et Gaonac'h, 1999). Si l'on a établi la loi de puissance, la seule connaissance de la résolution d'intérêt permet d'en déduire le paramètre recherché à cette résolution. La caractérisation de lois dites fractales sur des ensembles géométriques consiste à représenter la variation de mesures (longueurs, périmètres ou aires) en fonction de la résolution. Dans le cas d'un champ de données comme une image satellitaire, où plusieurs niveaux d'intensité existent, beaucoup de dimensions fractales peuvent être trouvées selon le seuil imposé. L'analyse multifractale est mieux adaptée pour la détermination des paramètres des lois invariantes d'échelle des champs de données. Dans ce cas, l'exposant est une équation invariante d'échelle évoluant en fonctions des statistiques.

Plusieurs études, sans toutes les nommer, sur les caractéristiques fractales orientées dans diverses branches des sciences de la Terre ont été effectuées depuis l'avènement de cette nouvelle notion développée par Mandelbrot (1967). Les réseaux de drainage ont fait l'objet de beaucoup d'études fractales sur leur forme et leur distribution (i.e., Tarboton et al., 1988; Tarboton, 1996; Claps et Oliveto, 1996). Les volcans ont été étudiés pour la morphologie de leurs laves (Gaonac'h et al., 1992; Bruno et al., 1994) et pour d'autres aspects. La dimension fractale de différents réseaux de fracture a été estimée (Vignes-Adler et al., 1991). Et encore d'autres sujets tels que la sismicité, la sédimentation, la porosité des roches et les concentrations de minerais ont été montrés comme possédant des lois invariantes d'échelle sur des gammes d'échelles assez grandes. Plus récemment, l'approche multifractale a été employée pour caractériser divers champs de données télédétectées. Des comportements "multiscaling" ont été trouvés dans les champs de réflexion de la partie visible du spectre électromagnétique sur des volcans basaltiques (Laferrière et

Gaonac'h, 1999). Des propriétés multifractales ont été attribuées aux champs thermiques des zones actives du volcan Kilauea (Harvey et al., 2002; Gaonac'h et al., 2003). La couleur de l'océan a été étudiée pour ces propriétés multifractales (Lovejoy et al., 2001).

La topographie constitue un des éléments importants de plusieurs études. Que ce soit pour son intégration dans des systèmes géographiques informatisés (SGI) ou pour des études sur l'évolution temporelle des réseaux de drainage et des diverses morphologies de surfaces terrestres ou extraterrestres, il est nécessaire que les propriétés de "scaling" et/ou "multiscaling" de la topographie soient utilisées dans ces études afin d'être intégrées dans un cadre plus cohérent. Dans les études du comportement invariant d'échelle de la topographie, et ce jusqu'à tout récemment, les modèles numériques d'élévation (MNE) étaient employés (e.g., Mark et Aronson, 1984; Huang et Turcotte, 1989; Chase, 1992). Ces MNE sont souvent dérivés par stéréoscopie à partir d'image satellitaires ou aériennes. Exceptées deux études sur le Rift Est-Africain (Weissel et al., 1994; Weissel et al., 1995), peu d'auteurs se sont intéressés aux différences possibles des paramètres fractals ou multifractals sur divers types de morphologie de surface pouvant exprimer une dominance de l'érosion, de la sédimentation, du tectonisme ou du volcanisme.

Weissel et al. (1995) ont étudié les propriétés statistiques ("scaling") de la topographie de différentes régions du Plateau éthiopien présentant des degrés d'érosion variables à l'aide de MNE. Ils ont trouvé une différence entre les dimensions fractales d'une portion de plateau très peu érodée, et le canyon, où l'érosion est avancée. Ils soulèvent l'hypothèse que des lois "multiscaling" seraient peut-être plus appropriées à l'étude de tels phénomènes. Est-ce que l'utilisation de données télédétectées telles que les images satellitaires est appropriée pour ce type d'étude? Quelle pourrait être la contribution apportée par l'utilisation des différentes régions du spectre électromagnétique dans l'analyse de l'invariance d'échelle? Y a-t-il des différences entre les propriétés statistiques des morphologies terrestres produites par différents satellites? À l'aide de données télédétectées des satellites Landsat TM 5 et ERS-1, et d'une approche fractale et multifractale, les propriétés statistiques des surfaces analysées dans différentes régions spectrales (visible, infrarouge moyen, micro-onde) seront recherchées dans le but de comprendre l'évolution possible de l'invariance d'échelle en fonction des longueurs d'ondes spectrales.

2.2 L'anisotropie invariante d'échelle

L'anisotropie, l'orientation préférentielle d'éléments ou de structures, est une caractéristique couramment remarquée dans les morphologies naturelles ou artificielles, que ce soit à l'échelle de l'arrangement cristallin de la surface d'une roche ou bien à l'échelle des structures majeures de dimension planétaire. Sa caractérisation peut se faire par exemple en mesurant l'élongation d'un ou plusieurs éléments; on peut aussi mesurer une orientation préférentielle des structures. De telles mesures se font habituellement à une échelle donnée. Alternativement, la caractérisation de l'invariance d'échelle se fait, elle, de manière isotrope (autosimilaire), impliquant que le système analysé possède des propriétés équivalentes dans toutes les directions et à toutes les échelles. Une façon d'inclure l'anisotropie dans l'invariance d'échelle peut ce caractériser telle qu'une transformation de la structure sur une gamme d'échelle différente selon la direction considérée; par exemple un aplatissement des structures dans un sens et un allongement dans l'autre sens. Ce type de détermination de l'invariance d'échelle, appelé autoaffine, est souvent insuffisant car des variations de l'anisotropie avec l'échelle peuvent se présenter sous forme de modifications beaucoup plus complexes incluant la stratification différentielle et la rotation différentielle des structures. Le besoin d'inclure de telles transformations dans un cadre d'invariance d'échelle a conduit au développement du formalisme de l'invariance d'échelle généralisée (GSI) (Lovejoy et Schertzer, 1985; Schertzer et Lovejoy, 1985).

À l'intérieur d'un cadre d'analyse GSI, les transformations d'échelles anisotropes sont contenues dans un générateur, une matrice de dimension 2 dans le cas d'une surface, qui agit sur l'échelle en loi de puissance et la transforme selon les paramètres décrivant la contraction, la stratification et la rotation. Une sphéro-échelle (échelle à laquelle les statistiques sont isotropes) est identifiable dans le système étudié; celle-ci permet de comparer de façon relative les échelles entres-elles. Quand le générateur est la matrice identité, le scaling est isotrope (même transfromation des vecteurs dans toutes les directions). Si le générateur prend la forme d'une matrice diagonale, cela équivaut au cas autoaffine. Par contre, quand la matrice contient des éléments hors diagonale, les structures changent d'orientation (rotation) et de forme (élongation, stratification des structures, aplatissement) avec l'échelle (Lovejoy et al., 2001).

À l'aide du GSI, des études faites sur des images satellitaires de nuage ont démontré la présence d'anisotropie invariante d'échelle (Lovejoy et al., 1992; Pflug et al., 1993). Pecknold et al. (1997) ont établi l'importance d'étudier l'anisotropie dans un cadre d'invariance d'échelle avec différents types de données (topographie, nuages, anomalies aéromagnétiques et glace marine). Lovejoy et al. (2001) et Pecknold et al. (2001) montrent aussi la portée de ce type d'investigation sur les champs magnétiques terrestres, difficilement descriptible par les méthodes "scaling" conventionnelles. Dans l'étude des surfaces terrestres, peu d'analyses ont été effectuées sur l'anisotropie nonlinéaire. Weissel et al. (1994) ont remarqué une différence entre les statistiques unidimensionnelles de profils topographiques en Éthiopie. Une expérience en laboratoire sur une rivière en tresse a aussi montré une distinction directionnelle du "scaling" (Foufoula-Georgiou et Sapozhnikov, 1998). Les réseaux fluviaux donnent souvent des résultats statistiques invariants d'échelle isotropes similaires, tel que démontrées par Pelletier (1999). Les propriétés anisotropes permettront-elles de les distinguer?

À partir d'images du satellite TERRA ASTER, sélectionnées sur divers réseaux de drainage terrestres, les propriétés invariantes d'échelle isotropes et anisotropes seront recherchées dans la région du visible du spectre électromagnétique. L'interprétation des résultats nous permettra de distinguer les processus sous-jacents.

La méthode créée dans la présente étude sera ensuite appliquée sur les images de l'Éthiopie acquises dans différentes régions du spectre électromagnétique.

3. Objectifs

Les questions et problèmes suscités par la problématique seront évalués en deux étapes. Les propriétés "scaling" et "multiscaling" du réseau de drainage sur le Plateau éthiopien seront étudiées à l'aide d'images satellitaires de longueurs d'ondes variées dans un premier volet. Le deuxième volet concernera l'aspect anisotrope invariant d'échelle des structures observées sur divers réseaux fluviaux. Les principaux objectifs sont établis ainsi:

"Scaling" et "multiscaling":

1) Caractérisation du "scaling" à l'aide de spectre d'énergie en espace Fourier sur des sections d'images satellitaires possédant des degrés d'érosion variables sur le Plateau éthiopien (satellites tels que Landsat TM 5 et ERS-1, utilisation des diverses régions spectrales).
2) Recherche des propriétés "multiscaling" de ces mêmes images.
3) Établissement de liens entre les processus responsables (e.g., érosion, sédimentation, météorisation) et les paramètres découlant des analyses statistiques.

Anisotropie invariante d'échelle:

4) Création d'une méthode directe d'analyse de l'anisotropie invariante d'échelle à l'aide des principes fondamentaux du GSI à partir d'analyse en

deux dimensions en espace Fourier et en espace réel (fonctions de structures en 2D).

5) Caractérisation de l'anisotropie invariante d'échelle d'images satellitaires (TERRA ASTER) par la méthode décrite ci-haut dans la région spectrale du visible (0.63-0.69 μm), de divers réseaux fluviaux possédant des attributs distinctifs.
6) Interprétation des propriétés trouvées par les analyses de l'anisotropie des morphologies observées.
7) Enfin, à partir de la méthode développée pour la recherche d'anisotropie, la caractérisation des propriétés anisotropes invariantes d'échelle du réseau de drainage éthiopien sera effectuée dans deux régions du spectre électromagnétique, le visible (0.52-0.60 μm) et l'infrarouge moyen (1.55-1.75 μm et 1.60-1.70 pour Landsat TM 5 et TERRA ASTER respectivement).

Les divers éléments décrits seront présentés dans la thèse sous forme de trois articles, les chapitres 1, 2 et 3.

4. Descriptions des chapitres

4.1 Chapitre 1

"Scaling of differentially eroded surfaces in the drainage networks of the Ethiopian Plateau."

Invariance d'échelle de surfaces différentiellement érodées du réseau de drainage du Plateau éthiopien.

La partie "scaling" et "multiscaling" a été abordée à l'intérieur de ce chapitre présenté sous forme d'article. Il a été rédigé en étroite collaboration avec la professeure Hélène Gaonac'h, directrice de la présente thèse. Cet article a été publié dans la revue scientifique "Remote Sensing of Environment" (Vol. 82, 111-122, 2002). Dans cet article, il est démontré que les images analysées, des sections d'images des satellites Landsat TM5 et ERS-1 du réseau de drainage du Plateau éthiopien, sont invariantes d'échelle et qu'elles possèdent aussi des propriétés multifractales ("multiscaling"). Nous avons montré qu'il y a des distinctions des paramètres statistiques "scaling" entre les parties plus érodées et celles moins érodées mécaniquement. De plus, une distinction supplémentaire est établie entre les surfaces peu érodées (plateau) observées dans le spectre du visible et de l'infrarouge moyen, différence non soulevée pour les parties présentant un degré d'érosion avancé (canyon). Des interprétations concernant les processus responsables, c'est-à-dire l'érosion mécanique et l'érosion chimique (altération créée par les intempéries), sont avancées pour expliquer les distinctions établies par les analyses d'invariance d'échelle sur les différentes morphologies observées.

4.2 Chapitre 2

"Scale-invariant anisotropy investigation of remotely sensed images of river networks"

Recherche de l'anisotropie invariante d'échelle d'images télédétectées de réseaux fluviaux.

À l'intérieur de ce chapitre, il est question de la caractérisation de l'aspect anisotrope des structures et textures dans un cadre d'invariance d'échelle. Ce chapitre, présenté sous forme d'article, a été écrit en collaboration avec Hélène Gaonac'h et avec Shaun Lovejoy de l'Université McGill. Il sera soumis dans les mois suivants le dépôt de la thèse à la revue "Journal of Geophysical Research". Dans cet article, l'importance de la caractérisation de l'anisotropie des structures et des textures présente dans la nature dans un cadre d'invariance d'échelle est démontrée. Pour ce faire, la théorie du GSI (invariance d'échelle généralisée) développée par Lovejoy et Schertzer (1985) et Schertzer et Lovejoy (1985) est appliquée. Des images satellitaires (TERRA ASTER) de deux réseaux de drainage différents, le Plateau de Loess, en Chine, et le Desolation Canyon, dans l'Utah, USA, sont analysées. Nous démontrons que pour les régions étudiées, l'anisotropie peut être caractérisée dans le cadre du GSI et qu'elle est invariante d'échelle (comportement log-linéaire). Nous montrons aussi qu'il y a des distinctions des propriétés invariantes d'échelle isotropes et anisotropes entre les deux réseaux de drainage, et nous les expliquons dans un cadre contextuel (géologies, lithologies et tectoniques différentes).

4.3 Chapitre 3

"How to quantify anisotropic features spreading over a large range of scales?"

Comment quantifier des morphologies anisotropes s'étendant sur une grande gamme d'échelles?

Dans ce chapitre, nous appliquons la méthode développée pour caractériser l'anisotropie dans un cadre d'invariance d'échelle sur les données du Plateau éthiopien. Ce chapitre est aussi présenté sous forme d'article, écrit avec Hélène Gaonac'h et avec Shaun Lovejoy de l'Université McGill. Il sera envoyé dans les mois suivants le dépôt de la thèse à la revue "Nature". Dans cette étude, différentes images satellitaires sont utilisées (Landsat TM 5 et TERRA ASTER) sur des régions possédant des degrés d'érosion très différents, portion de plateau peu érodée et canyon où l'érosion est avancée. Cette étude suit celle du chapitre 1; les propriétés statistiques de ces régions sont aussi recherchées dans différentes régions du spectre électromagnétique (visible et infrarouge moyen). Nous démontrons dans cet article l'importance de la caractérisation de l'anisotropie invariante d'échelle pour aider à distinguer les différents processus responsables des morphologies observées.

5. Conclusions

Enfin, il est important de mentionner que la contribution que j'ai apportée à la production de l'article publié (chapitre 1), ainsi que sur ceux en préparation et co-rédigés avec ma directrice de recherche, Hélène Gaonac'h, et le professeur Shaun Lovejoy, est majeure. J'ai tout particulièrement travaillé sur l'écriture de programmes informatiques et développé de nouvelles méthodes d'analyses. J'ai travaillé en étroite collaboration avec Hélène Gaonac'h en proposant de nouvelles interprétations statistiques et géologiques. La collaboration avec Shaun Lovejoy a reposé principalement sur le développement des outils statistiques du GSI en lien avec la théorie. Le professeur Jean-Claude Mareschal m'a apporté un soutien administratif et m'a aussi fourni des conseils au niveau des analyses statistiques et de la programmation informatique. La professeure Hélène Gaonac'h a supervisé la qualité des analyses et la rédaction de la thèse dans son ensemble.

Références

Bruno, B.C., Taylor, G.J., Rowland, S.K., and Baloga, S.M., 1994. Quantifying the effect of rheology on lava-flow margins using fractal geometry, Bull. Volcanol., 56, 193-206.

Chase, C.G., 1992. Fluvial landsculpting and the fractal dimension of topography, Geomorphology, 5, 39-57.

Claps, P., and Oliveto, G., 1996. Reexamining the determination of the fractal dimension of river networks, Water Resources Res., 32, 3123-3135.

Dodds, P.S. and Rothman, D.H., Scaling, universality, and geomorphology, Annu. Rev. Earth Planet. Sci., 28, 571-610, 2000.

Foufoula-Georgiou, E. and Sapozhnikov, B., Anisotropic scaling in braided rivers: an integrated theoretical framework and results from application to an experimental river, Water Ressources Res., 34, 863-867, 1998.

Gaonac'h, H., Lovejoy, S., and Stix, J., 1992. Scale invariance of basaltic lava flows and their fractal dimensions, Geophys. Res. Letters, 19, 785-788.

Gaonac'h, H., Lovejoy, S. and Schertzer, D., Resolution dependence of infrared imagery of active thermal features at Kilauea volcano, Int., J. Remote Sensing, 24, 2323-2344, 2003.

Harvey, D.C., Gaonac'h, H., Lovejoy, S. and Schertzer, D., Multifractal characterization of remotely sensed volcanic features: a case study from Kilauea volcano, Hawaii, Fractals, 10, 265-274, 2002.

Huang, J., and Turcotte, D.L., 1989. Fractal mapping of digitized images: application to the topography of Arizona and comparison with synthetic images, J. Geophys. Res., 94, 7491-7495.

La Barbera, P. and Rosso, R., On the fractal dimension of stream networks, Water Ressourses Res., 25, 735-741, 1989.

Laferrière, A. and Gaonac'h, H., Multifractal properties of visible reflectance fields from basaltic volcanoes, J. Geophys. Res., 104, B3, 5115-5126, 1999.

Lavallée, D., Lovejoy, S., Schertzer, D. and Ladoy, P., Nonlinear variability of Landscape topography: Multifractal analysis and simulation, in Fractals in Geography, edited by De Cola, L. and Lam N., pp. 158-192, Prentice-Hall, Englewood Cliffs, NJ, 1993.

Lovejoy, S. and Schertzer, D., Generalized scale invariance in the atmosphere and fractal models of rain, Water Ressources Res., 21, 1233-1250, 1985.

Lovejoy, S., Schertzer, D. and Pflug, K., Generalized scale invariance and differential rotation in cloud radiances, Physica A, 185, 121-128, 1992.

Lovejoy, S., Schertzer, D., Tessier, Y. and Gaonac'h, H., Multifractals and resolution-independent remote sensing algorithgs: the example of ocean colour, Int. J. of Remote Sensing, 22, 1191-1234, 2001.

Lovejoy, S., Pecknold, S. and Schertzer, D., Stratified multifractal magnetization and surface geomagnetic fields-I. Spectral analysis and modelling, Geophys. J. Int., 145, 112-126, 2001.

Mandelbrot, B.B., 1967. How long is the coast of Britain? Statistical self-similarity and fractional dimension, Science, 155, 636-638.

Mark, D.M., and Aronson, P.B., 1984. Scale-dependent fractal dimensions of topographic surfaces: an empirical investigation, with applications in geomorphology and computer mapping, Math. Geol., 16, 671-683.

Pecknold, S., Lovejoy, S., Schertzer, D., and Hooge, C., 1997. Multifractals and resolution dependence of remotly sensed data: GSI to GIS, in: Scale in Remote Sensing and GIS, eds. D.A. Quattrochi and M.F. Goodchild, CRC Press, Bora Raton, Fla., 361-394.

Pecknold, S., Lovejoy, S. and Schertzer, D., Stratified multifractal magnetization and surface geomagnetic fields-II. Multifractal analysis and simulations, Geophys. J. Int., 145, 127-144, 2001.

Pelletier, J.D., Self-organisatio and scaling relationships of evolving river networks, J. Geophys. Res., 104, 7395-7375, 1999.

Pflug, K., Lovejoy, S. and Schertzer, D., Differential rotation and cloud texture: analysis using generalized scale invariance, J. Atmos. Science, 50, 538-553, 1993.

Schertzer, D. and Lovejoy, S., Generalised scale invariance in turbulent phenomena, Phys. Chem. Hydro. J., 6, 623-635, 1985.

Schertzer, D. and Lovejoy, S, 1995. Standard and advanced multifractal techniques in remote sensing, in Fractals in Geosciences and Remote Sensing, ed. by G.

Wilkinson et al., Office of Official Publications of the European Communities, Luxembourg, 11-40.

Tarboton, D.G., Bras, R.L., Et Rodriguez-Iturbe, I., 1988. The fractal nature of river networks, Water Resources Res., 24, 1317-1322.

Tarboton, D.G., 1996. Fractal river network, Horton's laws and Tokunaga cyclicity, J. of Hydrology, 187, 105-117.

Turcotte, D.L., 1997, Fractals and Chaos in Geology and Geophysics, 2nd ed: Cambridge University Press, Cambridge, 398 p.

Veneziano, D. and Iacobellis, V., Self-similarity and multifractality of topographic surfaces at basin and subbasin scales, J. Geophys. Res., 104, 12797-12812, 1999.

Vignes-Adler, M., Le Page, A., and Adler, P.M., 1991. Fractal analysis of fracturing in two regions, from satellite imagery to ground scale, Tectonophysics, 196, 69-86.

Weissel, J.K., Pratson, L.F., and Malinverno, A., 1994. The lenght-scaling properties of topography, J. Geophys. Res., 99, 13 997-14 012.

Weissel, J.K., Malinverno, A., Harding, D.J. and Karner, G.D., Erosional development of the ethiopian Plateau of northeast Africa from a fractal analysis of topography, in Fractals in Petroleum Geology and Earth Processes, edited by C.C. Barton and P.R. La Pointe, pp. 127-142, Plenum Press, New York, 1995.

CHAPITRE 1

INVARIANCE D'ÉCHELLE DE SURFACES DIFFÉRENTIELLEMENT ÉRODÉES DU RÉSEAU DE DRAINAGE DU PLATEAU ÉTHIOPIEN

SCALING OF DIFFERENTIALLY ERODED SURFACES IN THE DRAINAGE NETWORK OF THE ETHIOPIAN PLATEAU

Published in Remote Sensing of Environment, 82, (2002) 111-122

Alexandre Beaulieu and Hélène Gaonac'h

Université du Québec à Montréal – Centre GEOTOP-UQÀM-McGill,
C.P.8888 succursale Centre-Ville, Montréal, Québec, Canada, H3C 3P8.

Abstract

Differentially eroded regions selected over the Ethiopian plateau, Northeast Africa, were statistically analyzed using satellite images of various electromagnetic spectrum regions and resolutions (Landsat TM and ERS-1). The power spectrum exponent β values for the Landsat TM2 (visible) and ERS-1 images over the same surface are associated to the intrinsic properties of the different sensor type and post-processing of the data. Differences in the β values were observed between eroded area (Blue Nile Canyon) and relatively noneroded area (Plateau) for all data sets. These differences are associated to the mechanical erosion of the plateau. The remotely sensed data fields show scaling from 35 m to 15 km, with no break at 1.5 km, and are highly multifractal. Analyses of the Landsat TM bands over each area demonstrated something particular: β values for bands in the short wave infrared range differed from β values for bands in the visible spectrum range in the plateau area by about 0.48, while in the drainage area, this difference is around 0.13. Landsat TM short wave infrared bands are sensitive to spectral signature of clay minerals, while data in the visible spectrum range mostly depict topography gradients. Two concurrent processes are highlighted, mechanical erosion and chemical erosion/deposition, which interact to produce the observed differences. In the drainage area, where cliffs and steep slopes are present, and mechanical erosion intensively occurs, the alteration minerals are remobilized quickly, whereas in the plateau area, mechanical erosion is low, and alteration mineral deposition is less

disturbed. Such new statistical highlights of topographic versus chemical surfaces will have to be taken into account in landforming models.

1. Introduction

While the dynamical mechanisms responsible for the evolution of the Earth's surface are generally highly non-linear, little is known in a quantitative way about how phenomena such as erosion and deposition occurs over a wide range of spatial and time scales. Synoptic overviews provided by data, such as remotely sensed images, can be very powerful in studying the consequences of these Earth sculpting processes. Despite the intensive development of remote sensing techniques in the past years, the importance of the scale/resolution dependence of the various remotely sensed fields is underestimated in most areas of applications. For example, images obtained at different scales may be very difficult to combine with each other in Geographical Information Systems (GIS) due to the very different variability of data at various spatial resolutions. Standard approaches involving sub-resolution regularity/homogeneity assumptions and/or variability at a single scale is inadequate (Schertzer and Lovejoy, 1995). As described below, an approach that considers the characterization of the data scale by scale using fractal and/or multifractal statistics is more realistic.

Fractal structures and their associated power laws characterize the variation of different measurements (length, perimeter or area) against the spatial resolution (e.g., Gaonac'h et al. (1992)). Even at fixed resolutions, most geophysical processes vary over wide range of intensities with each intensity level defining a different fractal dimension (Lovejoy and Schertzer, 1990; Lavallée et al., 1993; Laferrière and Gaonac'h, 1999). Hence, multifractal analyses using a multitude of statistical moments is more accurate, and in this case, the scaling exponent is a scale invariant function that determines how the statistical moments of a field (e.g., its mean, variance and many other moments) or the probability distribution varies against resolution (Laferrière and Gaonac'h, 1999). Knowledge of the scaling behavior through remotely sensed data gives an opportunity to objectively characterize the various surface phenomena with their underlying scaling properties.

Drainage areas provide examples of morphologies produced by the combination of tectonism and erosional/depositional processes. Many fractal studies were conducted on branching stream networks resulting from erosional/depositional mechanisms (Tarboton et al., 1988; Tarboton, 1996; Claps and Oliveto, 1996) mostly focusing on the estimates of fractal dimensions of river network extracted from Digital Elevation Model (DEM). Xia and Clarke (1997) summarized several examples of fractal analyses of river network showing different fractal dimensions varying between 1 and 2. The methods employed to estimate the fractal dimension, the scale of the map used to digitalize the networks and the fact that sometimes only parts and/or the whole stream network is used are all invoked to affect the estimate of the fractal dimension as shown in the various examples cited in Xia and Clarke (1997). On the other hand, the processes involved in the formation of the land surface, or the lithological aspect of different regions are not explicitly considered in these examples. Although these studies all took into account aspect of scale invariance, they were done with geometric river networks, not with data fields that are more geophysically significants.

Fractal analyses of topographic gradients of drainage surfaces have been used to distinguish the different processes responsible of the terrestrial morphologies either associated with climate and/or structural movements (Chase, 1992; Weissel et al., 1995; Pelletier, 1999). Chase (1992) created a numerical model of landform evolution based on cellular automata. He demonstrated that his model topography is much more sensitive to climatic variables than to tectonic uplifts. Using fractal analyses on topography of areas in southern Arizona, he obtained from 450 m to 45 km a mean fractal dimension around 2.2-2.3, with a characteristic break in the scale at 1.5 km. His interpretation is that topography is indeed multifractal, and caused by the mixing of various processes including erosion, deposition and diffusive weathering. Pelletier (1999) also created a scaling model of the topography including river networks based on diffusion and erosion processes. On the planetary scale, Kucinskas et al. (1992) investigated the scaling of topographic profiles on Venus, noticing small differences in the scaling/spectral exponent between two distinct areas, plains and mountain range. Weissel et al. (1995) conducted fractal analyses of the topography on two areas of the Ethiopian plateau, a relatively noneroded plateau, and a rugged surface sculpted by the Blue Nile river system. Using DEM of 90 m horizontal resolution, as Chase (1992), they observed two scaling regimes from 500 m to 10 km with a break at about 1.5 km. Assuming monofractality, they demonstrated that the degree of roughness, the Hurst exponent *H*, of the topography above 1.5 km is higher for the drainage area (H=0.78, D=2.22, D being the fractal dimension linked to H as D=3- H) than in the plateau area (H=0.51, D=2.49). They suggested that the scale break may be a result of natural processes, such as erosion, diffusion and tectonism, involved in the landscape formation, which may differentiate the shorter length scale (500-1500 m) compare to the longer length scale (above 1.5 km).

Topographic data is one representation of the surface, and is often derived from two stereoscopic images in the visible or from radar data. On the other hand, satellite and airborne data (from visible to microwave) give the opportunity to look at the different aspects of Earth morphologies, structures and chemical compositions (e.g., via solar reflection of the ground, emissions of long Thermal InfraRed (TIR) radiations, back-scattering of an active signal). Hence, the various spectral responses of the constituents of soils and rocks produce very different images for each Landsat TM bands (Table 1). For example, the presence of clay minerals would give distinct responses than other minerals in the Short-Wave InfraRed range (SWIR, Landsat TM5 and TM7 bands) but not in the visible range (VIS, Landsat TM1, TM2 and TM3 bands). Images of solar reflection and microwave backscatter are another example of complementary fields. The shaded effect (layover) particular to radar, the incident angle of the signal and the wavelength used can strongly affect the final image and makes it very different to an image produced by the reflected sun ray. These differences between each data field acquired over a same surface by the various spectral wavelength (VIS, SWIR, TIR and microwave) can be statistically analyzed from one scale to another and be very useful in identifying the underlying processes governing the earth's morphologies.

In this paper, we will focus on the erosion versus deposition surfaces following tectonic, climatic and hydrological processes using remotely sensed data from different spectral regions (VIS, SWIR and microwave). In this context, the underlying processes responsible for the observed morphologies, such as erosion/deposition and tectonism, will be statistically discriminated. The satellite data set chosen for this study is in the Ethiopian plateau of North East Africa (roughly the same region as studied in Weissel et al. (1995)). This region contains a very active drainage system (the Blue Nile and its tributaries), while some parts of the plateau remained relatively noneroded since the time of flood basalt volcanism. Another important advantage for this region is that it has a uniform lithology, flood basalts. It could be simpler to relate the differences of the observed surfaces due to erosion/deposition for a surface with such homogeneous lithology. Statistical differences of various remotely sensed expressions of the same surface, some of them being associated to data acquisition, while others are associated to landforming processes (tectonism, erosion/deposition and composition of soils), will be distinguished. Our results will be compared to those of previous studies involving various landforming processes. Analyzes of remotely sensed data over a wide range of scales compared to river networks and topographic data, correspond to an important step forward in the understanding of landscape forming mechanisms. Such types of studies have already been pursued by other authors such as Harvey et al. (2002) for the discrimination of surface heating processes in volcanic environment.

2. Area description, data set and method

2.1 Geological setting

The area studied is located in the Ethiopian Plateau northeast of Africa between 9° and 12° North and 38° and 41° East (Fig. 1). Continental flood basalts piled up to 2000 meter thick on an area several kilometer wide before rifting occurred (Mohr and Zanettin, 1988). Olivine basalt constitutes the main lithologic unit of this zone undergoing differential erosion. Radiometric ages and field studies indicate an initialization of extension and rift-related volcanism by late Miocene (9 Ma) (Mohr and Zanettin, 1988; Woldegabriel et al., 1990). The original plateau of 2500 m altitude was cut in two parts by the main Ethiopian Rift of 100 km large which widen to the north up to 300 km to form the triangular zone of Afar. As a result of the rifting processes, the margins of the Ethiopian Rift were uplifted. As proposed by Weissel et al. (1995), the uplift of the eastern margin is the result of a flexural isostatic rebound of the lithosphere. In association with a climatic change, this rebound modified the Ethiopian plateau surface regionally in such a way that some parts of the plateau were deeply eroded by the Blue Nile and its tributaries. Other noneroded parts represent remnants of the initial plateau preserved until this day (Weissel et al., 1995).

2.2 Remotely sensed data

The statistical analysis will be conducted on remotely sensed images obtained in different regions of the electromagnetic spectrum. The data consists of a Landsat TM satellite image and one ERS-1 radar image. The location of each data set is depicted in Figure 1. The Landsat TM image was acquired on January 5, 1986, with solar elevation and azimuth angle of 42° and 134° respectively (Eros Data Center, USGS). Description of the wavelength range for each band is made in Table 1. The ERS-1 product, acquired on October 5 1997, is a Satellite Aperture Radar (SAR) precision image generated from raw SAR data of 23 cm wavelength using up-to-date auxiliary parameters, corrected for antenna elevation gain and range spreading loss (Eurimage Radarsat Int'l Spot Image Consortium, ERSC).

The data analyzed from these images (Landsat TM and ERS-1) consist in subsections taken on eroded area (drainage) and relatively noneroded area (plateau). The scenes were first chosen on the Landsat TM image for the bands in VIS (TM1, TM2 and TM3) and SWIR (TM5 and TM7), where two areas were selected, one in the deeply eroded canyon, referred as Blue Nile Canyon (BNC), and the other on the plateau remnants area (PLA) that is relatively noneroded compare to the drainage area (Fig. 2). Each of these Landsat subscenes of 30 m resolution is composed of 1024 by 1024 pixels. The same sections were approximately chosen on the other set (ERS-1). The ERS-1 subscenes of 12.5 m resolution represent 2048 by 2048 pixels.

3. Results

3.1 Power spectrum

Spectral analysis is a convenient way for studying scaling. The usual approach assumes statistical isotropy (more on this below). The spectral energy $E(k)$ corresponds to the angle-integrated, ensemble-averaged, square modulus of the Fourier transforms of the images. If the analyzed data field shows isotropic scale invariant behavior, its energy spectrum can be written as Eq. (1):

$$E(k) \propto k^{-\beta} \tag{1}$$

where β is the scale invariant Fourier exponent and k the spatial wave number in cycle/meter (or cycle/pixel).

We first selected the data sets (Landsat TM2 and ERS-1) associated to topography over the BNC and PLA regions (Fig. 3) for a comparison of their energy spectrum (Fig. 4). This corresponds to ERS-1 and Landsat TM2 subscenes on BNC and PLA. All data sets demonstrate a scaling behavior, from about 120 m ($\log_{10} k$=-2.08) to 15 km ($\log_{10} k$ =-4.18) for the Landsat TM data set and from 35 m ($\log_{10} k$ =-1.54) to 12.8 km ($\log_{10} k$ =-4.11) for the ERS-1 image (Fig. 4). The breakdowns in the scaling for the highest resolutions of both data sets are interpreted as due to the smoothing of the data related to the various image processing (Laferrière and Gaonac'h, 1999). The ERS-1 image, which has a ground resolution of 12.5 m, demonstrates a breakdown in the scaling at about 35 m, while the scaling of the

Landsat TM image, which has a ground resolution of 30 m, breaks at about 120 m. The Landsat TM image is processed to a high level (georectified) leading to a wider smooth range of scales (30-120 m) than for the ERS image (12.5-35 m), the latter consisting of unprocessed raw data.

Scaling energy spectra differ by their Fourier exponent (β values) and their spectral energy amplitude (E(k)). At fixed k, variations in $E(k)$ intensities are attributed to dynamical gray level range and characterize the general roughness of the image (Fig. 3). For example, before enhancement, the Landsat TM2 BNC image has a very low gray level range (99.9 % of values between 20-70 on a 256 gray range) compare to the ERS-1 BNC image (99.9 % of values between 18-224 on a 256 gray range (Fig. 3), hence lower general $E(k)$ intensities (Fig. 4). The differences in the β values for the same area, BNC for example, estimated from the Landsat TM2 (β =0.94) and ERS-1 (β=0.55) data sets (Fig. 4, Table 2) can be explained by variations in the proportion of large structures (low k value) over small ones (high k value) relative to differences in the type of data acquisition (visible and radar) and different post-processing of the resulting images.

When considering the BNC (deeply eroded) and PLA (poorly eroded) morphological regions (Fig. 4), β values are always larger for the BNC area (Table 2). For example, we observed that for Landsat TM2, the β value for BNC is 0.94 compared to 0.36 for PLA. Finally, a closer look at the Landsat TM multispectral data shows something particular. A difference in the β values over the PLA area is observed between the Landsat VIS (β=0.37) and the Landsat SWIR (β=0.85). Analogous differences are not apparent in the BNC area, resulting in a clear distinction between the BNC (SWIR-VIS) and PLA (SWIR-VIS) power spectrum (Fig. 5, Table 2). To emphasize this difference between the SWIR and VIS data over the PLA and BNC areas, the selected sections (BNC and PLA) were divided in 256 by 256 subsections. Results of the analyses of the Fourier exponent (β values) of the VIS were plotted versus those of the SWIR (TM2 versus TM5 and TM3 versus TM7) (Fig. 6). There is a clear separation in two groups in the SWIR-VIS diagram (Fig. 6) between the two BNC and PLA subsections implying that some landforming process is acting differentially in the two areas, being more active in the PLA area.

3.2 Multifractal analysis

As demonstrated by Laferrière and Gaonac'h (1999), the use of conventional fractal methods (e.g., box-counting) on data field gives a series of fractal dimensions. Each distinct threshold would yield a different fractal dimension associated with a geometrical set.

A multiscaling field which has a total range of scale ratio $\lambda = L/l$, the ratio of the large outer scale L to the smaller intermediate scale l, can be described with the probability distribution of the intensities of the field such as Eq. (2):

$$\left.\begin{array}{l}\Pr(\varepsilon_{\lambda} \geq \lambda^{\gamma}) \approx \lambda^{-c(\gamma)} \\ \varepsilon_{\lambda} \geq \lambda^{\gamma}\end{array}\right\} for\ \lambda > 1 \qquad (2)$$

where γ is the order of singularity or the scale independent intensity, $c(\gamma)$ the codimension, and ε_λ the intensity of the field at the scale ratio λ. The ensemble average statistical moments of $q^{(th)}$ order are given by Eq. (3):

$$\left\langle \varepsilon_\lambda^q \right\rangle \propto \lambda^{K(q)} \tag{3}$$

where the exponent $K(q)$ is a scaling function associated with the different q order. Mathematically, the functions $K(q)$ are estimated as slopes of $\log(\langle \varepsilon_\lambda^q \rangle)$ versus $\log(\lambda)$, which implies that there is an infinite number of parameters to be empirically determined. Fortunately, Schertzer and Lovejoy (1987) and Lovejoy and Schertzer (1995) demonstrated that within a dynamic system including non-linear interactions over a continuous range of scale and/or multiplicative interactions of different processes, a considerable simplification is obtained. The multiplicative cascade processes can be generated from a limited number of universal parameters. This universality implies that the laws governing the system are not sensitive to many of the model details. Thus, the universal multifractal parameters characterize the $K(q)$ function such as Eqs. (4) and (5):

$$K(q) = \frac{C_1}{\alpha - 1}(q^\alpha - q) \text{ for } 0 \le \alpha < 1 \text{ and } 1 < \alpha \le 2 \tag{4}$$

$$K(q) = C_1 q \log(q) \text{ for } \alpha = 1 \tag{5}$$

where α is the parameter which describes the degree of multifractality of the field and $0 < C_1 < d$ the codimension of the singularity γ contributing to the average of the field. The multifractal parameter α varies from 0 to 2, α =0 being monofractal, and α

=2 (maximum) corresponding to the lognormal multifractal model. As for C_1, it quantifies the sparseness, in the form of the codimension of the singularity that contributes dominantly to the average. The double-trace moment (DTM) method that has been developed by Lavallée et al. (1993) lets us conveniently estimate the α, C_1 and H parameters. The DTM analysis involves the use of moments of two different statistical orders, q and η at different resolutions λ and Λ (Eq. (6)):

$$\langle (\varepsilon_\Lambda^\eta)_\lambda^q \rangle \approx \lambda^{K(q,\eta)} \tag{6}$$

where ε_Λ, the intensity gradient at each pixel of the field at the finest resolution Λ, is raised to the power η, then average over the intermediate resolution λ, raised to the q-th power and then average over all the data available. The new exponent function $K(q,\eta)$ is related to the scaling function $K(q)$=$K(q,1)$ as Eq. (7):

$$K(q,\eta) = K(q\eta,1) - qK(\eta,1) \tag{7}$$

For the universal multifractality condition, combining (4,5) and (7) shows that $K(q,\eta)$ can be expressed as Eqs. (8) and (9):

$$K(q,\eta) = \eta^\alpha K(q,1) = \frac{C_1}{\alpha-1}\eta^\alpha (q^\alpha - q) \text{ for } \alpha \neq 1 \tag{8}$$

$$K(q,\eta) = \eta^\alpha K(q,1) = C_1 \eta q \log(q) \text{ for } \alpha = 1 \tag{9}$$

α can be estimated as the slope of the scale invariant function $K(q,\eta)$ versus η on a log-log plot and C_1 from the intercept. Relevant applications of this method include Laferrière and Gaonac'h (1999), Pecknold et al. (1997) and Harvey et al. (2002). For accurate estimate of the multifractal parameters, the DTM has to be applied to conservative multifractal field in which the mean of the cascade process is the same at each scale. The analyzed field being generally not conservative, an additional scaling $\lambda^{(-H)}$ is consider where H is the Hurst exponent. Since $\beta = 1\text{-}K(2)\text{+}2H$, the non-conservative parameter H can be estimated by Eq. (10):

$$H = \frac{\beta - 1}{2} - C_1 \frac{(2^{\alpha} - 2)}{2(\alpha - 1)} \tag{10}$$

Multifractal analyses of the data sets are describe in Table 3, and, as an example, the multiscaling of the Landsat TM5 BNC area is exhibited from 120 m (λ=256) to 30 km (λ=1) as the slope $K(q,\eta)$ increases with η in Figure 7. The multifractal parameters \alpha and C_1 are then deduced from Figure 8. When considering all the data, the \alpha parameter yields result around 1.9 and the C_1 values around 0.03 for all data sets; the H parameter however, has values that varies directly with the β values (Table 2) e.g. Landsat VIS BNC H = -0.02; Landsat VIS PLA H = -0.29.

4. Discussion

Utilization of diverse remotely sensed data in the observation of the Earth surface is a very useful practice, however, one has to be careful about the fact that each image may represent particular aspects and properties of the surface. For example, images from one region (BNC) taken in the visible electromagnetic spectrum range are quite different from images of the same region in the microwave range, both exhibiting scaling behavior, but with different statistical exponents and intensities (i.e., Landsat TM2 and ERS-1 data, Figure 4). The differences in β values between the images of the same region (Fig. 4) are associated with the sensor types. All the post-processing steps of satellite data will affect the final representation of the image. For example, enhancement (stretching) of an image will mostly increase the energy amplitude of the spectrum at all scales. An applied stretch on the Landsat TM2 image confirmed a shift of the whole spectrum to higher amplitudes but no change in the β value. The very low β value of the ERS-1 image on the BNC and PLA areas may be attributed to the radar data properties of this sensor (speckeling, dominance of azimuthal features, layover). More studies have to be done to better understand such statistical differences.

The plateau area (PLA) β values are systematically lower (Fig. 4) in each data sets (VIS and radar) then in the eroded areas (BNC), e.g., β_{BNC}=0.94 compare to β_{PLA}=0.36 for Landsat TM2. Satellite images like Landsat TM2 and ERS-1, reflect the distribution of the topography and its related gradient. Regions with flat topography, such as the PLA area, will produce fewer large structures compared to small structures producing a rougher field. Images in the visible spectrum range such as Landsat TM2 also include the spectral mineral signature of the observed surface (e.g., black basalt compared to gray granite); in the studied regions, this aspect is of lesser importance because of the lithologic uniformity (flood basalts). As suggested by Laferrière and Gaonac'h (1999), a simple reflection model predicts a difference of 1 between the albedo and the topography β values, the later being higher (Table 2).

Such differences between the H (Hurst exponent) of the PLA and BNC areas over the Ethiopian plateau has been confirmed through variogram analyses of topography by Weissel et al. (1995) on the same regions (drainage H=0.78, plateau H=0.51). On the other hand, we do not observe any break in the scaling around 1.5 km as Weissel et al. (1995) and Chase (1992) did on topography.

Variations of the β values in different spectral bands of the Landsat TM image (e.g., VIS and SWIR) showed little variations in drainage areas (β_{BNC}=0.94 compare to β_{BNC} =1.10 for Landsat TM2 versus TM7) whereas in the plateau, the relative difference is more pronounce (β_{PLA} =0.36 compare to β_{PLA} =0.87 for Landsat TM2 versus TM7) (Fig. 5 and 6). These differences between the VIS and SWIR channels for the PLA area can be explained by differing surface spectral signature, due to varying spatial distributions of soil composition. For example, Landsat TM multispectral imagery has been used since many years now to characterize different type of soil composition (Drury and Hunt, 1989; Vitorello and Galvão, 1994; Madeira et al., 1997). The tropical climate of the Ethiopian plateau associated with the rifting makes it a place where there was, and still is, a lot of precipitation, so the lithologic units are geochemically altered by weathering (laterized) due to tectonic uplift and climatic effects, implying mechanical as well as chemical erosion and deposition (Augustithis and Vgenopoulos, 1981). This led to the formation of laterized soil up to several meters depth. Basalt lateritization will produce clay minerals, such as kaolinite and chlorite, and limonitic minerals like geothite and hematite, which will easily retain surface water and favor vegetation growth. Landsat TM5 and TM7 (SWIR) and their ratio are sensible to clay minerals because of their spectral signature (Drury and Hunt, 1989; Vitorello and Galvão, 1994; Madeira et al., 1997). Using band ratioing on Landsat TM images on the different zones (BNC and PLA), it is possible to confirm variation in the clay content or in the spatial distribution of the clay minerals. The Landsat TM ratio TM5/TM7, which emphasize the clay minerals, show that in the plateau area (PLA), the distribution of clays, exhibited in lighter gray tones in the images, is more widespread than in the drainage area (Fig. 9), producing a marked increase of the β value from VIS to SWIR bands in the PLA area compare to the BNC area.

This observation corroborates with the fact that lateritization dynamics are different in flat and inclined areas. Remobilization of alteration minerals on steep slopes and cliffs happens with a higher rate, rejuvenating the old surface compare to flat area where alteration minerals accumulates. In fact, a previous study on climate forcing mechanisms in the Cenozoic explained a similar relation between weathering and abundance of alteration minerals (Raymo and Ruddiman, 1992). Their model implies that in areas dominated by rapid mechanical erosion, the surface area is always renewed with fresh minerals. In comparison, in the flat areas, chemical erosion is pervasive and contributes less to the river system. This is reflected in the different statistical characteristics of the Landsat VIS and SWIR images, which are different for the PLA and the BNC area (Fig. 6). The competition between different landforming processes based on scaling properties of the topography has previously been suggested by Kucinskas et al. (1992), Chase (1992) and Pelletier (1999). Our study involving the SWIR data introduced a further step for the investigation of landforming evaluation and deposition/remobilization of alteration minerals.

As for the multifractal analysis, irrespective of the data sets used, the α and C_1 parameters are roughly the same, yielding high values in the α parameter (1.9), which means that these fields are highly multifractal (close to a lognormal). The low C_1 values imply a relatively uniform spatial distribution of the singularity γ contributing to the mean gradient of the field. Since a and C_1 are roughly fixed, variations in the H parameter between the different sets is responsible for the variations in the β values. Laferrière and Gaonac'h (1999) obtained similar result for their analysis of satellite and aerial photos on Etna and Mauna Loa volcanoes. The α, C_1, β and H values they obtained for the SPOT panchromatic image on two volcanoes (Etna and Mauna Loa) is close to our values for the Ethiopian-BNC area with the Landsat VIS data (Table 2 and 3). This may be due to the qualitative visual resemblance of lava flow field and river network. Modeled diffusion-limited aggregation yields patterns very similar to natural development of river branching systems and lava flow lobes (Halsey, 2000).

5. Conclusions

Investigation of terrestrial landforming processes with satellite images is very useful, but great care has to be taken when comparing data from different sensors and resolutions. The difference in β values between data acquired in different electromagnetic spectrum range (Landsat TM VIS spectrum and ERS-1 microwave backscattered images) over the same areas is related to acquisition and processing methods. As expected, the ERS-1 image provides distinct scaling properties than visible images, reflecting the particular distribution of the structures related to microwave active remote sensing. Our remotely sensed data confirmed scaling differences between eroded and relatively non-eroded areas as previously observed by Weissel et al. (1995) but no characteristic scale at 1.5 km. The investigated data sets, over the studied region, are distinguished only by H (or β), the multifractal analyses showing similar results for all data sets (highly multifractal).

On the other hand, spectral and multifractal analysis of multiple data sets reveal other properties of the landscape related to erosion/deposition processes that interact together, the mechanical removal of material and the chemical alteration of minerals which permit remobilization of some components of the rocks. The new resulting scaling patterns of clays on the plateau area provided characteristic power spectra in the SWIR compared to the VIS range. Although clay minerals are also present in the drainage area, their distribution follows the topographic gradient, hence giving similar power spectra between the two distinct spectral regions. These results give way to interesting possibilities for the use of remotely sensed images in regions where soil loss and remobilization intensively occur. Our new multispectral and multiscaling results may have to be incorporated in models to more closely describe natural landscapes. Further studies will involve scaling filtering to resolve data discrepancies for images of a given region taken at different time of the day or the year, or in different electromagnetic ranges, as well as other case studies of differential erosion/deposition in various landforming environments.

Acknowledgements

We wish to thank Shaun Lovejoy, Jean-Claude Mareschal, Evelise Bourlon and Dany Harvey for their help and support as well as an anonymous reviewer for improvement of the manuscript. This work was supported by Fonds pour la Formation de Chercheur et l'Aide à la Recherche (FCAR grant).

References:

Augustithis, S.S. & Vgenopoulos, A. (1981). Geochemical and mineralogical studies of the alteration (lateritic) cover of alkali trachy-andesite from the Plateau. In M.K.R. Chowdhury, B.P. Radhakrishna, R. Vaidyanadhan, P.K. Banerjee, & K. Ranganathan (Eds.), *Laterisation Processes*, (pp. 139-143). Rotterdam, Netherlands, Balkema.

Chase, C.G., (1992). Fluvial landsculpting and the fractal dimension of topography. *Geomorphology*, *5*, 39-57.

Claps, p. & Oliveto, G. (1996). Reexamining the determination of the fractal dimension of river networks. *Water Resources Research*, *80*, 267-280.

Drury, S.A. and Hunt, G.A. (1989). Geological uses of remotely-sensed reflected and emitted data of laterized Archaen terrain in Western Australia. *International Journal of Remote Sensing*, *10*(3), 475-497.

Gaonac'h, H., Lovejoy, S. and Stix, J. (1992). Scale invariance of basaltic lava flows and their fratal dimensions. *Geophysical Research Letters*, 19(9), 785-788.

Halsey, T.C. (2000). Diffusion-limited aggregation: a model for pattern formation. *Physics Today*, *November 2000*, 36-41.

Harvey, D.C., Gaonac'h, H., Lovejoy, S. and Schertzer, D. (2002). Multifractal characterization of remotely sensed volcanic features: a case study from Kilauea volcano, Hawaii, *Fractals*, *10*, 265-274.

Kucinskas, A.B., Turcotte, D.L. and Huang, J. (1992). Fractal analysis of Venus topography in Tinatin Planitia and Ovda Regio. *Journal of Geophysical Research*, *97*(E8), 13635-13614.

Laferrière, A. and Gaonac'h, H. (1999). Multifractal properties of visible reflectance fields from basaltic volcanoes. *Journal of Geophysical Research*, *104*(B3), 5115-5126.

Lavallée, D., Lovejoy, S., Schertzer, D. and Ladoy, P. (1993). Nonlinear variability of Landscape topography: Multifractal analysis and simulation. In L. De Cola & N. La (Eds.), *Fractals in Geography* (pp. 158-192). Englewood Cliffs, NJ: Prentice-Hall.

Lovejoy, S. and Schertzer, D. (1990). Our multifractal Atmosphere: A unique laboratory for non-linear dynamics. *Physics in Canada*, *46*(4), 62-71.

Lovejoy, S. and Schertzer, D. (1995). How bright is the coast of Brittany?. In G. Wilkinson, I. Kanellopoulos, & J. Mégier (Eds.), *Fractals in Geoscience and Remote Sensing, Image Understanding Research Vol. 1* (pp. 102-151). Luxembourg, Office of Official Publications of the European Communities.

Madeira, J., Bedidi, A., Cervelle, B., Pouget, M. and Flay, N. (1997). Visible spectrometric indices of hematite (Hm) and geothite (Gt) content in lateritic soils: the application of a Thematic Mapper (TM) image for soil-mapping in Brasilia, Brazil. *International Journal of Remote Sensing*, *18*(13), 2835-2852.

Mohr, P. and Zanettin, B. (1988). The ethiopian flood basalt province. In J.D. McDougall (Ed.), *Continental Flood Basalt* (pp. 63-110). Netherlands: Kluwer Academic Publishers.

Pecknold, S., Lovejoy, S., Schertzer, D. and Hooge, C. (1997). Multifractals and resolution dependence of the remotely sensed data: GSI to GIS, In D.A. Quattrochi & M.F. Goodchild (Eds.), *Scale in Remote Sensing and GIS* (pp. 361-394). Boca Raton, FL: CRC Lewis.

Pelletier, J.D. (1999). Self-organisation and scaling relationships of elvolving river networks. *Journal of Geophysical Research, 104*(B4), 7359-7375.

Raymo, M.E. and Ruddiman, W.F. (1992). Tectonic forcing of late Cenozoic climate. *Nature, 359*, 117-122.

Schertzer, D., and Lovejoy, S. (1987). Physical modeling and analysis of rain and clouds by anisotropic scaling of multiplicative processes. *Journal of Geophysical Research*, *92*, 9693-9714.

Schertzer, D., and Lovejoy, S. (1995). Standard and advanced multifractal techniques in remote sensing. In G. Wilkinson et al. (Eds.), *Fractals in Geosciences and Remote Sensing* (pp. 11-40). Luxembourg: Office of Official Publication of the European Communities.

Tarboton, D.G., Rafael, L.B., Rodriguez-Iturbe, I. (1988). The fractal nature of river networks. *Water Resources Research*, *24*, 1317-1322.

Tarboton, D.G. (1996). Fractal river network, Horton's law and Tokunaga cyclicity. *Journal of Hydrology*, *187*, 105-117.

Vitorello, I. and Galvão, L.S. (1996). Spectral properties of geologic materials in the 400- to 2500 nm range: review for application and lithologic mapping. *Photo-interprétation*, *2*, 77-99.

Weissel, J.K., Malinverno, A., Harding, D.J. and Karner, G.D. (1995). Erosional development of the ethiopian Plateau of northeast Africa from a fractal analysis of topography. In C.C. Barton et P.R. La Pointe (Eds.), *Fractals in Petroleum Geology and Earth* Processes (pp. 127-142). New York: Plenum Press.

Woldegabriel, G., Aronson, J.L. and Walter, R.C. (1994). Geology, geochronology, and rift basin development in the central sector of the main Ethiopia Rift. *Geological Society of America Bulletin*, *102*, 439-458.

Xia, Z. and Clarke, K.C. (1997). Approaches to scaling of geo-spatial data. In D.A. Quattrochi & M.F. Goodchild (Eds.), *Scale in Remote Sensing and GIS* (pp. 309-360). Boca Raton, FL: CRC Lewis.

Tables

Table 1

Spectral characteristics of the Landsat TM sensor

Band	Spectral range (um)	
TM1	0.45-0.52	VIS
TM2	0.52-0.60	
TM3	0.63-0.69	
TM4	0.76-0.90	NIR
TM5	1.55-1.75	SWIR
TM7	2.08-2.35	
TM6	10.4-12.5	

Table 2

Power spectrum analysis results

Platform	BNC	PLA
Landsat TM2	0.94	0.36
Landsat TM3	0.93	0.38
Landsat TM5	1.02	0.82
Landsat TM7	1.10	0.87
ERS-1	0.55	0.20
Spot Radiance Field Etna[a]	1.16	
Spot Radiance Field Mauna loa[a]	1.29	
Aerial Radiance Field Etna[a]	0.90	
Deadman's Butte Topography[b]	1.93 ± 0.03	
United States Topography[c]	1.91 ± 0.03	

Error on β estimates for all data sets is about 0.01.

[a] From Laferrière and Gaonac'h (1999).

[b] From Lavallée et al. (1993).

[c] From Pecknold et al. (1991).

Table 3

Multifractal analysis results

Platform	α	C_1	H
Landsat VIS (BNC/PLA)	1.89/1.87	0.03/0.03	-0.02/-0.29
Landsat SWIR (BNC/PLA)	1.91/1.89	0.03/0.03	-0.06/-0.03
ERS-1 (BNC/PLA)	1.96/1.85	0.04/0.02	-0.19/-0.40
Spot Radiance Field Etna[a]	1.84	0.05	0.13
Spot Radiance Field Mauna loa[a]	1.90	0.03	0.17
Aerial Radiance Field Etna[a]	1.72	0.03	-0.02

Error on α, C_1 and H estimates for all data sets is about 0.01-0.02.

[a] From Laferrière and Gaonac'h (1999).

Figure captions:

Figure 1: Geological map of Ethiopia (modified from Mhor and Zanettin, 1988) showing the location of the Landsat TM image (large square) and the ERS-1 image (small square).

Figure 2: Subsections of the Landsat TM image, BNC and PLA areas. The image is a color-composite of bands 3, 4 and 5.

Figure 3: BNC and plateau PLA represented by different remotely sensed images. (a) Landsat TM2 BNC, (b) ERS-1 BNC, (c) Landsat TM2 PLA, and (d) ERS-1 PLA. Landsat images are enhanced for a better visualisation.

Figure 4: Power spectrum analyses for the Landsat and ERS-1 data sets over the BNC and PLA areas. ○ =ERS-1 BNC with a slope (β)=0.55, ●= ERS-1 PLA with a slope(β)=0.20, ∇=Landsat TM2 BNC with a slope(β)=0.94 and +=Landsat TM2 PLA with a slope(β)=0.36.

Figure 5: Plot of the substraction of SWIR and VIS spectrum for BNC and PLA areas. ◊=Landsat TM7-TM2 PLA and ■=Landsat TM7-TM2 BNC. For PLA and BNC, slopes are 0.48 and 0.17, respectively, and the correlation coefficients 0.91 and 0.97, respectively.

Figure 6: Plot of SWIR versus VIS β values for 256 by 256 pixels subsections of BNC (Δ) and PLA (▼) areas.

Figure 7: $\langle(\varepsilon_{\Lambda}^{\eta})_{\lambda}^{q}\rangle$ versus $\log_{10}(\lambda)$ for various η values and for q=2 for Landsat TM5 BNC area. For each η value, we observe a linear trend in the $\log_{10}$-$\log_{10}$

diagram. The scaling in each case is exhibited from 120 m (λ=256) to 30 km (λ=1). Δ η=2.00, ◊ η=1.58, × η=1.26, ○ η=1.00.

Figure 8: Plot of $\log_{10}|K(2,\eta)|$ versus $\log_{10}\eta$ for Landsat TM5 BNC area, exhibiting universal multifractality over approximately η=0.04 and η=1. The slope α= 1.91.

Figure 9: Landsat TM5/TM7-ratioed images (similar enhancement) of BNC and PLA areas showing the relative content and distribution of clay minerals.

Figure 1

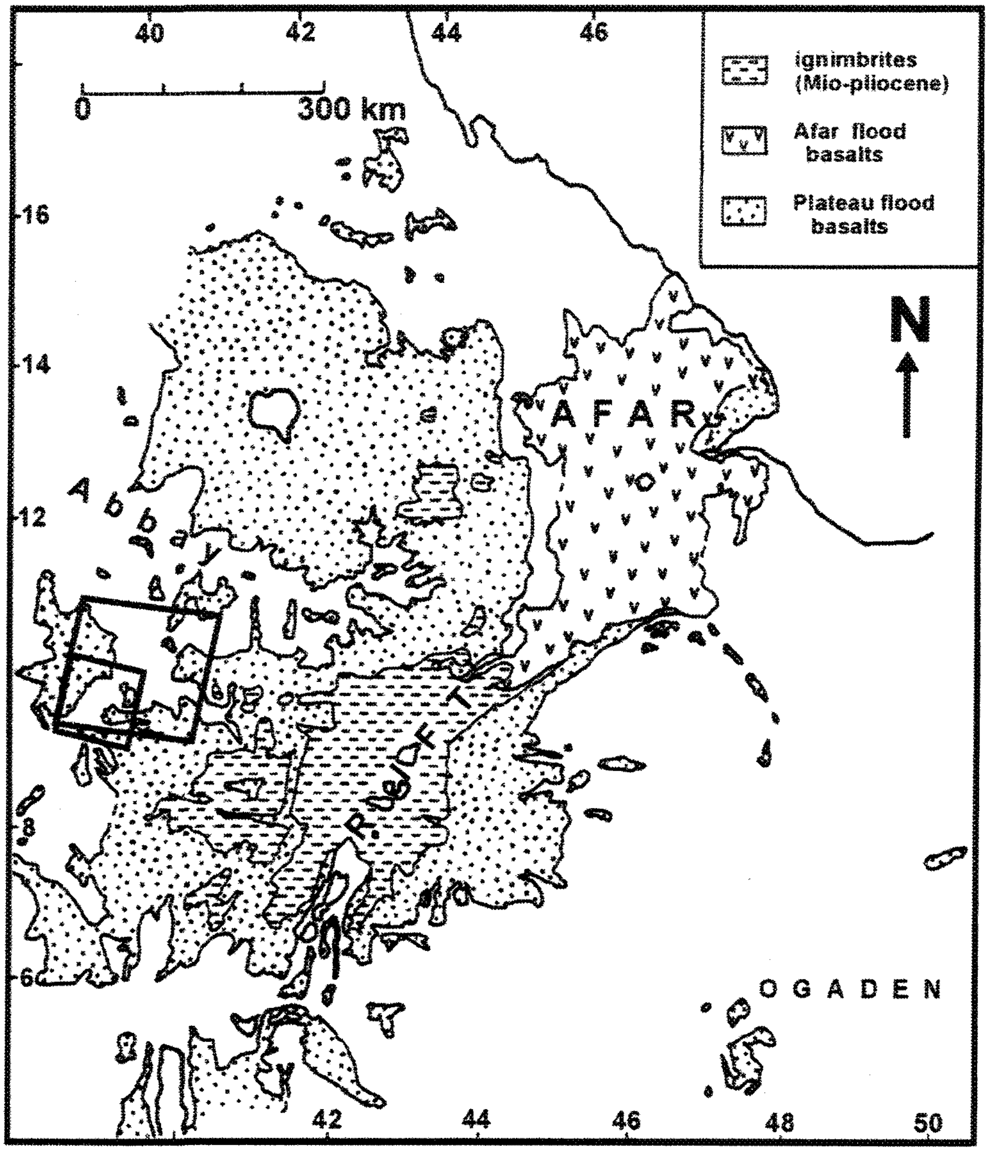
40
42
44
46
0
300 km
16
14
12
8
6
ignimbrites (Mio-pliocene)
Afar flood basalts
Plateau flood basalts
N
A F A R
Abbay
R I F T
O G A D E N
42
44
46
48
50

Figure 2

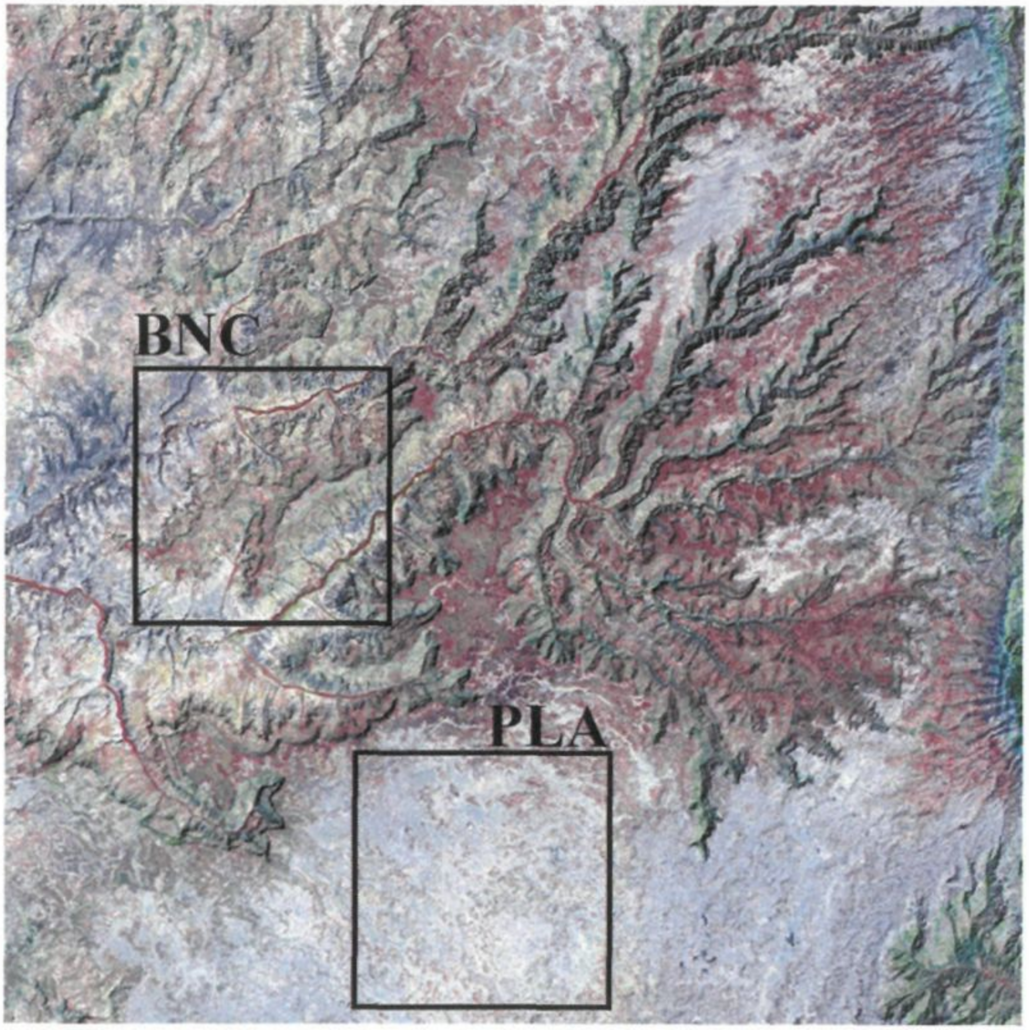

Figure 3

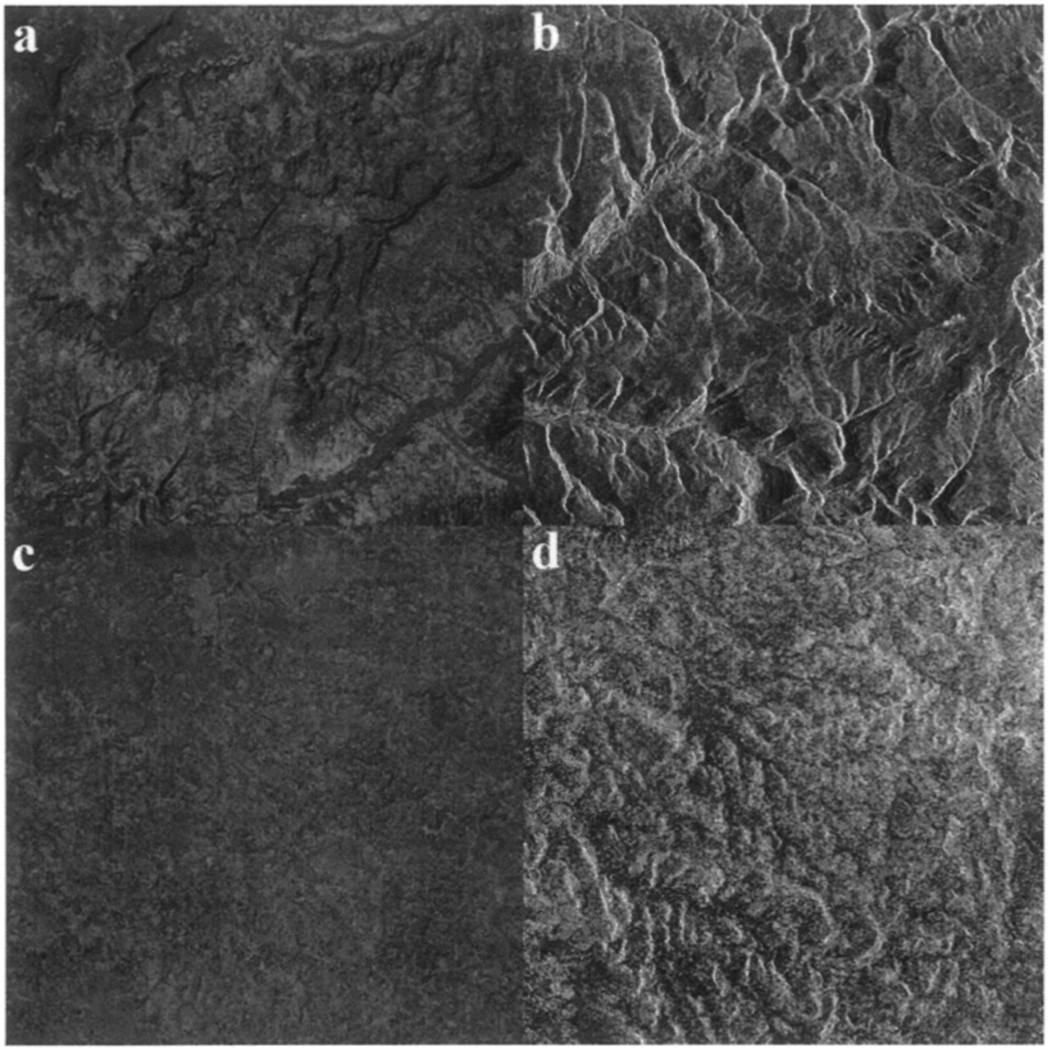

Figure 4

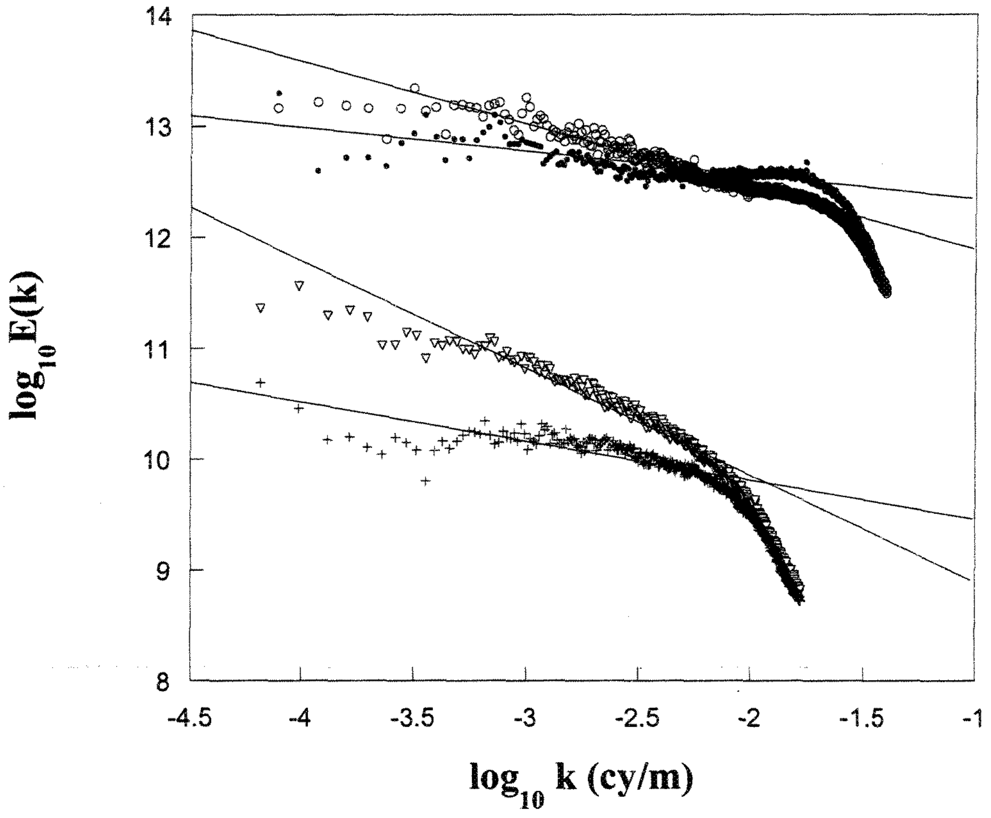

Figure 5

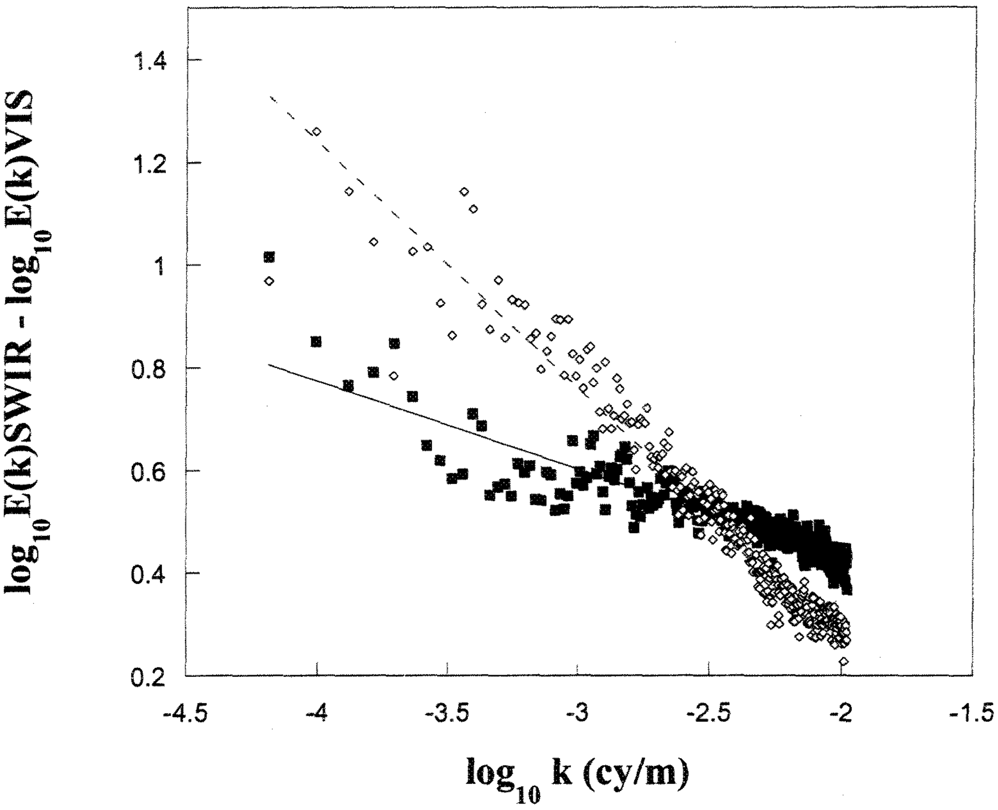

$\log_{10} E(k)SWIR - \log_{10} E(k)VIS$
1.4
1.2
1
0.8
0.6
0.4
0.2
-4.5
-4
-3.5
-3
-2.5
-2
-1.5
$\log_{10}$ k (cy/m)

Figure 6

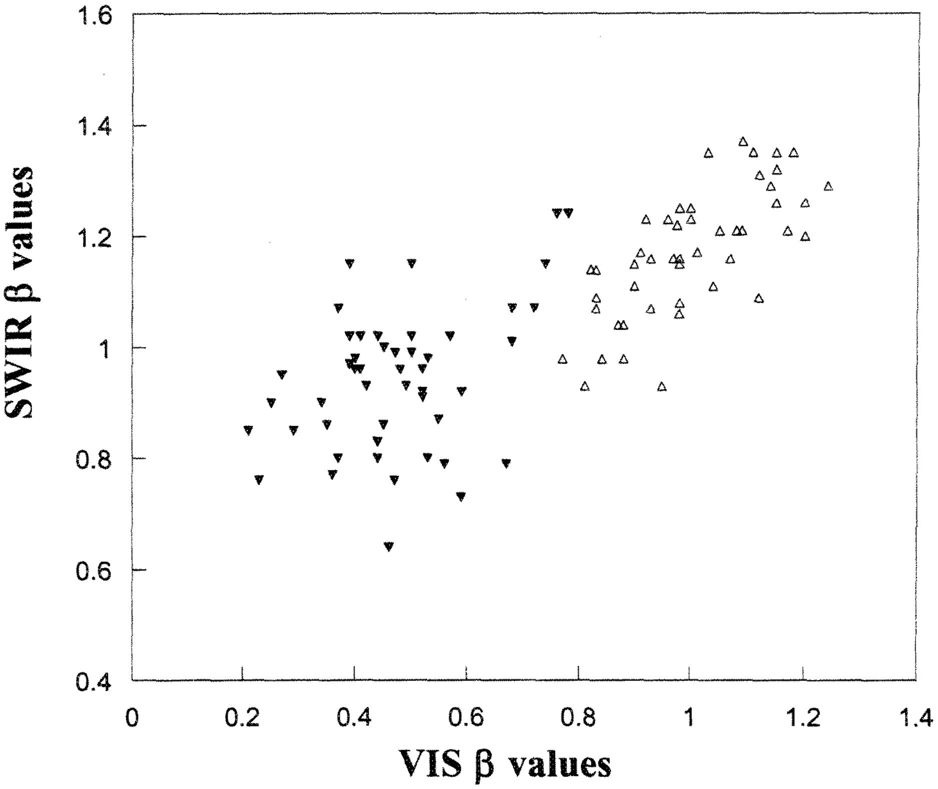

Figure 7

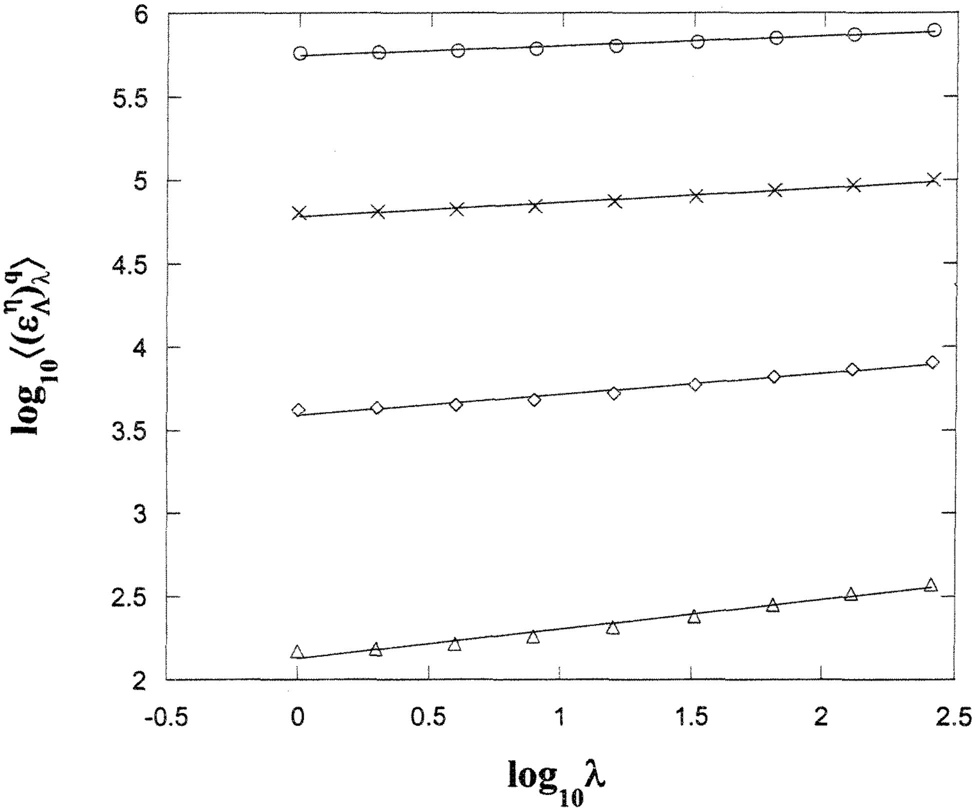
6
5.5
5
4.5
4
3.5
3
2.5
2
-0.5
0
0.5
1
1.5
2
2.5
$\log_{10}\langle(\varepsilon_\lambda^\eta)^q\rangle$
$\log_{10}\lambda$

Figure 8

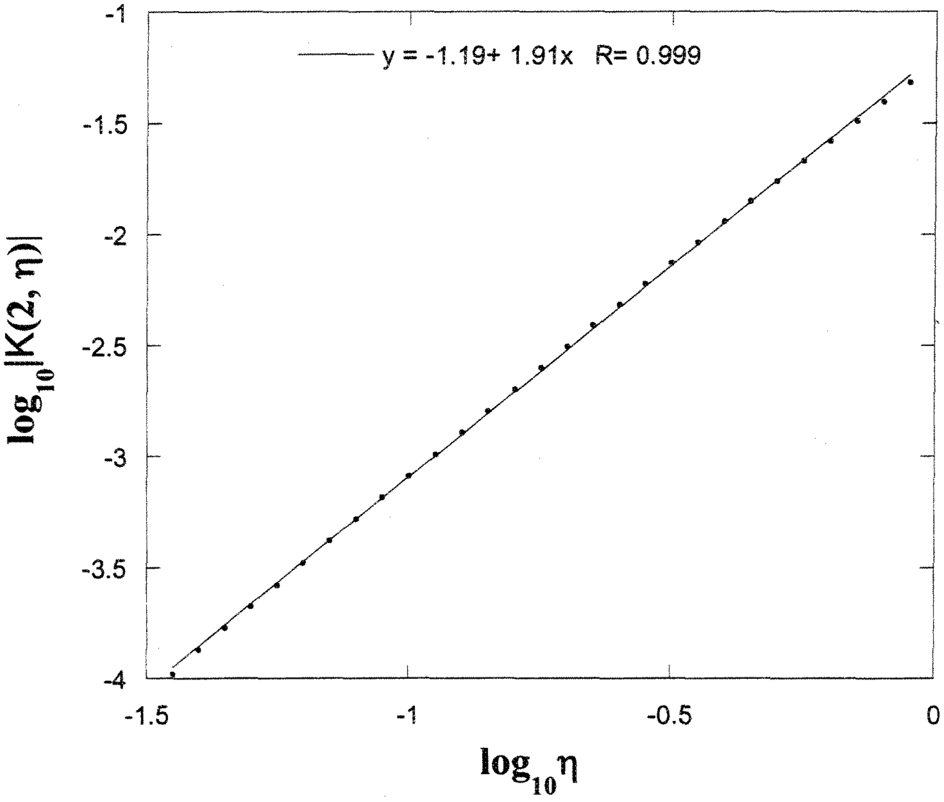

Figure 9

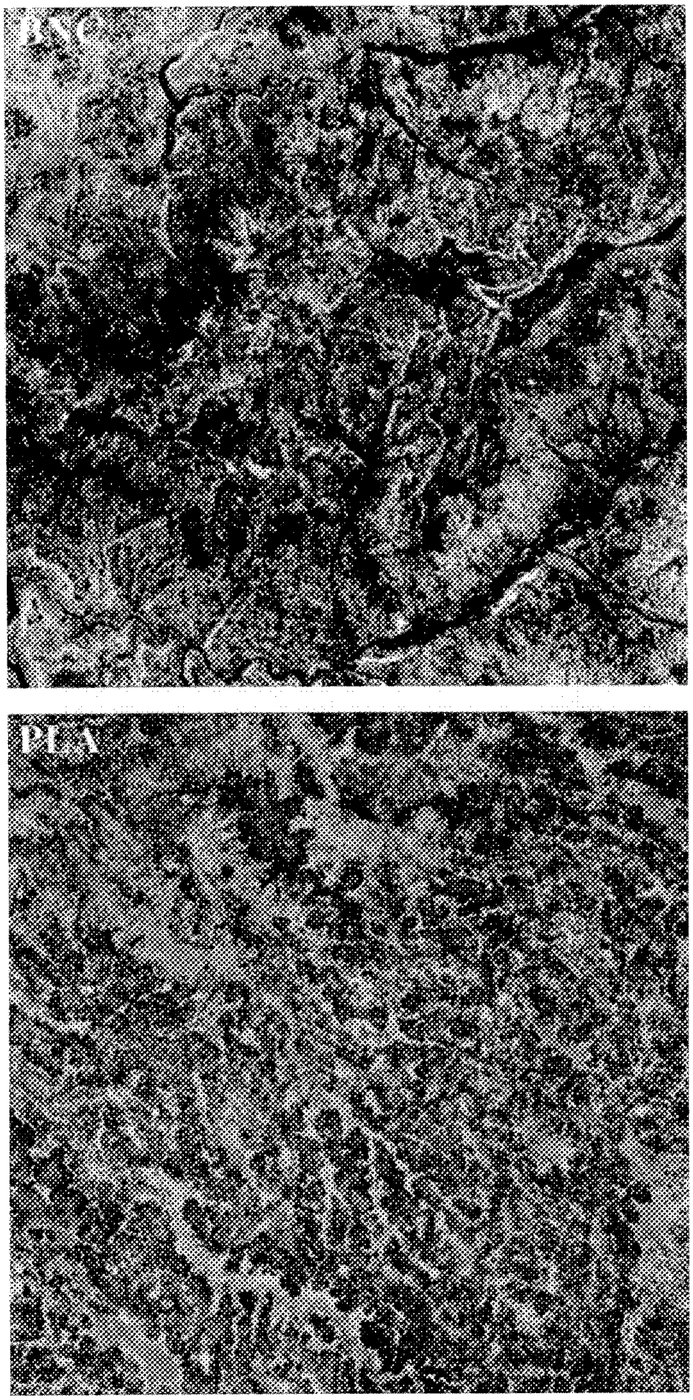

CHAPITRE 2

RECHERCHE DE L'ANISOTROPIE INVARIANTE D'ÉCHELLE D'IMAGES TÉLÉDÉTECTÉES DE RÉSEAUX FLUVIAUX

SCALE-INVARIANT ANISOTROPY INVESTIGATION OF REMOTELY SENSED IMAGES OF RIVER NETWORKS

In preparation for submission to Journal of Geophysical Research

Alexandre Beaulieu[1], Hélène Gaonac'h[1] and Shaun Lovejoy[2]

1- Université du Québec à Montréal – Centre GEOTOP-UQÀM-McGill,
C.P.8888 succursale Centre-Ville, Montréal, Québec, Canada, H3C 3P8.
2-Université McGill, Department of Physics, 3600 University, Montreal,
Québec, Canada, H3A 2T8

Abstract

Investigation of the statistical properties of two drainage networks selected in different environments is conducted with the use of remotely sensed images of the ASTER sensor. Compare to the conventional characterization of the drainage network patterns retrieved from elevation data, remote sensing images provide more information on the different river networks. A first interesting result is demonstrated by the β values obtained for the various drainage studied. We can differentiate the very dendritic China Loess Plateau images, which show very low β values compare to the other images. However, it is not possible to make distinction between the other images from China and Utah with the β values only. For this, we characterized the anisotropic properties of the river networks represented in these images. First, we showed that anisotropy is scale invariant and that it can be characterized in the linear Generalized Scale Invariance (GSI) Framework. We demonstrated that the various networks have different anisotropic behaviors (differential anisotropy (ζ_1) and anisotropy at a characteristic scale (ζ at 960 meters)). We suggest that the higher differential anisotropy values reflect the mature aspect of river networks whereas the higher Utah ζ(960 m) values, which characterize a stronger anisotropy at this scale may be related to the presence of tectonic mechanisms in this region. This new way of investigating the statistics, particularly the anisotropy, over various data field, can provide insightful information on their properties and help characterize and discern their intrinsic properties.

Introduction

The earth's surface is produced by the tectonic, volcanic, erosional and depositional mechanisms carving the topography of the land. The similarities at different scales observed in the natural landforms on the Earth's surface gave rise to a lot of statistical studies. Quantitative measurements of natural morphologies such as lengths, perimeters and areas have been related to their size/scales by power laws (e.g., Gaonach'h et al., 1992; Bruno et al., 1994). Such behavior has indeed been found from the earth's whole topography to much smaller structures (e.g., Vening Meinesz, 1951; Bell, 1975; Mark and Aronson, 1984; Turcotte, 1987; Brown, 1987; Huang and Turcotte, 1989; Lovejoy and Schertzer, 1990; Power and Tullis, 1991; Klinkenberg and Goodchild, 1992; Chase, 1992; Lavallée et al., 1993; Van Put et al, 1994; Malinverno, 1995; Gagnon et al., 2003). This study will mainly focus on landforms created by fluvial erosion, the shaping of the land by rivers. Scale invariance investigations in fluvial geomorphology and river networks also gave rise to a lot of scaling studies (e.g., Rodriguez-Iturbe and Rinaldo, 1998). It has been characterize in many different ways: geometric aspect of streams by Horton (1945), stream ordering by Strahler (1957) and fractal dimensions of stream number and stream lengths by La Barbera and Rosso (1989). They argued that the effect of geology and hydrology should reduce the values of the fractal dimension estimates, removing the possibility of the river networks to fill the space, hence having values under 2.0. Studies on river networks and their scaling behaviors gave rise to new laws relating various aspects of the geometrical nature of these networks. Pelletier (1999) and Dodds and Rothman (2000) provide good reviews on the subject.

River network data are routinely extracted from topographic surfaces for the investigation of their topological and scale invariant statistics. It is important to link the scale invariant exponents with the underlying physical and geological processes. Monofractal scaling investigations of river networks provided significant information, but the investigation of data fields, such as topographic surfaces and remotely sensed images representing drainage areas, is also necessary. Scaling fields are better characterized by multifractals instead of monofractals; nonlinear exponent functions are used instead of a unique scaling exponent. For each threshold of a data field (or for each statistical moment), a fractal dimension that determined the entire function is needed to completely characterized the scaling. The multifractal behavior of topographic surfaces brought a more generalized investigation of the scale invariance through a whole series of statistical moment orders (e.g., Lavallée et al., 1993, Weissel and Pratson, 1994, Pecknold et al., 1997). Gagnon et al. (2003) found over range 20 000 km to 40 m that isotropic moments of order less than 2 are determined by two universal multifractal parameters to within ± 45% in the statistical moments.

Remotely sensed data provide information on the topography/albedo as well as various other projections of natural "surfaces" through the different spectral regions (e.g. visible, short-wave infrared, infrared, microwave). This gives the possibility to go beyond the surface roughness of the land and to look at other fields such as the chemical composition of soil, its humidity, its temperature etc. Examples of scale invariance studies using remotely sensed fields have been conducted in hydrology, volcanology, biology (e.g., Laferrière and Gaonac'h, 1999; Maître and Pinciroli, 1999; Lovejoy et al., 2001; Harvey et al., 2002; Gaonac'h et al., 2003). Beaulieu and Gaonac'h (2002) investigated through Landsat TM 5 and ERS-1 images the drainage area of the Ethiopian Plateau. They found similar differences in the statistics of albedo fields between eroded and less eroded areas as previously demonstrated by Weissel et al. (1995) with topographic data. On the other hand, while investigating in infrared spectral regions, Beaulieu and Gaonac'h (2002) proposed that mechanical erosion and chemical erosion processes are differently acting on the Ethiopian Plateau.

The simplest hypothesis is that the statistics are independent of directions (isotropy), if the system is also scale invariant, it will be "self-similar". The scale invariant properties of surfaces are routinely characterized by using isotropic statistics, which disregard the effect of anisotropy or preferentially-oriented forms, a property that is commonly present in nature. However, natural systems are rarely if ever isotropic and the anisotropy is generally a function of size. Rather than impose an a priori isotropic notion of scale on our system, it is therefore natural to allow the system itself to define the appropriate anisotropic notion. This is the idea behind Generalized Scale Invariance (GSI), a general formalism for scale invariance that takes into account anisotropic variation with scale (Schertzer and Lovejoy, 1985; Lovejoy and Schertzer, 1985). Only few studies in earth sciences raised the possibility that anisotropy could play an important role in scale invariance. Using topographic profiles oriented EW and NS, Weissel et al. (1994) showed that each direction was exhibiting a different scale invariant exponent depending on the orientation. Foufoula-Georgiou and Sapozhnikov (1998) revealed differential scaling behavior in an experimental braided river system. Self-affine scaling is suggested in the literature as a way to characterize anisotropy in a scaling perspective. However, in this case, anisotropy is confined to fixed coordinate axes, and this is an insufficient generalization for most applications (Pecknold et al., 1997). Lovejoy et al. (1992) and Pflug et al. (1993), using GSI, demonstrated, with remotely sensed images of clouds, that scale-changing operation in anisotropic systems, such as differential stratification, differential rotation and even more complex scale-changing operation can be quantified. Geomagnetic fields, where differential anisotropy varies versus the scale ratio, were quantified in the GSI framework (Lovejoy et al., 2001; Pecknold et al., 2001).

Studying natural dynamical processes such as erosion needs to be done over a wide range of scales in order to explain the large variety of landforms; specifying the anisotropy of observed morphologies is essential to broadly outline the natural scaling anisotropic aspect of the erosion. Estimates and comparisons of statistical scaling and anisotropic scale invariant properties of the fields would be a first step in relating the underlying dynamical processes to the observed morphologies. For example, would river networks observed on remotely sensed images evolving on different geological settings and possibly being affected by different tectonic mechanisms, show distinct anisotropic scaling? Isotropic scaling analysis of the topography is accurately obeyed over large ranges. This implies that the tremendous diversity of geomorphologies must be a consequence of anisotropic scaling, which is partially washed out in the isotropic analyses (Gagnon et al., 2003).

In the present paper, remotely sensed images from the TERRA ASTER sensor were analyzed to estimate the isotropic and anisotropic scaling properties of drainage networks settled in different lithological environment, the China Loess Plateau and the Utah Desolation Canyon. We present a method for investigating the variation of the anisotropy according to scale when the variation is independent of the location (linear GSI) and we demonstrate the benefits of such a characterization. Fourier and second-order structure function analyses are applied to get better constraints on the quantitative parameters. We then discuss the distinctions in the isotropic and anisotropic statistical scale invariant properties observed between the selected regions and propose geological explanations for the observed similar and distinct results.

The data

Remotely sensed images from the TERRA ASTER sensor (level 1A reconstructed unprocessed instrument data), in band 2 (0.63-0.69 μm) were selected over two drainage areas. The selected images had to be relatively free of urban areas, presenting homogeneous vegetation, uniform lithology and relatively dry climate. The China Loess Plateau drainage basin and river networks of the Utah Desolation

Canyon represent good images of river networks with such constraints. These areas were chosen in the satellite scenes. The images (parts of the scenes), 45 in total, are 512×512 pixels (averaged from original 1024×1024 pixels) and have a pixel resolution of 30×30 m, hence covering and area of 15.36×15.36 km^2.

Two regions were chosen in the China loess plateau, the first region on the Yellow River (Huang He River, CL and CY in Figure 1a) drainage basin west of Luliang Mountain and the second region in the west part of the Taihang mountain (CM in Fig.1a). The formation of the Loess Plateau in China dates back to 7-8 Ma, but was very intensive after about 2.6 Ma ago and in the Quaternary (DerbyShire, 2001). The average grain size composing the loess deposit and its thickness are diminishing from NW to SE, reflecting in a general way the dynamics of the transport of the loess by the dominant winds. Deposition of those particles from the atmosphere produces very loose particle packing (Derbyshire, 2001). The stability of the loess deposit is sustained in a large area mainly because of climatic conditions; the dry climate maintains under-saturated conditions of the loess deposits. The effect of rain on loess is drastic; water saturation of loess deposit causes it to disaggregate instantaneously, creating landslides and mudflows. The section selected in the loess plateau over the Yellow River (CL and CY) is mainly composed of several meters thick loess deposits (Porter, 2001). This area of the loess plateau is displaying a dendritic type river network, demonstrating the great erodibility of the loess deposit. The images chosen in this Chinese area are separated in two groups: images of the mainland where the drainage is less developed (CL, Fig. 2a) and images of the more develop Yellow River network (CY, Fig. 2b). The second Chinese area chosen over the Loess Plateau is near the Taihang Mountains (CM, Fig 2c), where the loess deposits are thinner and contain more clays. This area is also presenting a dendritic type of network, but less densely distributed than in the CL area, possibly due to thinner loess deposit and the effect of the shallow underlying hard rock basement. The Taihang Mountains are mainly composed of granite and gneiss (Zunyi et al. 1986). Images were chosen in the mountains part and loess plateau (CM, Fig. 2c). Both Chinese regions are in semi-arid warm temperate conditions, receiving around 300-600 mm of annual precipitations and having mean annual temperatures around 2-6 °C (Wang and Takahashi, 1998).

The region chosen in Utah, the Desolation Canyon, is shown in figure 1b. An example of a selected image is shown in figure 2d (UT). The Green River cuts deep in this area where 5000 m of sediments were deposited in an ancient basin, the Uinta Basin paleogene deposits, a Laramide downwarp formed by structural disruption of the foreland region during latest Cretaceous and Paleogene time (Dinckinson et al., 1985, Franczyk et al, 1991). The Uinta Basin depositional facies was a lacustrine environment where episodic water level fluctuations causing rapid shift in the deposit regime created markedly cyclic patterns of fluvial and lacustrine sedimentation. The sediments are mainly composed of interbeded formation of shale, siltstone and sandstone. Hence, the river network, since lying on hard rock, tends to be structurally controlled. The climatic condition in this area is similar to China, a semi-arid environment receiving around 300-400 mm of annual precipitation and annual temperatures averaging 1-7 °C.

Methodology

Investigation of the scaling properties of each image was done with spectral analysis. The spectral energy density $P(k)$ is the ensemble-averaged, square modulus of the Fourier transforms of the images; the energy spectrum $E(k)$ is the angle-integrate of $P(k)$. If isotropic scaling is respected, then $E(k)$ can be written as:

$$E(k) \propto k^{-\beta} \tag{1}$$

where β is the scale invariant Fourier exponent and k the spatial wave number in cycle/meter (or cycle/pixel). Because of the angle-integration, these statistical analyses are isotropic and washout most of the anisotropy.

The investigation of the anisotropic scaling has been done with two different methods. Fourier Transform images (FT) are produced and smoothed to facilitate the drawing of anisotropic contours. Images were also produced from the second order structure functions (SF) defined as:

$$S_q(\Delta x, \Delta y) = \left\langle \left| \tau(x+\Delta x, y+\Delta y) - \tau(x,y) \right|^q \right\rangle \tag{2}$$

where τ(x,y) is the intensity of the field at each pixel, q is the moment order (2 in our case), $\langle ... \rangle$ denotes the ensemble-average, Δx and Δy the increments in the x and y directions. Similarly to the $E(k)$, an isotropic structure function can be calculated by averaging $S_q(\Delta x, \Delta y)$ over all angle about $(\Delta x, \Delta y)=(0, 0)$, yielding $S_q(l)$ where $l = \sqrt{\Delta x^2 + \Delta y^2}$. Scaling in the generalized structure function exists when:

$$S_q(l) \sim l^{\xi(q)} \tag{3}$$

where $\xi(q)$ is the structure function scaling exponent.

In a self-similar system, zooming into the structures will not change the statistics in scaling power law ways. In order to obtain the same simple relation between large and small structures in anisotropy scaling system, the zoom must be accompanied by a compression and/or rotation as a function of scale. When facing anisotropy for scaling structures, the generalized scale invariance (GSI) method as developed by Schertzer and Lovejoy (1985) is a powerful framework. The anisotropic scaling can be described by a scale-changing operator T_λ, which relates the statistical anisotropic properties of a field from one scale ratio λ to another. The operator T_λ may be written such as:

$$T_\lambda = \lambda^{-G} \tag{4}$$

where G is a generator that takes the form of the identity matrix for the isotropic case. A second required element is a family of balls that cover the space and are modified by the scale-changing operator. Definition of the scale ratios can be done via those balls as the square root of their area. In an isotropic case, all the balls are the same shape, and in the simplest case, circles. If anisotropy is present in a system, we are assuming that at one specific scale the system is isotropic, and this can be defined by the sphero-scale l_s. Scale-changing operation T_λ, on this sphero-scale will produce a family of balls that are commonly associated to ellipses. The images analyzed in this study are two-dimensional. Assuming that G is a position-independent matrix (linear GSI), it can be written as a 2-D matrix or a linear combination of basic quaternions-like elements (Schertzer and Lovejoy, 1985; Lovejoy and Schertzer, 1985):

$$\boldsymbol{G} = d\mathbf{1} + c\mathbf{K} + f\mathbf{J} + e\mathbf{I} \tag{5}$$

where

$$\mathbf{1} = \begin{pmatrix} 1 & 0 \\ 0 & 1 \end{pmatrix}, \mathbf{K} = \begin{pmatrix} 1 & 0 \\ 0 & -1 \end{pmatrix}, \mathbf{J} = \begin{pmatrix} 0 & 1 \\ 1 & 0 \end{pmatrix}, \mathbf{I} = \begin{pmatrix} 0 & -1 \\ 1 & 0 \end{pmatrix} \tag{6}$$

hence:

$$G = \begin{pmatrix} d+c & f-e \\ f+e & d-c \end{pmatrix} \tag{7}$$

where c and f are associated to the stratification, e to the rotation and d to the general contraction of the system (d=1 for simplification, Pflug et al. (1993)). The general qualitative behavior of linear GSI is determined by:

$$a^2 = c^2 + f^2 - e^2 \tag{8}$$

Two different cases can be described, when $a^2 > 0$ the stratification is dominant; stretching of the structures dominates, with rotation never exceeding $\pi/2$. When on the contrary, $a^2 < 0$, the rotation is dominant, the balls, or ellipses rotates as the scale changes through an infinite angle of rotation (although only a finite amount of rotation is permissible for a total finite scale ratio). When rotation and stratification both act in a system, they can sometimes give a^2 values near zero, since they counteract each other.

The characterization of the GSI parameters as demonstrated in Lewis et al. (1999) with a technique called the scale invariant generator involved the fitting of theoretical equations using *G* and the unit ball (the ensemble average spectral energy density generated by GSI parameters), which is then compared to the real spectra of the image (either through FT or SF images) using least-square method. In this paper, contours are fitted to the FT images (and SF images), and the GSI parameters are then extracted from these analyzed contours (Fig. 3). To each contour in this image, ellipses are best fitted and the long axis A, the short axis B and the orientation θ are estimated. The ellipticity is calculated for each contour as the following:

$$\varepsilon = \frac{A-B}{A} \tag{9}$$

and, in the GSI, according to the following relation (see Pflug et al. (1993)):

$$\zeta = \sqrt{\varepsilon/(\varepsilon+1)} \tag{10a}$$

which can be rewritten such as:

$$\zeta = \sqrt{\sqrt{A/B} - \sqrt{B/A}} \tag{10b}$$

In stratification dominance, when $a^2>0$ an when there exists a roughly isotropic scale, the ellipticity may be related to the anisotropic scaling GSI parameters via:

$$\zeta^2 = 2\sqrt{c^2+f^2}\,\frac{\sinh^2(au)}{a} \tag{11}$$

where $u = \log \lambda$, $\lambda = l/l_s$, l is the scale and l_s is the sphero-scale (Pflug et al., 1993). In rotation dominance, when $a^2<0$, the absolute value of a is used. Simplifying the equation using Taylor expansion, ignoring the cubic and higher order terms and using $u = \ln l - \ln l_s$ we obtain:

$$\zeta = (2|a|\sqrt{c^2+f^2})^{1/2}(\ln l - \ln l_s) \tag{12a}$$

or:

$$\zeta = \zeta_0 + \zeta_1 \ln l \tag{12b}$$

where $\zeta_0 = -\ln l_s (2|a|\sqrt{c^2+f^2})^{1/2}$ and $\zeta_1 = (2|a|\sqrt{c^2+f^2})^{1/2}$. This expansion is valid as long as:

$$|u| < \frac{\sqrt{6}}{a} \tag{13}$$

Since Pecknold et al. (1997) analysis of various geophysical fields showed that $|a|$ is frequently of the order of 0.1 and usually < 0.2, this implies that the following is applicable if we are within a factor of 10^5 of the sphero-scale ($l/l_s < e^{\sqrt{6}/0.2}$). The result of equation 10b is plotted against the scale ratio λ equivalent to square root of the area of the corresponding ellipses (this correspond to using d=1, see Lewis et al. (1999)). From the data and equation 11, the slope ζ_1 and the intercept ζ_0 are retrieved.

In this case, the parameter ζ_1 represents the differential anisotropic variation from scale to scale of the system. Then, the sphero-scale l_s is extracted as:

$$l_s = e^{-\zeta_0/\zeta_1} \tag{14}$$

When considering the angle variation of the balls, Pflug et al. (1993) expressed it as:

$$\theta = \frac{1}{2}\tan^{-1}\frac{f}{c} - \frac{1}{2}\tan^{-1}\left(\frac{e}{a}\tanh(au)\right) \tag{15}$$

Expanding this expression and ignoring cubic and higher order terms gives:

$$\theta \approx \frac{1}{2}\tan^{-1}\frac{f}{c} - \frac{1}{2}eu \tag{16}$$

This approximation is valid as long as:

$$|u| < \sqrt{\frac{3}{(c^2+f^2)}} \tag{17}$$

which is very close to the previous condition. Then, according to the above, we can represent the angle variation as:

$$\theta = \theta_0 + \theta_1 \ln l \tag{18}$$

where $\theta_0 = \frac{\varphi}{2} + \frac{e}{2}\ln l_s$ and $\theta_1 = -\frac{e}{2}$, φ being equal to $\tan^{-1}\frac{f}{c}$. From equations 8, 10 and the parameter e retrieved from θ_0, we can rewrite ζ_0 and ζ_1 according to the following relations:

$$\zeta_0 = -\sqrt{2r\sqrt{|r^2 - e^2|}}\,\ln l_s \tag{19}$$

and

$$\zeta_1 = \sqrt{2r\sqrt{\left|r^2 - e^2\right|}} \tag{20}$$

with $c = r\cos\varphi$, $f = r\sin\varphi$ and $r^2 = a^2 + e^2$. Finally, the solution of equation 19 is:

$$r^2 = \frac{e^2 + \sqrt{e^4 + \zeta_1^4}}{2}, a^2 > 0 \tag{21a}$$

and

$$r^2 = \frac{e^2 \pm \sqrt{e^4 - \zeta_1^4}}{2}, a^2 < 0 \tag{21b}$$

hence, when $\left|\zeta_1\right| > \left|e\right|$, we must have a stratification dominant regime ($a^2 > 0$) and a unique solution for r^2. However, when $\left|\zeta_1\right| < \left|e\right|$, we have two additional possible solutions for $a^2 < 0$. In this case, we could consider the third order term of the expansion of the expression of ξ^2 (equation 11) to establish the sign of a^2.

Results

Estimation of isotropic spectral exponent β values was done between 240 m ($\log(k)$=1.81) and 3840 m ($\log(k)$=0.3) for all data sets. Many of the images exhibit scaling behavior from 120 m to 3840 m. However, the isotropic scaling of the overall data is more systematically characterized between 240 m and 3840 m. We are facing the poor quality of the ASTER data, where smoothing at the highest resolutions is important. Laferrière and Gaonac'h (1999) and Beaulieu and Gaonac'h (2001) made similar observations on the scaling of remotely sensed data. Examples of energy spectra of each data set are presented in figure 4. The averaged β exponents show a trend increasing from CL (β=0.09) to CM (β=0.91) (Fig. 4, Table 1). While the isotropic analyses demonstrated the presence of scale invariance as stated above, and also provided distinct scaling characterization between the CL images and the others, we are also concern by the anisotropic scaling aspect of the networks, if it could supply more information for their distinction.

Evaluation of the ζ_1 parameter (differential anisotropic variation) for all images was done with the two FT and SF methods, as described above. Contours below the 120 m scale were discarded because of data smoothing problems as described above. Data points between 120 m and 240 m were used for extracting statistical properties since the GSI analyses did not demonstrate sensitive break in this range as observed for the energy spectra. Hence, we decided to keep all the data above 120 m resolution for better constrain on the statistics. Examples are shown in figure 5. In some cases, anisotropy reaches a maximum and then starts to decreases at higher scales; in these examples, the larger range of scales is selected. For example, in figure 5a, the FT data point (and SF) for UT data show this behavior, the interval chosen for the evaluation of the slope was between scales of 115 m ($\ln(l)$=4.75) and 1550 m ($\ln(l)$=7.35). These cases correspond to relatively strong anisotropy.

When a difference in the numerical values of opposite sides of an image is present (border discrepancy), a window effect is created in the FT and SF representations. This produces divergent anisotropic values for larger structures between the FT and SF methods, as shown in figure 5b by the data set CM for scales above 1000 meters ($\ln(l)=6.90$). The use of windowing technique in FT (Hanning, Welch, Barlett) was avoided since they are done isotropically, hence possibly affecting the anisotropy that we are analyzing. Finally, another discrepancy between the two FT and SF methods may arise when images are nearly isotropic ($\zeta(l)$ very low all over the scales). In these cases large structures are difficult to contour in SF images due to poor statistics. It will provoke the scarcity of the SF data points to the larger sizes of the distribution, hence affecting the evaluation of the slope (ζ_1), like displayed in figure 5c, where only two data points are present over a scale of 350 m ($\ln(l)=5.86$). Gaonac'h et al. (2003) found similar behavior with other type of images. This problem is of less importance in the FT images hence we decided to concentrate on the FT results for the regressions and retrieval of the parameters.

In figure 6a and 6b, the ζ_1 and θ_1 values, which characterize the rate at which structures are "stretched" with scale and at which they rotate with scale respectively, are plotted against β. The β values give an opportunity to discriminate the very dendritic China CL data set from the other sets (CY, CM and UT). The anisotropic ζ_1 values separate the CL and CM groups ($\zeta_1 < 0$) from the CY and UT groups ($\zeta_1 > 0$), especially when considering the average of each group (larger symbols). The θ_1 value of all the data is confined between -1 and 1, except for one point (Fig. 6b). This parameter does not show any differentiation in between the investigated data ensembles. The plot of the anisotropy ($\zeta(l)$) at a fixed scale of 960 meters (1/16 of the image size) versus the β values demonstrated a good discrimination between UT group on one hand and the China CM, CL and CY groups on the other hand (Fig. 7). This characteristic scale possesses good statistical behavior in both analysis (FT and SF).

The parameter a^2 is a measure of the differential anisotropic variation of a system, including the stratification/contraction and rotation of the structures $a^2 = c^2 + f^2 - e^2$. The a^2 values range is between -0.01 and 0.10, in which most of the values approach zero. While the GSI method presently applies to structures and fields that are not too anisotropic, a^2 values around 0 confirm the condition while expressing the scaling. The sphero-scale l_s estimated values are in general beyond the observed range of scales for the CL and CM groups because of the negative ζ_1 values of these images, whereas the CY and UT groups show l_s values around 64 and 4 meters, respectively.

Errors on the evaluation of the parameters β, ζ_1, θ_1 and a^2 on each image were evaluated by the effect of inclusion/exclusion of data point on the values of the respective slopes; they are around 0.01, 0.02, 0.05 and 0.003 respectively. The largest errors were on the CL data set, which has the lowest β values.

Discussion

The presence of anisotropy and scale-invariant anisotropy demonstrated in this investigation over two different drainage areas proved to be very insightful. Important new scale invariant parameters are introduced that are statistically quantifying morphological differences: ζ_1, the differential anisotropic variation with scale, $\zeta(l)$ the anisotropy of the structures at a fixed scale. These parameters are linked by rotation and stratification of the textures/structures acting during scale-changing operations. The log-linear relationship between these parameters is predicted by the GSI model proposed by Schertzer and Lovejoy (1985) and Lovejoy and Schertzer (1985). As shown in figure 6a and 7, the use of isotropic scaling β values, ζ_1 and $\zeta(960\text{ m})$ parameters furnish robust distinction between the various data groups (CL, CM, CY and UT). First, the β values ($\beta \leq 0.4$) yield a clear distinction between the China CL group and the others (Fig. 6a). The differential anisotropy provide information to discriminate between the China CY and CM group. Finally, the anisotropy at the characteristic scale of 960 m gives further discrimination between the Utah in one hand and the China groups CY and CM on the other hand.

The images from the China Loess Plateau and the Utah desolation canyon possess two different type of drainage according to conventional geomorphologic classification. These two kinds of morphologies have very different drainage density, being very densely distributed in the China data ensembles, and a lot coarser, less dense in the UT images. The two regions also possess very different ground properties, being very friable in the loess deposit of China compared to the hard rock settings in the Utah. In the thick loess deposit area, remobilization of the loess is more then often done by slope failure and flow-side in instantaneous event during high rain rate (Derbyshire, 2001). The CL images are selected in poorly developed drainage part (beginning of small rivers) compared to the more developed CY images, which exhibit the large Yellow River system. On the east part of the studied China region, in the Loess Plateau near the Taihang Mountains (CM images), the loess deposit is thinner hence giving the underlying rock strong response to the final drainage morphology in comparison with the CL area. On the contrary, in the Utah region where the geological setting is composed of sedimentary rock such as sandstones and limestones, the river system is more structurally dependent; the ridge-type textures in the images are all well aligned and of similar size compared to the one in China (Fig. 2).

This difference between the CL group and the other is well demonstrated by figure 6a. The distinct lower β values of the CL images (CL, average β=0.09) may be explained by the thickness of the deposit of loess around the Yellow River, creating a high-density drainage system. The low β values indicate the paucity of large structures compared to smaller ones. β is then increasing for the other China data sets and the Utah images, reflecting the presence of more large structures compared to CL images (CY, CM and UT, average β=0.76, 0.91 and 0,85 respectively). When comparing CY to CL for example, its higher β values can easily be explained by the presence of the large developed rivers in its images, increasing the proportion of large structures compared to small one in the energy spectrum (Fig 4). Similar observations on the maturity of different portions of a river network with β values were also found by Beaulieu and Gaonac'h (2002) on the Ethiopian Plateau. The CM images, which demonstrate higher β values but present similar dendritic fluvial geomorphology as the CL images, could possibly indicate the combined effect of the loess deposit and the underlying hard rocks, which may favor large structures over small ones. These images were partly selected in a mountainous area composed of granites and gneisses, covered by a thin layer of loess deposits, and partly on the plateau area where the loess deposit is less thick compared to the CL and CY areas. The presence of underlying hard rocks leads to higher β values, showing their impact on the development of the river system. Maître and Pinciroli (1999) also suggested a possible link between the fractal dimension and geomorphologic aspects of the surface, such as soil composition and friability, where low fractal dimensions would be associated with friable environment and high values with hard rock settings. Hence, the more densely dendritic the network is, the lower the β values become.

The CL and CM groups have negative differential anisotropic (ζ_1 values) variations reflecting that structures exhibit less anisotropy with larger scales (Fig. 6a). In the CL group, images show no or practically no large structures, as previously explained by their low β values. In the case of the CM images, large structures are present, but they seem to radiate in every directions compared to smaller one, hence showing no preferred orientation compared to the small ones. This observation further enhances the fact that they possess similar dendritic morphology, which is not so deeply developed. They represent the source of drainage areas. On the other hand, CY and UT structures exhibit higher anisotropy with larger scales (Fig. 6a). This difference reflects the dominance of large preferentially oriented rivers on the statistics without breaking the scaling. The CY and UT areas correspond to more mature river networks. The anisotropy at fixed scale (ζ(960 m)) help for the differentiation of the Chinese images compared to the Utah images (Fig. 7). All the China groups related to the same drainage area possess similar averaged ζ(960 m) values (CL=0.72, CY=0.74 and CM=0.56) while the Utah shows a higher ζ(960 m) value (UT=1.06) reflecting the more intense anisotropy at this 960 m scale. Another way to consider this result is that anisotropy can develop at smaller scales for Utah regions. This is exhibited by a smaller sphero-scale (l_s=4 meter) for UT images compared to CY images (l_s=64 meter). We suggest that this discrepancy probably reflects the difference in lithology and in the structural geology of the area, which may enhance the anisotropy at smaller scales.

Conclusion

Investigation of river networks and drainage patterns has long been pursued, mostly with topographic data sets from which the network patterns were extracted.

From these geometric sets, parameters were retrieved in order to characterize and understand the intrinsic properties of the different drainage type including their scaling and anisotropic characteristics. In this study, we used remotely sensed images in order to statistically quantify the properties of river networks. The type of soil and rock basement, the tectonics, the climate and the vegetation all influence the erosion mechanism and hence the river network geometry. The analyzed satellite images have been acquired in the visible range of the spectrum and the statistical results are thus intrinsically related to the topography of the regions via the albedo field. Weissel and Pratson (1994), with their investigation on directional topographic profile, and Weissel et al. (1995), were concerned that anisotropic morphologies could affect the statistical properties of the topography. Applying Schertzer and Lovejoy (1985) theory in GSI framework, we analyzed remotely sensed drainage areas through scaling and anisotropic scaling perspective for understanding the whole range of structures present in a river network.

The data confirm the scaling as well as the anisotropy of river network. Moreover, the anisotropy does not create any break in the scaling but produce a log-linear relationship between the differential anisotropy and the scale. The two statistical FT and SF methods provided similar results, which strengthen the quantitative characterization of the two geographic river networks. An increase in β is related to the development of complexity of the network type. We suggest that a more developed, mature river network produces a stronger differential anisotropy. All the images of a same river network have overall similar anisotropy (same $\zeta(l)$), different from one geological setting to another. These new very promising results open a new avenue for quantitative geological understanding. Further research will have to be conducted on the aspect of non-linearity of anisotropic variations (non linear GSI), where the characteristics of the image may change according to the location of the analyses.

References:

Beaulieu, A. and Gaonac'h, H., Scaling of differentially eroded surfaces in the drainage network of the Ethiopian plateau, Remote Sensing of Environment, 82, 111-122, 2002.

Bell, T.H., Statistical feature of sea-floor topography. Deep-see Reasearch, 22, 883-892, 1975.

Brown, S.R., A note on the description of surface roughness using fractal dimension, Geophys. Res. Letters, 14, 1095-1098, 1987.

Chase, C.G., Fluvial landsculpting and the fractal dimension of topography, Geomorphology, 5, 39-57, 1992.

Derbyshire, E., Geological hazards in loess terrain, with particular reference to the loess regions of China, Earth-Science Review, 54, 231-260, 2001.

Dickinson, W.R., Lawton, T.F. and Inman, K.F., Sandstone detrical modes, central Utah foreland region: stratigraphic record of cretaceous-paleogene tectonic evolution, J. Sedimentary Geology, 56, 276-293, 1986.

Dodds, P.S. and Rothman, D.H., Scaling, universality, and geomorphology, Annu. Rev. Earth Planet. Sci., 28, 571-610, 2000.

Foufoula-Georgiou, E. and Sapozhnikov, B., Anisotropic scaling in braided rivers: an integrated theoretical framework and results from application to an experimental river, Water Ressources Res., 34, 863-867, 1998.

Franczyk, K.J., Hanley, J.H., Pitman, J.K. and Nichols, D.J., Paleocene depositional systems in the western Roan Cliffs, Utah, Utah Geol. Ass. Pub., 19, 111-127, 1991.

Gagnon, J.-S., Lovejoy, S. and Schertzer, D., Multifractal Earth topography. J. Geophys. Research, Solid Earth, in press.

Gaonac'h, H., Lovejoy, S. and Schertzer, D., Resolution dependence of infrared imagery of active thermal features at Kilauea volcano, Int., J. Remote Sensing, 24, 2323-2344, 2003.

Gaonac'h, H., Lovejoy, S. and Beaulieu, A., Anisotropic scale invariance characterisation of A'a and pahoehoe lava, Hawaii. In preparation, 2003.

Harvey, D.C., Gaonac'h, H., Lovejoy, S. and Schertzer, D., Multifractal characterization of remotely sensed volcanic features: a case study from Kilauea volcano, Hawaii, Fractals, 10, 265-274, 2002.

Horton, R.E., Erosional development of streams and their drainage basins: hydrophysical approach to quantitative morphology, Geol. Soc. Am. Bull., 56, 275-370, 1945.

Huang, J. and Turcotte, D.L. Fractal mapping of digitized images: application to the topography of Arizona and comparisons with synthetic images, J. Geophys. Res., 94, 7491-7495, 1989.

Klinkenberg, B. and Goodchild, M.F., The fractal properties of topography: a comparison of methods, Earth Surface Processes And Landforms, 17, 217-234, 1992.

La Barbera, P. and Rosso, R., On the fractal dimension of stream networks, Water Ressourses Res., 25, 735-741, 1989.

Laferrière, A. and Gaonac'h, H., Multifractal properties of visible reflectance fields from basaltic volcanoes, J. Geophys. Res., 104, B3, 5115-5126, 1999.

Lavallée, D., Lovejoy, S., Schertzer, D. and Ladoy, P., Nonlinear variability of Landscape topography: Multifractal analysis and simulation, in Fractals in Geography, edited by De Cola, L. and Lam N., pp. 158-192, Prentice-Hall, Englewood Cliffs, NJ, 1993.

Lewis, G.M., Lovejoy, S., Schertzer, D. and Pecknold, S., The scale invariant generator technique for quantifying anisotropic scale invariance, Computers and Geosciences, 25, 963-978, 1999.

Lovejoy, S. and Schertzer, D., Generalized scale invariance in the atmosphere and fractal models of rain, Water Ressources Res., 21, 1233-1250, 1985.

Lovejoy, S., Schertzer, D. and Pflug, K., Generalized scale invariance and differential rotation in cloud radiances, Physica A, 185, 121-128, 1992.

Lovejoy, S., Schertzer, D., Tessier, Y. and Gaonac'h, H., Multifractals and resolution-independent remote sensing algorithms: the example of ocean colour, Int. J. of Remote Sensing, 22, 1191-1234, 2001.

Lovejoy, S., Pecknold, S. and Schertzer, D., Stratified multifractal magnetization and surface geomagnetic fields-I. Spectral analysis and modelling, Geophys. J. Int., 145, 112-126, 2001.

Maître, H. and Pinciroli, M., Fractal characterization of a hydrological basin using SAR satellite images, IEEE Trans. Geos. Rem. Sens., 37, 175-181, 1999.

Malinverno, A., Fractals and ocean floor topography: a review and a model, in Fractals in Earth Sciences, edited by C.C. Barton and P.R. La Pointe, pp. 107-130, Plenum Press, New York, 1995.

Mark, D.M. and Aronson, P.B., Scale-dependent fractal dimensions of topographic surfaces: an empirical investigation, with applications in geomorphology and computer mapping, Math. Geol., 16, 671-683, 1984.

Pecknold, S., Lovejoy, S., Schertzer, D. and Hooge, C., Multifractals and resolution dependence of remotely sensed data: GSI to GIS, in Scale in Remote Sensing and GIS, edited by Quattrochi, D.A. and Goodchild, M.F., pp. 361-394, Boca Raton, FL, CRC Press, 1997.

Pecknold, S., Lovejoy, S. and Schertzer, D., Stratified multifractal magnetization and surface geomagnetic fields-II. Multifractal analysis and simulations, Geophys. J. Int., 145, 127-144, 2001.

Pelletier, J.D., Self-organisatio and scaling relationships of evolving river networks, J. Geophys. Res., 104, 7395-7375, 1999.

Pflug, K., Lovejoy, S. and Schertzer, D., Differential rotation and cloud texture: analysis using generalized scale invariance, J. Atmos. Science, 50, 538-553, 1993.

Porter, S.C., Chinese loess record of monsoon climate during the last galcial-interglacial cycle, Earth-Science Reviews, 54, 115-128, 2001.0

Power, W.L. and Tullis, T.E., Euclidean and fractal models for the description of rock surface roughness, J. Geophys. Res., 96, 415-424, 1991.

Rodriguidez-Iturbe, I. And Rinaldo, A., 1997. Fractal river basins: Chance and self-organisation. Cambridge, UK: Cambridge Univ. Press. 547 pp.

Schertzer, D. amd Lovejoy, S., Generalised scale invariance in turbulent phenomena, Phys. Chem. Hydrodyn. J., 6, 623-635, 1985.

Strahler, A.N., Quantitative analysis of watershed geomorphology, Eos Trans., AGU, 38, 913-20, 1957.

Turcotte, D.L., A fractal interpretation of topography and geoid spectra on the Earth, Moon, Venus and Mars, Proc. Lunar Planet. Sci. Conf., 17th, part 2, J. Geophys. Res., 92, E597-E601, 1987.

Van Put, A., Vertes, A., Wegrzynek, D., Treiger, B. and Van Grieken, R., Quantitative characterization of individual particles surfaces by fractal analysis of scanning electron microscope images, Fresenius J. Anal. Chem., 350, 440-447, 1994.

Vening Meinesz, F.A., A remarkable feature of the Earth<s topography, origin of continents and oceans. Proc. Koninkl. Ned. Akad. Wetensch., ser. B, 55, 212-228, 1951.

Wang , Q. and Takahashi, H., Regional hydrological effects of grassland degradation in the Loess Plateau of China, Hydological Processes, 12, 2279-2288, 1998.

Weissel, J.K. and Pratson, L.F., The length-scaling properties of topography, J. Geophys. Res., 99, 13997-14012, 1994.

Weissel, J.K., Malinverno, A., Harding, D.J. and Karner, G.D., Erosional development of the ethiopian Plateau of northeast Africa from a fractal analysis of topography, in Fractals in Petroleum Geology and Earth Processes, edited by C.C. Barton and P.R. La Pointe, pp. 127-142, Plenum Press, New York, 1995.

Zunyi, Y., Yuqi, C. and Hongzhen, W., The Geology of China, Oxford Monographs on Geology and Geophysics no. 3, 303 pp., Clarendon Press, Oxford, 1986.

Table

Table 1

Averaged estimates of the statistical scaling parameters of the analyzed images and their error

	CL	**CM**	**CY**	**UT**	**error**
ave β	0.09	0.91	0.76	0.85	0.01
ave ζ_1	-0.19	-0.07	0.24	0.18	0.03
ave θ_1	-0.13	0.09	0.55	0.02	0.05
ave a^2	0.00	0.01	0.02	0.01	0.003

Figure captions:

Figure 1: a) Location of the two selected regions in the Loess Plateau of China. The ASTER flight over the Yellow River (Huang He River) contains 8 scenes, overall representing 60 km by 485 km; the CL and CY images were chosen in this section. The other ASTER flight is partly on the Taihang Mountains and is made of 5 scenes, overall representing 60 km by 304 km; the CM images were taken from this area. Map is modified after Derbyshire (2001). b) Location of the Utah data set (UT). The dark rectangle shows portion of the ASTER flight, which is composed of 3 scenes, and is 60 km by 184 km. Map modified after Dickinson et al. (1985).

Figure 2: Examples of the drainage pattern in each data groups. (a) the CL group containing 17 images, the ASTER data have been collected on October 1, 2000. (b) CY group containing 5 images, same ASTER scenes as (a). (c) the CM group containing 16 images, the ASTER data have been collected 10, 2001. (d) the UT group containing 7 images, the ASTER scenes were acquired on October 19, 2000. Each image is 512 by 512 pixels and is $15.36 \times 15.36 \text{ km}^2$.

Figure 3: Example of the fitted contours in a CY FT image. The contours shown at the bottom is a magnification of the small square in the top image. In a FT image, the small structures are depicted by the large contours, and the large ones by the small contours; they are also orthogonal to the real structures.

Figure 4: Plot of $\log_{10} E(k)$ versus $\log_{10} k$ for selected images of each group, they are shifted for a better visualization, see table 1 for average β values.

Figure 5: Plot of $\zeta(l)$ versus the scale log of the scale l for the FT and SF methods on the four different image groups (UT, CM, CL and CY) (120 meters corresponds to $\ln(l)$=4.7)

Figure 6: a) Plot of ζ_1 values versus the β values estimated from the FT method for the different groups. The large symbols represent the averaged values of each field. b) Plot of θ_1 values (in radians) versus the β values estimated from the FT method for the different groups.

Figure 7: Plot of ζ(960 m)values versus the β values estimated from the FT method for the different data ensembles.

Figure 1

a)

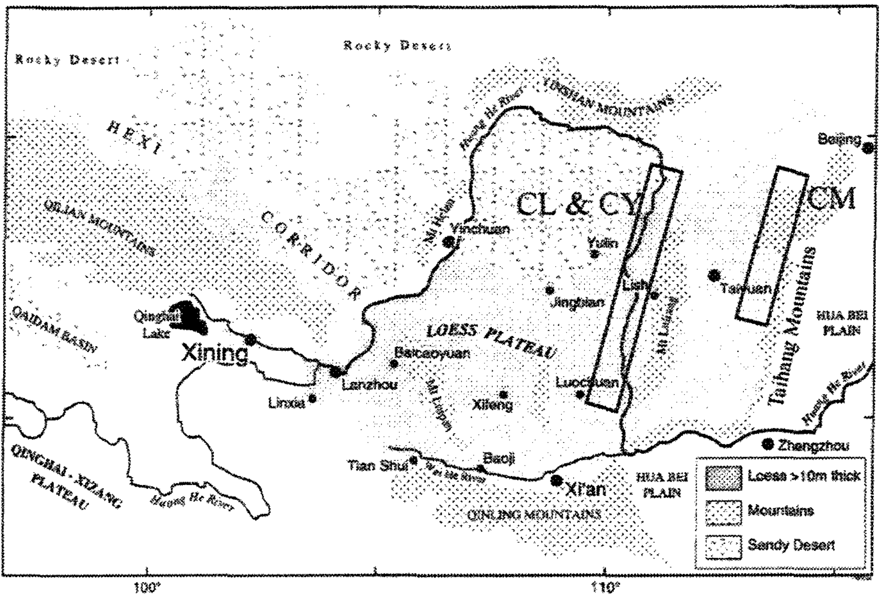
Rocky Desert
Rocky Desert
HEXI
CORRIDOR
QILIAN MOUNTAINS
QAIDAM BASIN
Qinghai Lake
Xining
Lanzhou
Linxia
Yinchuan
Mt Helan
Huang He River
YINSHAN MOUNTAINS
CL & CY
CM
Beijing
Yulin
Jingbian
Lishi
Mt Luliang
Taiyuan
Taihang Mountains
HUA BEI PLAIN
LOESS PLATEAU
Baicaoyuan
Mt Liupan
Xifeng
Luochuan
Zhengzhou
Huang He River
Tian Shui
Wei He River
Baoji
Xi'an
HUA BEI PLAIN
QINLING MOUNTAINS
QINGHAI - XIZANG PLATEAU
Huang He River
Loess >10m thick
Mountains
Sandy Desert
40°
35°
100°
110°

b)

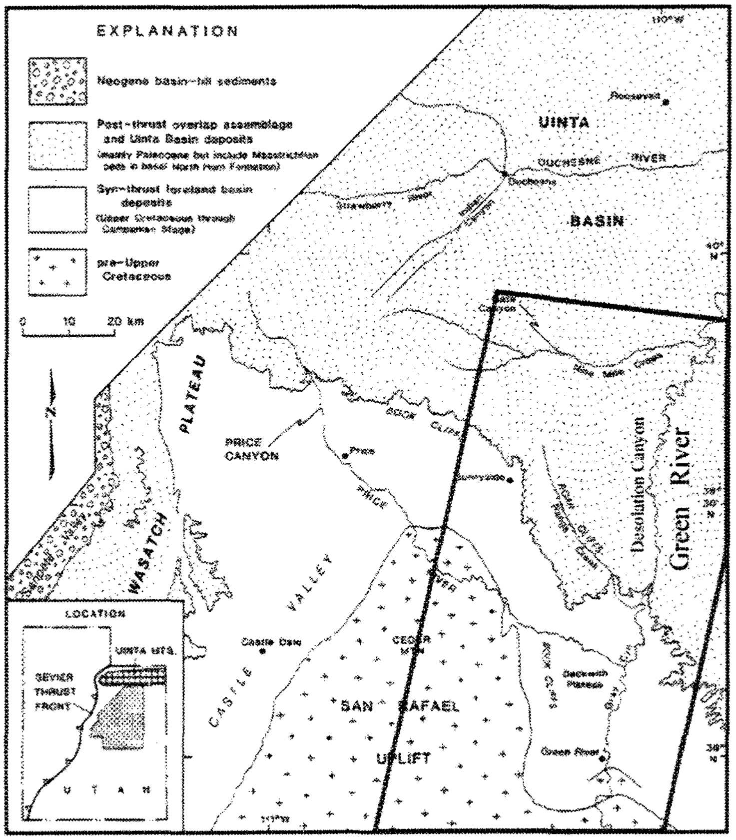
EXPLANATION
Neogene basin-fill sediments
Post-thrust overlap assemblage and Uinta Basin deposits
(mainly Paleocene but include Maastrichtian beds in basal North Horn Formation)
Syn-thrust foreland basin deposits
(Upper Cretaceous through Campanian Stage)
pre-Upper Cretaceous
0 10 20 km
N
110°W
Roosevelt
UINTA
DUCHESNE RIVER
Duchesne
Strawberry River
Indian Canyon
BASIN
40° N
Nine Mile Creek
PLATEAU
BOOK CLIFFS
PRICE CANYON
Price
PRICE
Sunnyside
ROAN CLIFFS
Desolation Canyon
Green River
39° 30' N
WASATCH
CASTLE VALLEY
Castle Dale
CEDAR MTN
SAN RAFAEL
UPLIFT
BOOK CLIFFS
Beckwith Plateau
Green River
39° N
111°W
LOCATION
UINTA MTS.
SEVIER THRUST FRONT
UTAH

Figure 2

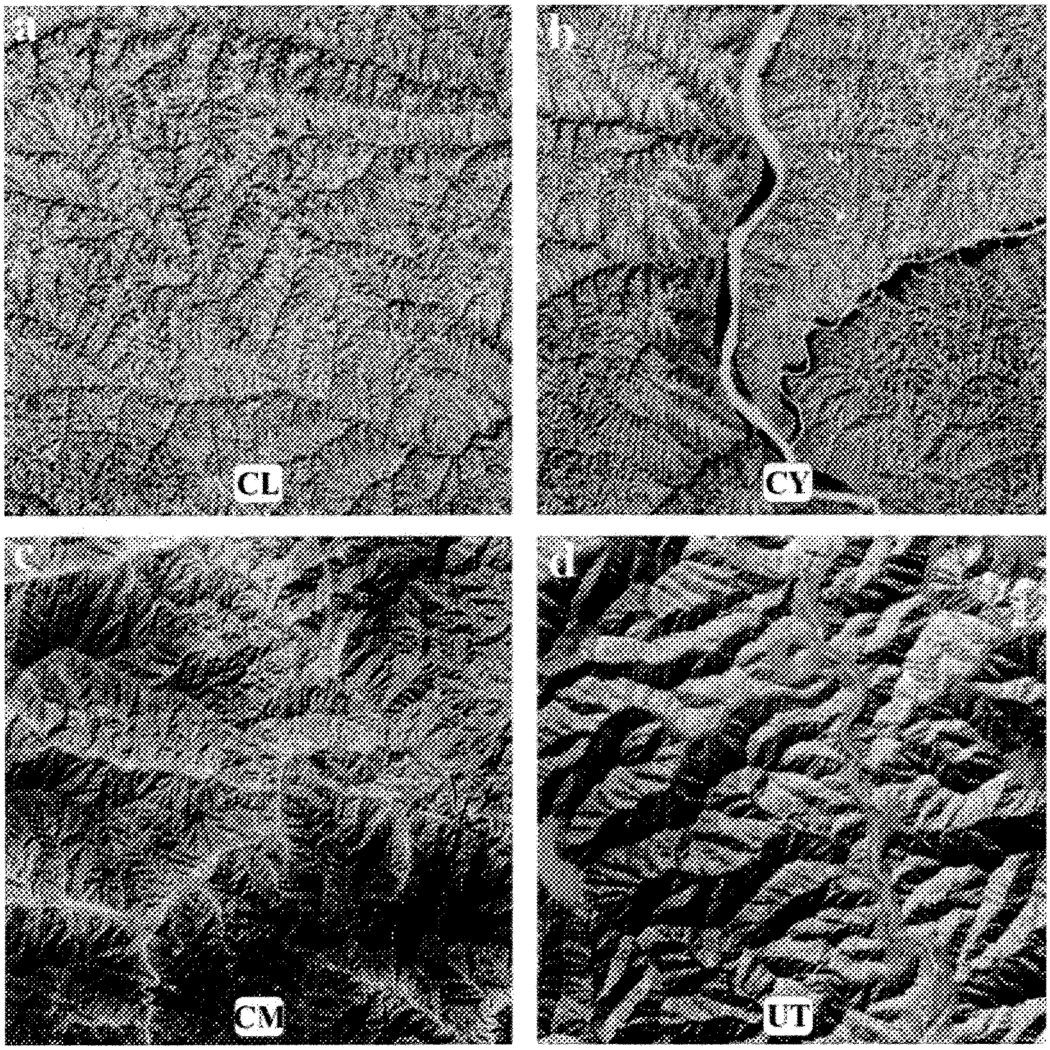

Figure 3

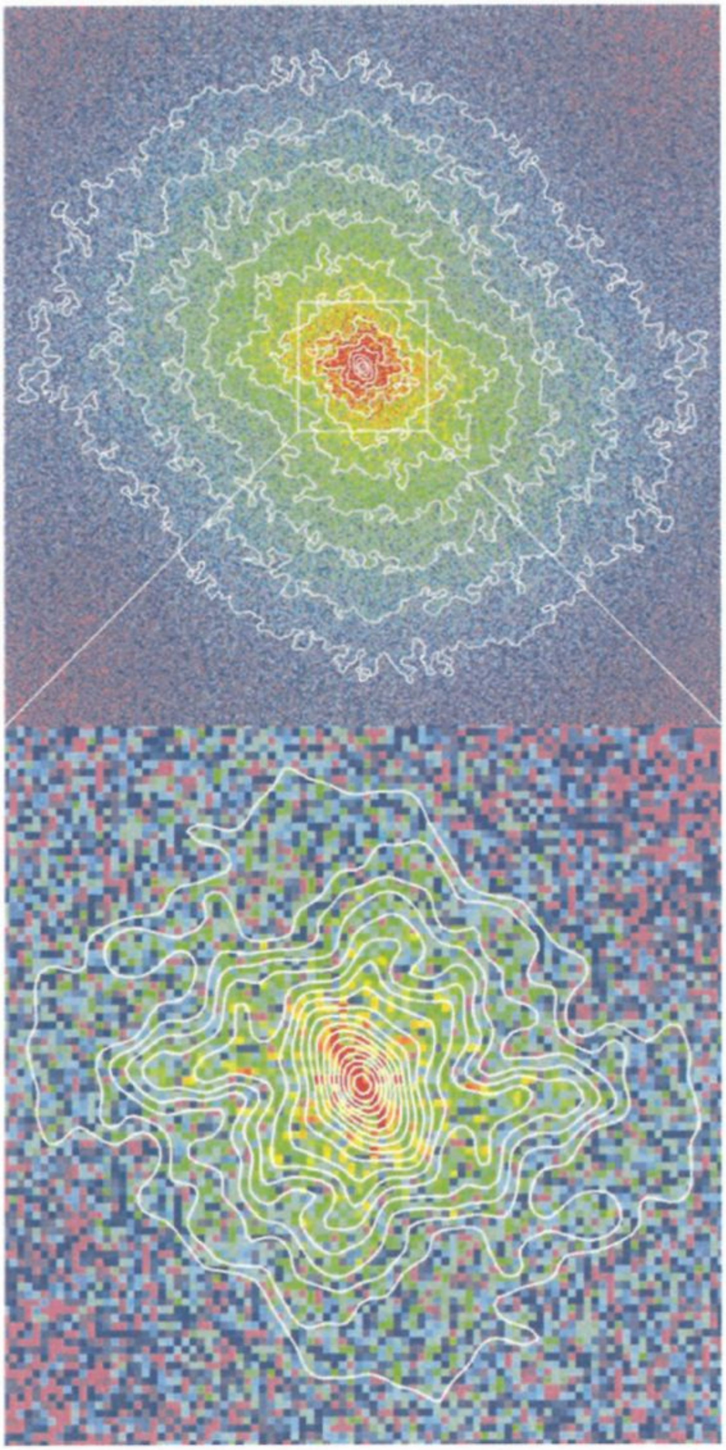

Figure 4

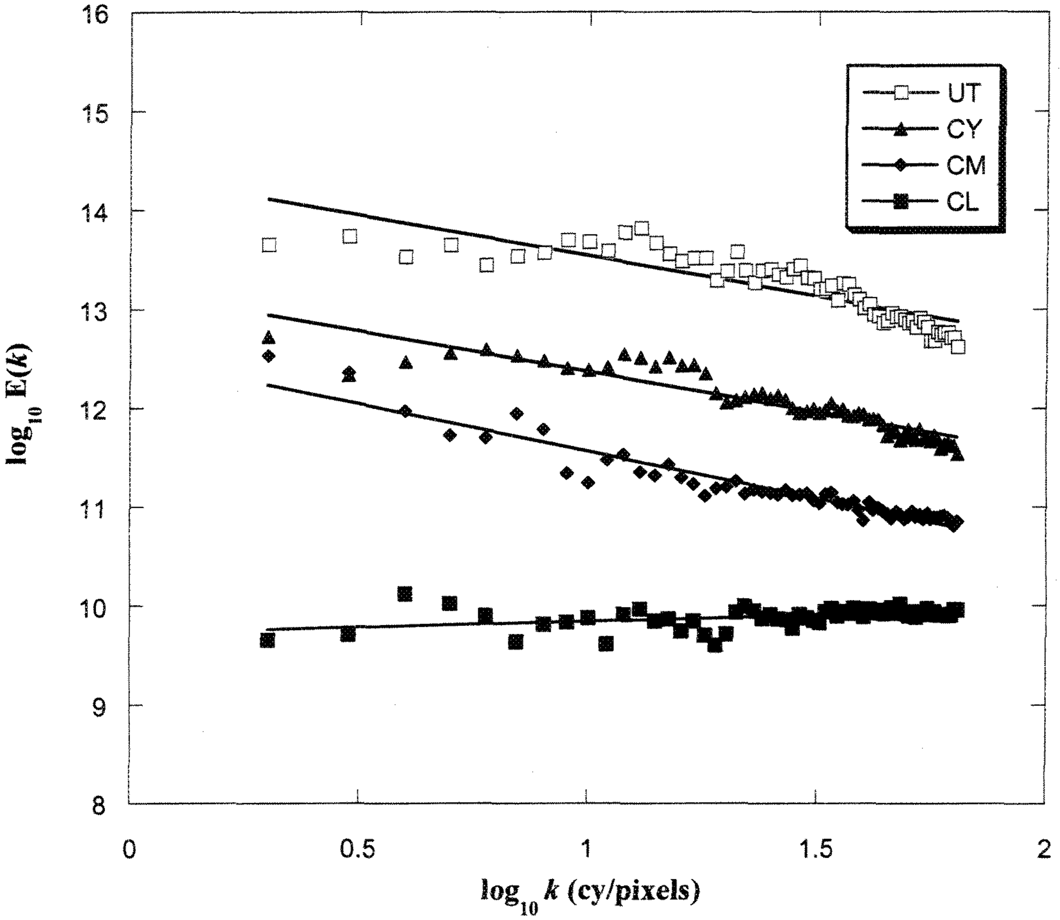
16
15
14
13
12
11
10
9
8
0
0.5
1
1.5
2
UT
CY
CM
CL
$\log_{10}$ E(*k*)
$\log_{10}$ *k* (cy/pixels)

Figure 5

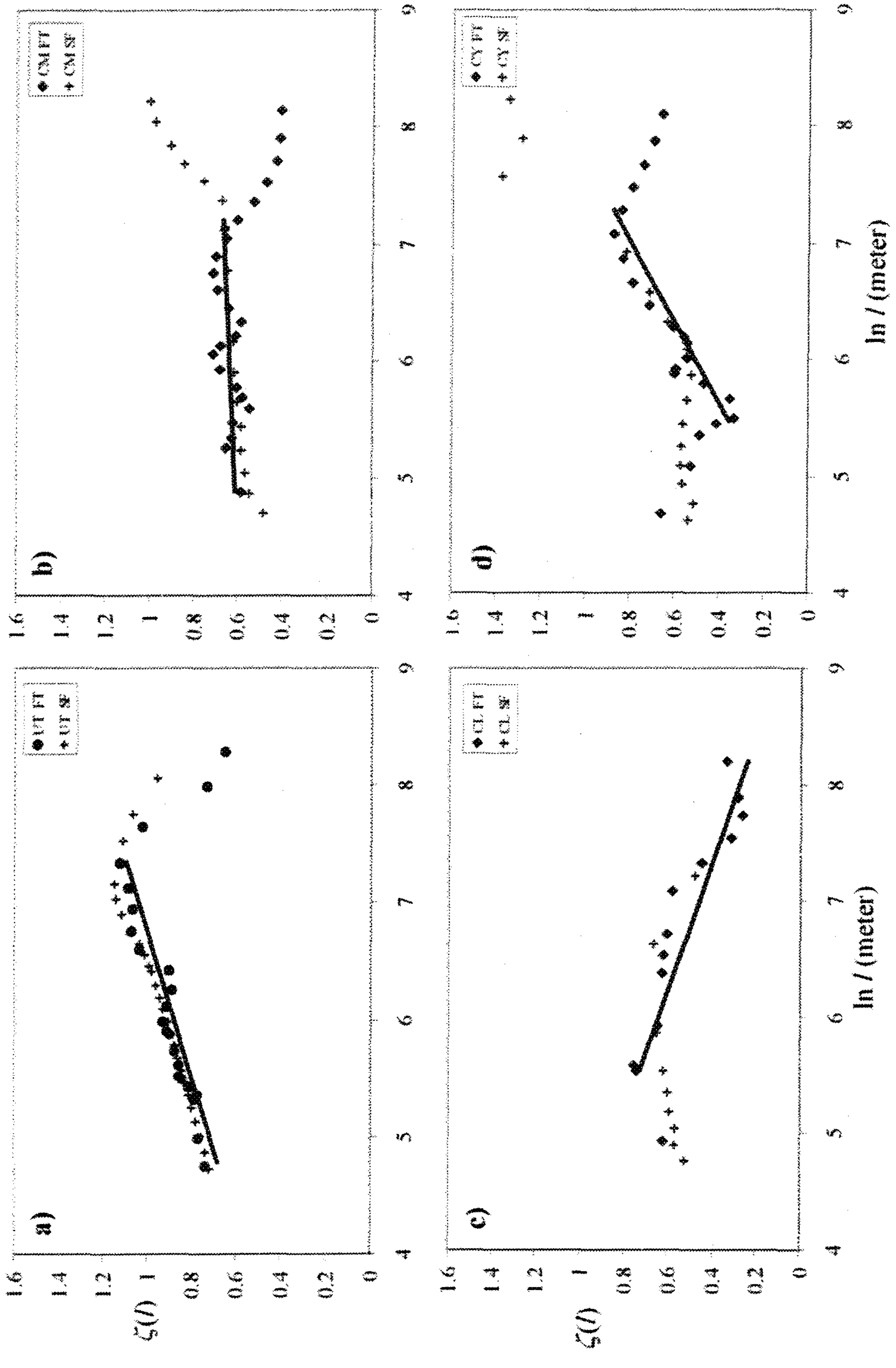
a)
● UT FT
+ UT SF
b)
◆ CM FT
+ CM SF
c)
◆ CL FT
+ CL SF
d)
◆ CY FT
+ CY SF
ζ(l)
ζ(l)
ln l (meter)
ln l (meter)
0
0.2
0.4
0.6
0.8
1
1.2
1.4
1.6
4
5
6
7
8
9

Figure 6

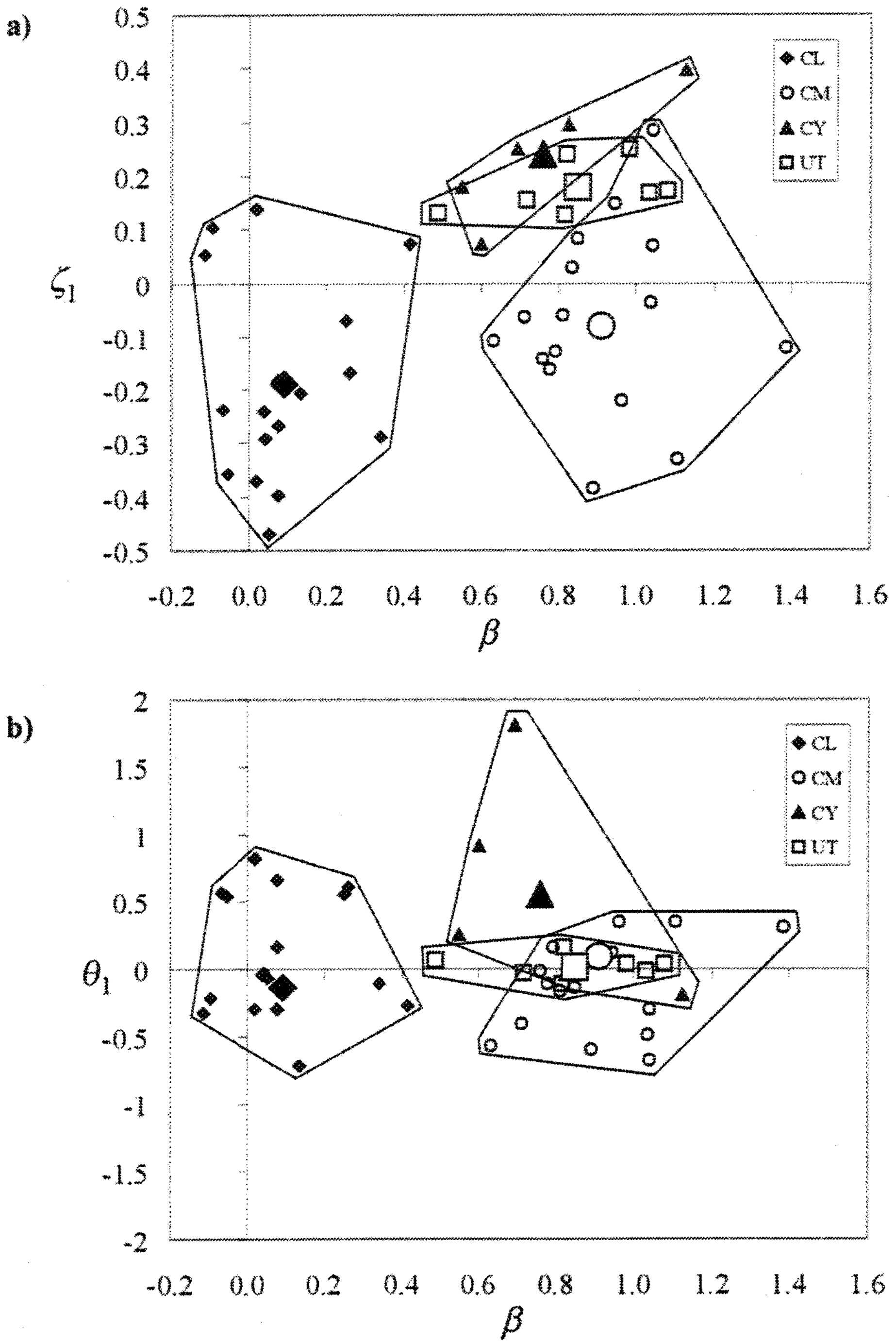
a)
0.5
0.4
0.3
0.2
0.1
0
-0.1
-0.2
-0.3
-0.4
-0.5
ζ_1
-0.2
0.0
0.2
0.4
0.6
0.8
1.0
1.2
1.4
1.6
β
◆ CL
○ CM
▲ CY
□ UT
b)
2
1.5
1
0.5
0
-0.5
-1
-1.5
-2
θ_1
-0.2
0.0
0.2
0.4
0.6
0.8
1.0
1.2
1.4
1.6
β
◆ CL
○ CM
▲ CY
□ UT

Figure 7

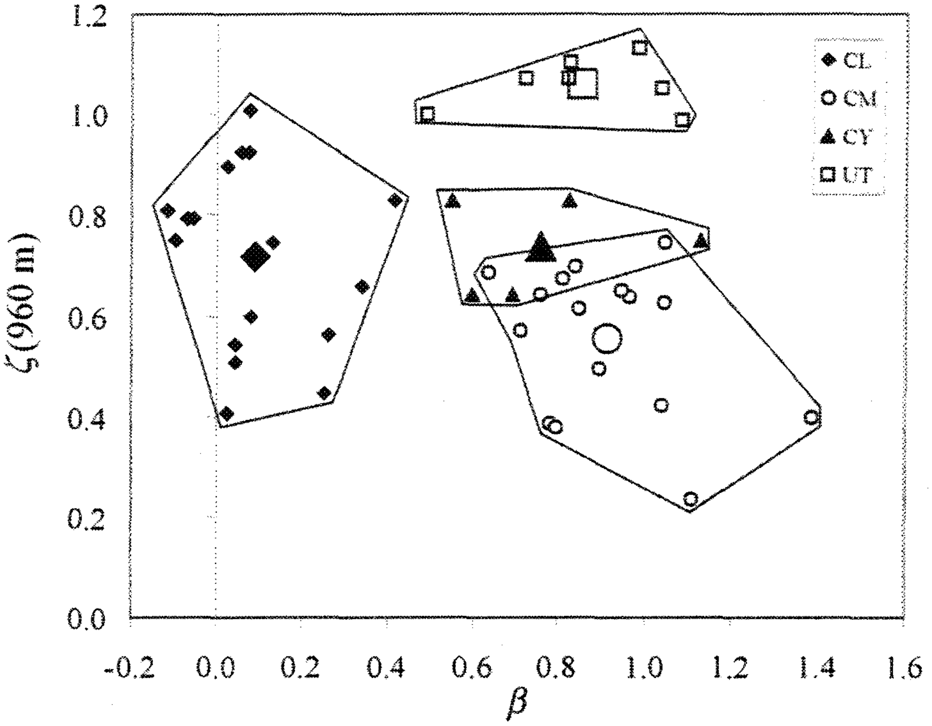

CHAPITRE 3

QUANTIFICATION DU COMPORTEMENT ANISOTROPE AVEC L'ÉCHELLE: UNE NOUVELLE FAÇON DE CARACTÉRISER LES MORPHOLOGIES DE SURFACE.

QUANTIFICATION OF THE ANISOTROPIC BEHAVIOR WITH SCALE: A NEW WAY TO CHARACTERIZE SURFACE MORPHOLOGIES.

In preparation for submission to Nature

Alexandre Beaulieu[1], Hélène Gaonac'h[1] and Shaun Lovejoy[2]

1- Université du Québec à Montréal – Centre GEOTOP-UQÀM-McGill,
C.P.8888 succursale Centre-Ville, Montréal, Québec, Canada, H3C 3P8.
2-Université McGill, Department of Physics, 3600 University, Montreal,
Québec, Canada, H3A 2T8

The use of remotely sensed images is now widespread to monitor and interpret natural structures such as in geophysics and geology, medical science and meteorology. Statistical quantification of the intrinsic characteristics of these images is vital for comparison and correlation of the involved dynamical processes. In the recent decades, fractal and multifractal techniques involving scale invariance has been developed and widely used to investigate over a large range of scales the different acting processes, from one scale to another, revealed by these fields[1-5]. Scaling analyses usually assume the fields are isotropic - that the fields are self-similar. Since anisotropy is present in most systems, this is inappropriate. Using energy spectra and 2D structure functions of satellite data over differently eroded portion of the Ethiopian Plateau drainage network, in various spectral regions, we investigated the anisotropic properties in the framework of the Generalized Scale Invariance (GSI)[6-9]. Hence, we demonstrate that anisotropy is scale invariant and that it can be characterized by linear GSI. We have also revealed the presence of two interacting processes, mechanical and chemical erosion/deposition, on the Ethiopian Plateau, each demonstrating different anisotropic properties.

Attempts to characterize surfaces, and to assess their intrinsic statistical properties, have been multiplying rapidly in recent years. Natural forms as well as artificial ones, such as topographic surfaces, can be repeatedly magnified, exhibiting morphologies and structures, from planetary topography down to the nanoscale ruggedness of the crystal arrangement of a sand grain. Scale invariant investigation is appropriate to study such surfaces and to quantify the succession of similar observed features from one scale to another. Various methods have been applied in the past to estimate their statistical properties. Some popular analyses are variograms[10,11], Fourier energy spectra[12,13] and functional box-counting[11]. Unfortunately, these methods are usually combined (often implicitly) with isotropic averaging so that any anisotropy is "washed out". This is a serious limitation for surfaces that show structures demonstrating preferential orientations. Such "differential" anisotropy is ubiquitous, it is important to study it. Researches in various domains have been developed to quantify anisotropy and evaluate the underlying properties. For example, in order to gauge the functional behavior of machine wear surfaces, fractal analyses using structure functions were used to investigate surface plane anisotropy[14]. Engineering interest for the assessment of fiber preferential orientation, hence anisotropy, in reinforced concrete, has been raised to better understand its mechanical behavior[15]. In medical science, image analysis becomes important since the major advance in remote sensing technologies and image processing. A method consisting in the estimation of fractal dimension in every direction over a surface has been developed to study bone structures in order to recognize the presence of osteoarthritic in knee joints[16]. Application of this method called the Hurst orientation transform (HOT) gave interesting results on the characterization of anisotropy[17,18].

Research in the fields of geosciences cannot avoid this issue since the Earth's morphologies are made of complex anisotropic structures where anisotropy varies with scale, structures and shapes changing according to their size. Such differential anisotropy may consist in stratification and/or rotation of the structures as already demonstrated for various settings in different investigations[19,20,21]. For example, we may observe small preferentially-oriented fractures which can evolve to larger ones with distinct orientation. This transition from anisotropy at one scale to another may come across an intermediate scale at which the statistics are roughly isotropic, at the sphero-scale (l_s), which is a convenient reference scale. Remotely sensed images provide an excellent opportunity to scrutinize such statistical properties over a large range of scales. Data fields of the Earth's surfaces can be studied in different wavelength regions. Spectral signatures of the surface vary depending on the wavelength investigated; for example, the chemical properties of the top micron-surface would affect images in the visible spectrum (VIS) differently of those acquired in the short-wave infrared (SWIR). In this paper, we investigate the presence of anisotropic scale invariance in satellite images, of two distinct areas, "plateau" and "canyon", within the drainage network of the Ethiopian Plateau with different types of satellite images: Landsat TM 5and TERRA ASTER (Fig. 1). A previous study over the same region revealed the distinct scaling properties of the VIS and SWIR images through power spectra analyses[22]. Fourier (FT) and second order structure function (SF) images on which angle integration as function of radius is performed, are used to investigate the presence of scaling (fig. 2). In the present case, the scaling of the Ethiopian canyon region is present from about 120 m to 15 000 m. However, when investigating the scaling in such a way, the anisotropy is disregarded by the smoothing effect of the isotropic integration, possibly producing a "biased" scaling estimate (Fig. 2). In order to consider the anisotropy of the image, the statistical analyses are produced in the framework of the Generalized Scale Invariance (GSI)[6-9,19-21].

In regular zooming, the statistical properties of a field are evolving over a range of scales in a power-law isotropic way. This transformation can be defined by a scale-changing operator T_λ, which relates the statistical properties from one scale λ to another. T_λ, may be written such as:

$$T_\lambda = \lambda^{-G}$$

where G is a generator that takes the form of the identity matrix for the isotropic case and λ is a scale ratio (see below). In a 2D anisotropic system with linear GSI, where the stratification and rotation of the structures change with scale, G may be written as a generator matrix:

$$G = \begin{pmatrix} d+c & f+e \\ f-e & d-c \end{pmatrix}$$

Where c and f are related to the stratification of the structures, e to the rotation and d to the general contraction (for matter of simplification, d=1, which means no contraction). The general anisotropy describing a system can be summarized by:

$$a^2 = c^2 + f^2 - e^2$$

The parameters c, f and e equal 0 for a surface with isotropic scaling; a^2 determines the qualitative character of the differential anisotropy in a system. If $a^2 > 0$, it is stratification dominant; if $a^2 < 0$, it is rotation dominant[23]. Rotation and stratification can counteract each other giving a^2 values near zero. In this study, we consider linear GSI, i.e., this is valid if the anisotropy depends only on scale, not spatial location. A more exhaustive description of the GSI has been previously presented by other authors[6-9,19-21].

The applied method of this study involves the characterization of elliptic contours that better fit the amplitude of the variations present in the FT and SF images[23]. Both analyses (FT and SF) were used in order to get a strong control on the estimated statistical anisotropic parameters. The contours as exhibited in FT as well as in SF images clearly show the presence of anisotropy in the large structures of the plateau area in the SWIR region compare to the small structures (Fig. 3). Ellipticity may be defined such as:

$$\varepsilon = (A - B)/A$$

where A and B are respectively the long and the small axis of the estimated ellipse. According to the theoretical linear GSI with sphero-scale l_s that predicts a linear relation between the ellipticity ($\zeta(l)$) and the size of the structures (l), we define ellipticity factor $\zeta = \sqrt{\varepsilon/(\varepsilon+1)}$, that can be rewritten such as[7,23]:

$$\zeta = \sqrt{\sqrt{A/B} - \sqrt{B/A}}$$

In stratification dominance, ζ is related to the scale ($\sqrt{AB}$) as[23]:

$$\zeta = \zeta_0 + \zeta_1 \ln l$$

where $\zeta_0 = -\ln l_s (2|a|\sqrt{c^2+f^2})^{1/2}$ and $\zeta_1 = (2|a|\sqrt{c^2+f^2})^{1/2}$. Figure 4 reveals the log-linear behavior between the anisotropy and the scale for all the data. From the graphs, ζ_0 and ζ_1 are extracted as the intercept and the slope respectively, l_s is then calculated as $l_s = e^{-\zeta_0/\zeta_1}$. The observed $\zeta(l)$ values are plotted versus $\ln(l)$ for the "plateau" and "canyon" regions (fig. 4).

The results of the remotely sensed Ethiopian images confirm that we have to consider the anisotropy of the Ethiopian surfaces in such a scale invariant framework. Fits are better for the canyon area because of the amplitude of the variation of the image values from scale to scale (Fig. 4). From the slope and the intercept of these graphs, the values of ζ_1 and l_s, the sphero-scale at which the "ball" is isotropic, are retrieved (fig. 4). A high ζ_1 value, the differential variation of anisotropy with scale, reveals that a stronger anisotropic variation from scale to scale is occurring in the system. FT and SF methods give quite comparable ζ_1 and l_s values. The Ethiopian ASTER data sets also give very similar results than the Landsat images (see figure 4). The predicted l_s values (averaged from the two data set and the FT and SF methods) obtained for both plateau and canyon areas in the VIS range are 30 and 2 meters respectively, whereas in the SWIR range they are 75 and 2 meters respectively. The ζ_1 and l_s values are distinct between the VIS and SWIR regions for the "plateau" while similar in the "canyon". In the VIS image, the topographic aspect is the dominant contributor to the remotely sensed data, whereas in the SWIR image, the chemical composition of the altered surface plays a noticeable role in the production of the reflected surface[22]. Chemical weathering of the basaltic lava produce a lateritic cover rich in clays, particularly kaolinite[24], a mineral to which the SWIR part of the electromagnetic spectrum is very sensible[25,26]. The difference observed between VIS and SWIR images reflects the involvement of different processes (mechanical erosion versus chemical erosion/deposition) acting on the Ethiopian Plateau and producing distinct differential scale invariant anisotropies. In the case of the "canyon", the similarity between ζ_1 in VIS and SWIR is interpreted as dominant mechanical erosion. In the plateau area, where mechanical erosion, even if present, is less intensive, the formation of a chemically altered or leeched crust (a lateritic cover) is possible. The crust remains and forms a structured pattern that provides distinct anisotropic properties for the VIS and SWIR spectrum range. These observations confirm previous isotropic scaling studies on this Ethiopian area[22,27,28]. It is also interesting to note that the estimated statistical parameters β, ζ_1 and l_s from the TERRA ASTER satellite image of the "canyon" area, which is a part of the Blue Nile river network, yielded quite similar values as those observed in a previous study on the Green River system in the Desolation Canyon, Utah with the same satellite. Both areas are in similar environment in a lithological perspective (hard rock settings)[29].

The characterization of anisotropy in a GSI framework has great potential for studying scale invariant anisotropic morphologies and textures and their underlying landscape processes. The anisotropy over the Ethiopian Plateau is scale invariant and exhibits distinct anisotropic characteristics between the "plateau" and "canyon" regions. From our investigation on scale invariant anisotropy, future works may involve to better characterize the structures of these images via the quantification of the amplitude (ζ at fixed scale) and orientation/rotation of the anisotropy. Important considerations will be to more precisely estimate the sphero-scale l_s and ζ_1 values through second or fourth order fitting of $\zeta(x)$ versus the scale ($\ln(x)$) in order to better incorporate them into the GSI framework. Taking into account the similarities of natural structures from one scale to another, but also of their changing anisotropy, is a necessary step forward to the characterization of the Earth landforms and understanding of underlying geoprocesses.

References:

1. Bunde, A. & Havlin, S. (eds.) *Fractals in Science* (Springer-Verlag, Berlin Heidelberg, 1994).
2. Quattrochi, D.A. & Goodchild, M.F. (eds.) Scale in remote sensing and GIS (CRC Lewis Publishers Boca Raton, Fo, 1997).
3. Gaonac'h, H., Lovejoy, S. & Stix, J. Scale invariance of basaltic lava flows and their fractal dimensions. *Geophys. Res. Lett.*, **19, 9**, 785-788 (1992).
4. Lavallée, D., Lovejoy, S., Schertzer, D. & Ladoy, P. Nonlinear variability of Landscape topography: Multifractal analysis and simulation. *Fractals in Geography* (eds De Cola, L. and Lam N.) 158-192 (Prentice-Hall, Englewood Cliffs, NJ, 1993).
5. Schertzer, D. & Lovejoy, S. Physical modeling and analysis of rain and clouds by anisotropic scaling of multiplicative processes. *J. Geophys. Res.*, **92**, 9693-9714 (1987).
6. Lovejoy, S., Schertzer, D. & Pflug, K. Generalized scale invariance and differential rotation in cloud radiances. *Physica A*, **185**, 121-128 (1992).
7. Pflug, K., Lovejoy, S. & Schertzer, D. Differential rotation and cloud texture: analysis using generalized scale invariance. *J. Atmos. Science*, **50**, 538-553 (1993).
8. Pecknold, S., Lovejoy, S. & Schertzer, D. The morphology and texture of anisotropic multifractals using generalized scale invariance. *Stochastic Models in Geosystems* (eds. Woyczynski, W. & Molchansov, S.) 269-312 (Springer-Verlag, New York, 1997)
9. Lewis, G.M., Lovejoy, S., Schertzer, D. & Pecknold, S. The scale invariant generator technique for quantifying anisotropic scale invariance. *Computers & Geosciences*, **25**, 963-978 (1999).
10. Klinkenberg, B. & Goodchild, M.F. The fractal properties of topography: a comparison of methods. *Earth Surface Processes And Landforms*, **17**, 217-234 (1992).
11. Chase, C.G. Fluvial landsculpting and the fractal dimension of topography. *Geomorphology*, **5**, 39-57 (1992)
12. Huang, J. & Turcotte, D.L. Fractal mapping of digitized images: application to the topography of Arizona and comparisons with synthetic images. *J. Geophys. Res.*, **94**, 7491-7495 (1989).
13. Laferrière, A. & Gaonac'h, H. Multifractal properties of visible reflectance fields from basaltic volcanoes. *J. Geophys. Res.*, **104**, **B3**, 5115-5126 (1999).
14. Thomas, T.R., Rosén, B.-G. & Amini, N. Fractal characterisation of the anisotropy of rough surfaces. *Wear*, **232**, 41-50 (1999).
15. Redon, C., Chermant, L., Chermant, J.-L. & Coster, M. Assessment of fibre orientation in reinforced concrete using Fourier image transform. *J. of Microscopy*, **191**, 258-265 (1998).

16. Podsiadlo, P. & Stachowiak, G.W. The development of the modified Hurst transform for the characterization of surfaces topography of wear particles. *Tribology Letters*, **4**, 215-229 (1998).
17. Podsiadlo, P. & Stachowiak, G.W. Applications of Hurst orientation transform to the characterization of surface anisotropy. *Tribology International*, **32**, 387-392 (1999).
18. Podsiadlo, P. & Stachowiak, G.W. Analysis of trabecular bone texture by modified Hurst orientation transform method. *Med. Phys.*, **29**, 460-474 (2002).
19. Pecknold, S., Lovejoy, S., Schertzer, D. and Hooge, C., Multifractals and resolution dependence of remotely sensed data: GSI to GIS, in Scale in Remote Sensing and GIS, edited by Quattrochi, D.A. and Goodchild, M.F., pp. 361-394, Boca Raton, FL, CRC Press, 1997.
20. Lovejoy, S., Pecknold, S. and Schertzer, D., Stratified multifractal magnetization and surface geomagnetic fields-I. Spectral analysis and modelling, Geophys. J. Int., 145, 112-126, 2001.
21. Pecknold, S., Lovejoy, S. and Schertzer, D., Stratified multifractal magnetization and surface geomagnetic fields-II. Multifractal analysis and simulations, Geophys. J. Int., 145, 127-144, 2001.
22. Beaulieu, A. & Gaonac'h, H. Scaling of differentially eroded surfaces in the drainage network of the Ethiopian Plateau. *Remote Sensing of Environment*, **82**, 111-122, 2002.
23. Beaulieu, A., Gaonac'h, H & Lovejoy, S. Scale-invariant anisotropy investigation of remotely sensed images of river networks, submitted to J. Geophys. Res., Surfaces. This thesis, chap2, 2004.
24. Augustithis, S.S. & Vgenopoulos, A. Geochemical and mineralogical studies of the alteration (lateritic) cover of alkali trachy-andesite from the Plateau. Laterisation processes (eds. Chowdhury et al.) 139-143 (Balkema, Rotterdam, Netherlands, 1981).
25. Drury, S.A. & Hunt, G.A. Geological uses of remotely-sensed reflected and emmited data of laterized Archean terrain in Western Australia. *Int. J. Remote Sensing*, **10**, 475-497 (1989).
26. Vitorello, Í. & Galvão, L.S. Spectral properties of geologic materials in the 400- to 2500 nm range: review of application and lithologic mapping. *Photo-Interprétation*, **2**, 1317-1322 (1996).
27. Weissel, J.K., Malinverno, A., Harding, D.J. & Karner, G.D. Erosional development of the Ethiopian Plateau of northeast Africa from a fractal analysis of topography. *Fractals in Petroleum Geology and Earth Processes* (eds C.C. Barton & P.R. La Pointe) 127-142 (Plenum Press, New York, 1995).
28. Weissel, J.K. & Pratson, L.F. The length-scaling properties of topography. *J. Geophys. Res.*, **99**, 13997-14012, 1994.
29. Beaulieu, A, Gaonac'h, H. & Lovejoy, S. Scaling of differentially eroded surfaces in the drainage network of the Ethiopian Plateau. In preparation for *J. Geophys. Res.*, **This Thesis chapter 2**.

Figure captions:

Figure 1: Images chosen, "canyon" and "plateau", on the Landsat TM scene acquired on January 5, 1985, with solar elevation of 42° and azimuth angle of 134°. The scene is a color-composite of bands 3, 4 and 5. The size of subset is 1024 by 1024 pixels, which is about 30 km square. Images chosen on TERRA ASTER scenes, acquired on June 11, 2001, with solar elevation of 60° and azimuth angle of 149°are of the same size and resolution (averaged form initial resolution of 15 meters).

Figure 2: (**a**) The two-dimensional spectral density (FT) of Landsat TM canyon area in the SWIR spectrum range. In this Fourier image, the large structures are represented in the center and are orthogonal to ones in the real space. The graph (**b**) represent the isotropic analysis of the FT, the isotropic energy spectrum log($E(k)$) versus log (k), the slope being β [$E(k) \propto k^{-\beta}$]. In the image, two circles ("balls") are drawn (A and B), their energy density is represented in the graph to demonstrate the scale representation of these isotropic "balls" on which the values are ensemble-average.

Figure 3: Contours drawn on the FT (**a**) and the SF (**b**) images of the Landsat TM plateau area in the SWIR spectrum range. The figure **c** and **d** are the contours drawn in the respective zooms of **a** and **b** (white square). In **a**, only the structures from 30 to 360 meters in size are represented; in **b** the exhibited structures are from 2190 to 12690 meters. The zooms **c** and **d** are

representing respectively the structures 360 to 15360 meters from **a** and 30 to 2190 meters from **b**.

Figure 4: The four diagrams show the variation of ellipticity ($\zeta(l)$) versus the scale/size of the structures $ln(l)$. The values obtained for the extra TERRA ASTER data sets for the canyon area are $\zeta_1 = 0.13, 0.16$ for FT VIS and SWIR and $\zeta_1 = 0.17, 0.15$ for SF VIS and SWIR. The values for the TERRA ASTER plateau area are $\zeta_1 = 0.09, 0.24$ for FT VIS and SWIR and $\zeta_1 = 0.13, 0.22$ for SF VIS and SWIR.

Figure 1

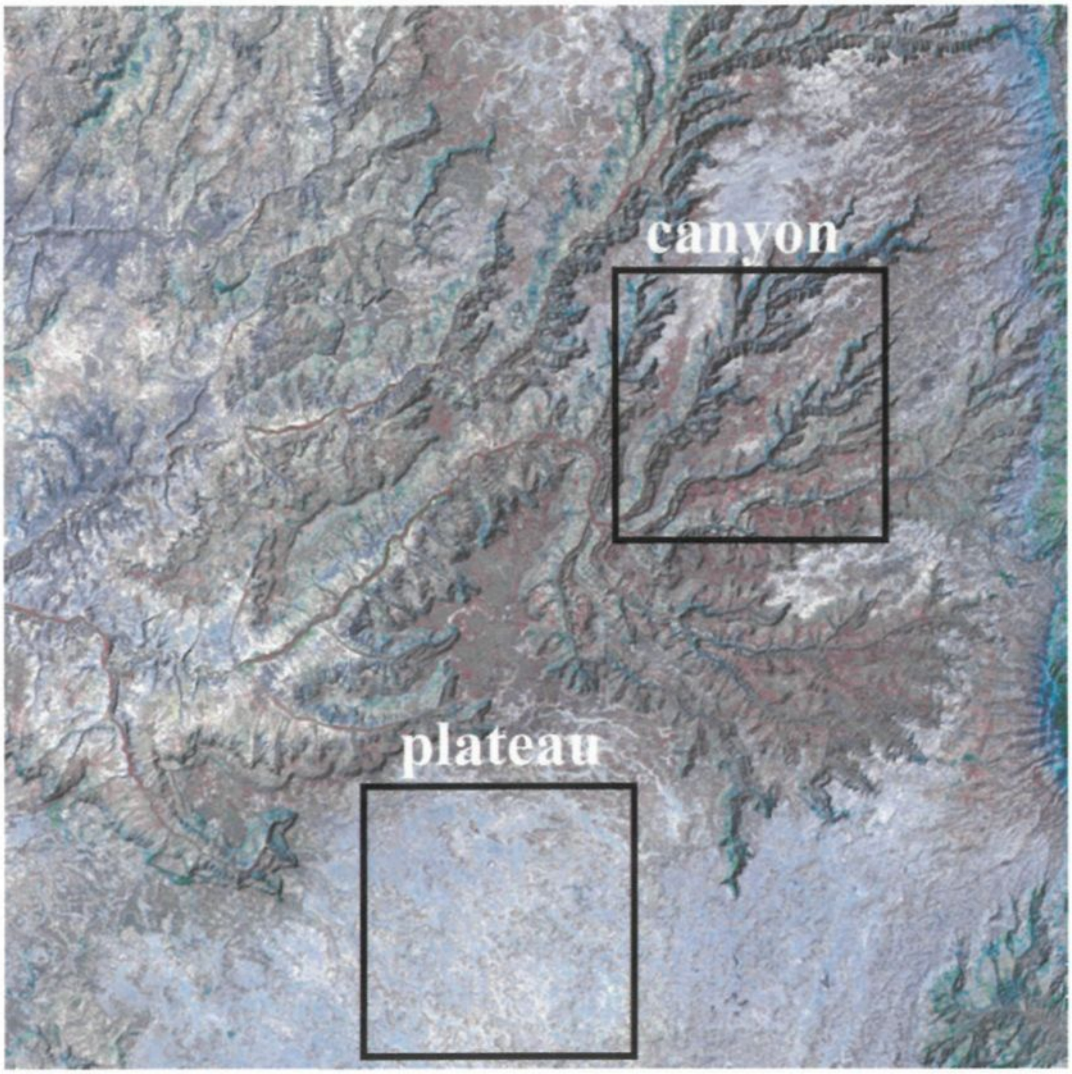

Figure 2

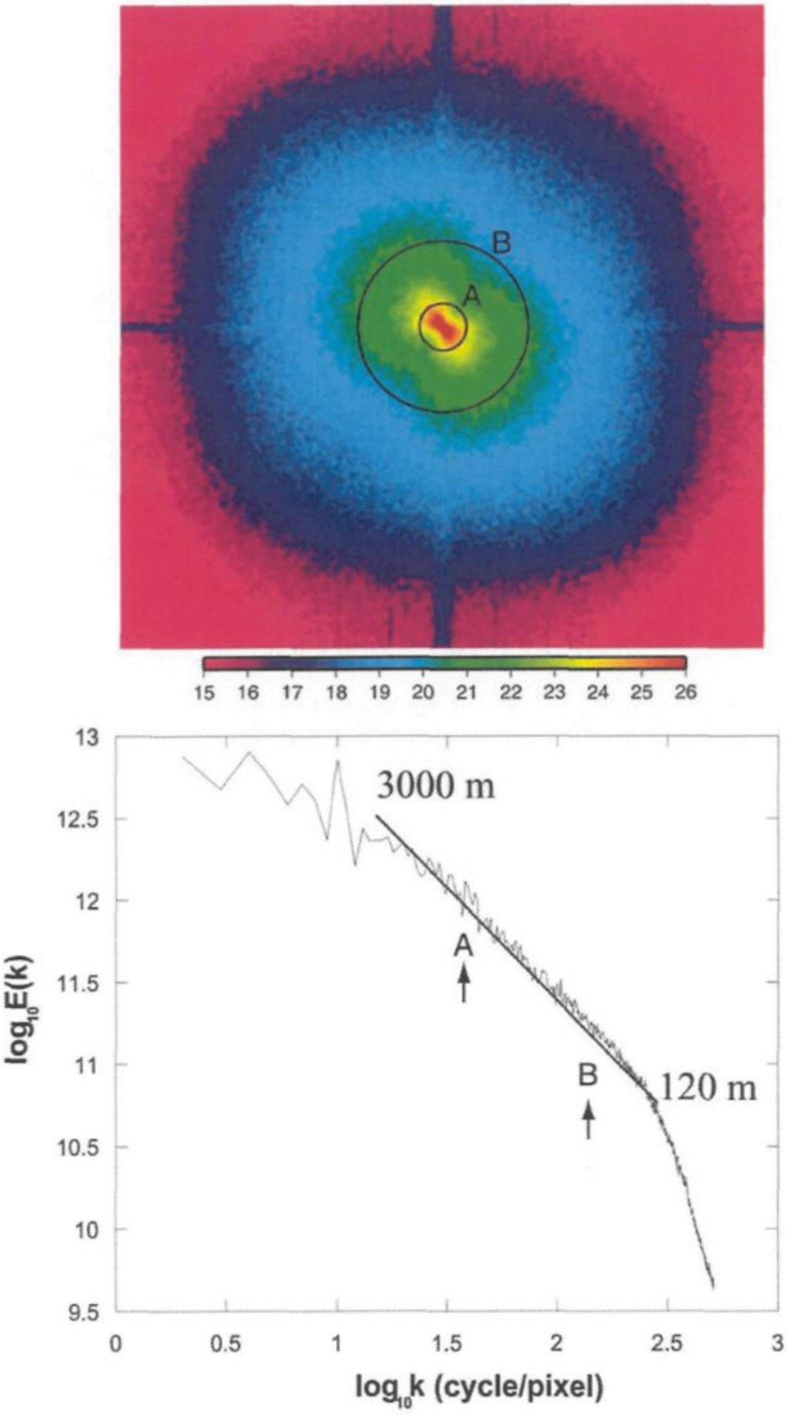
B
A
15 16 17 18 19 20 21 22 23 24 25 26
13
12.5
12
11.5
11
10.5
10
9.5
0
0.5
1
1.5
2
2.5
3
3000 m
A
B
120 m
$\log_{10}E(k)$
$\log_{10}k$ (cycle/pixel)

Figure 3

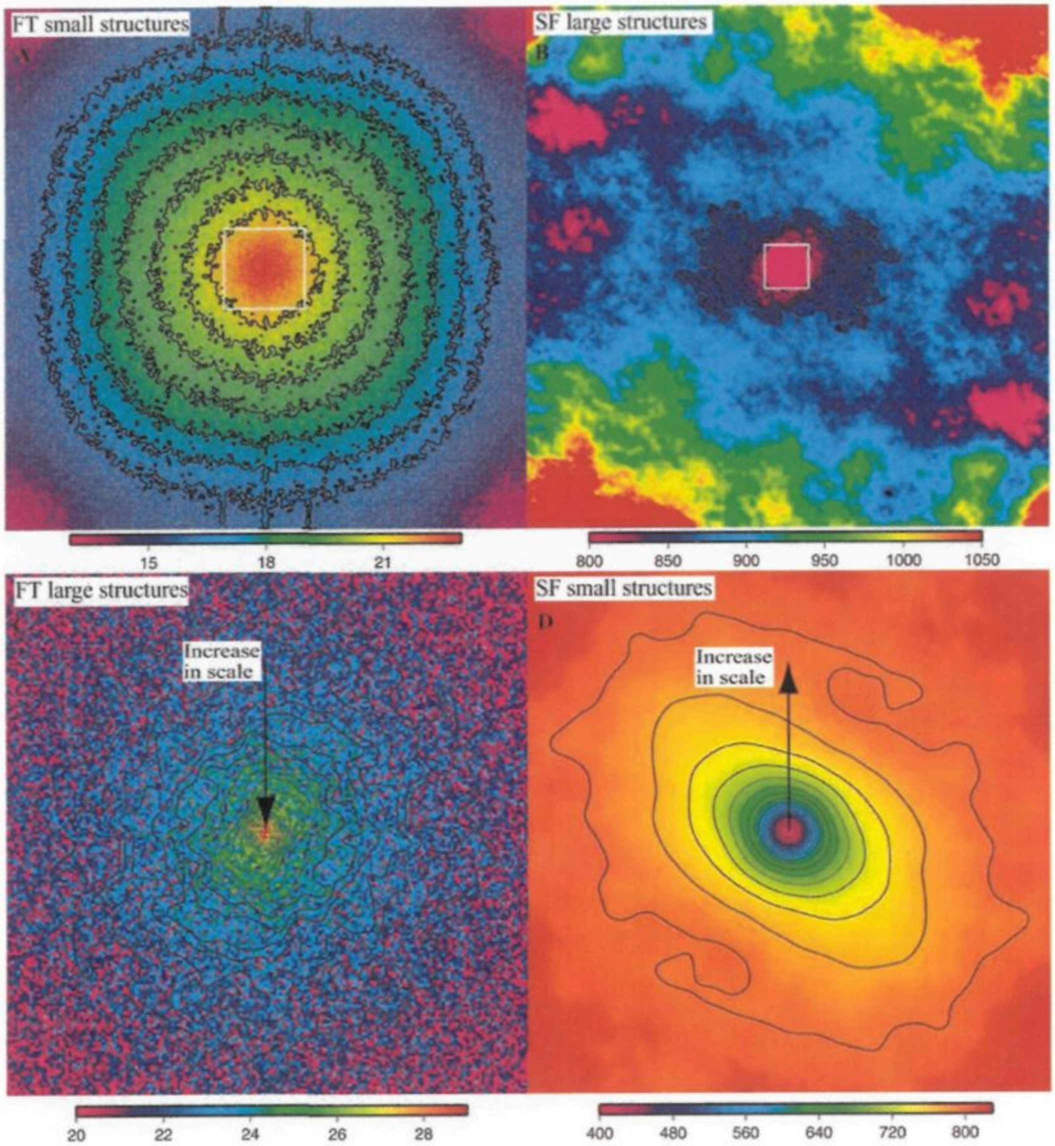
FT small structures
A
SF large structures
B
15
18
21
800
850
900
950
1000
1050
FT large structures
C
Increase in scale
SF small structures
D
Increase in scale
20
22
24
26
28
400
480
560
640
720
800

Figure 4

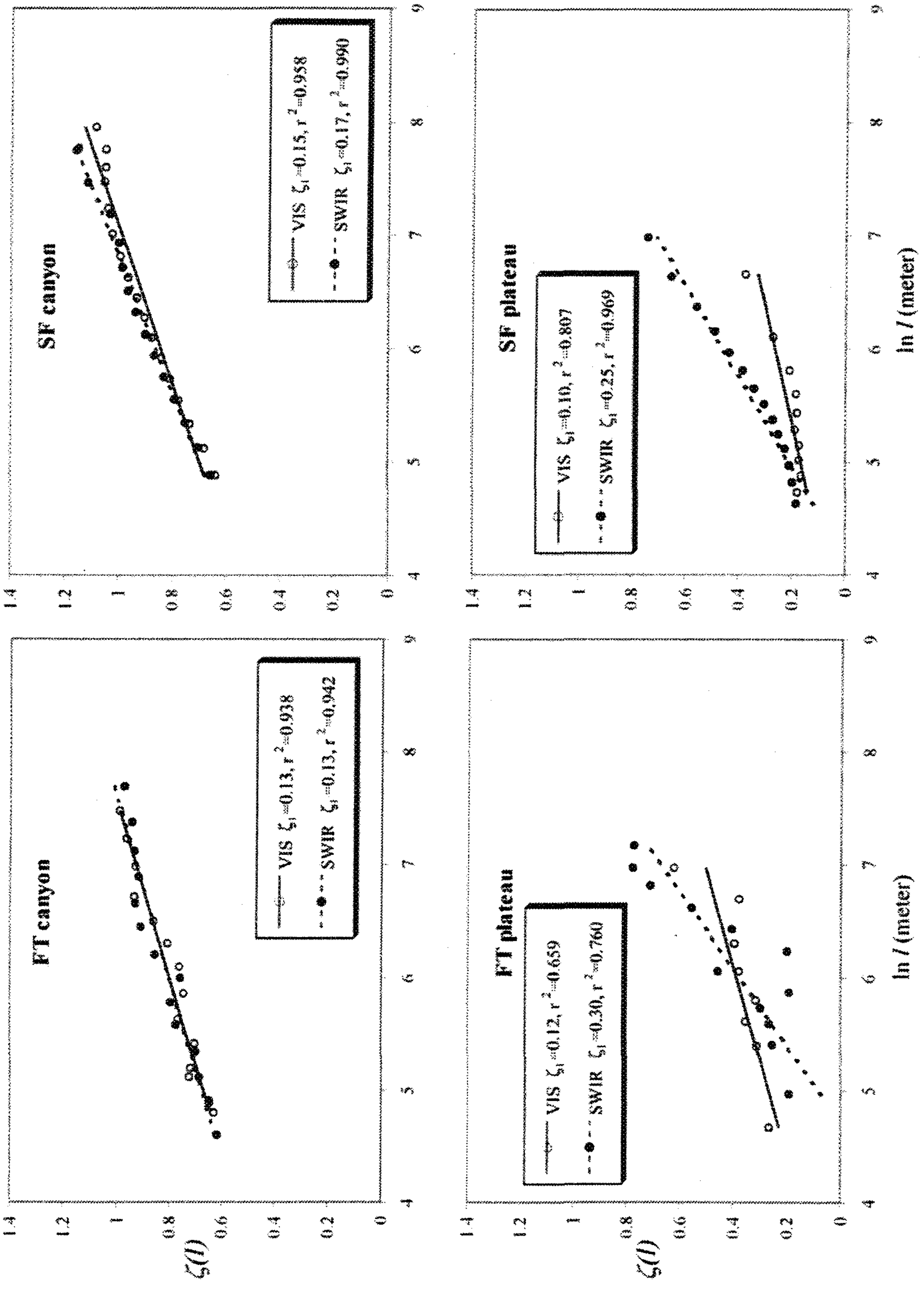
FT canyon
VIS ζ_1 =0.13, r^2 =0.938
SWIR ζ_1 =0.13, r^2 =0.942
SF canyon
VIS ζ_1 =0.15, r^2 =0.958
SWIR ζ_1 =0.17, r^2 =0.990
FT plateau
VIS ζ_1 =0.12, r^2 =0.659
SWIR ζ_1 =0.30, r^2 =0.760
SF plateau
VIS ζ_1 =0.10, r^2 =0.807
SWIR ζ_1 =0.25, r^2 =0.969
$\zeta(l)$
$\zeta(l)$
1.4
1.2
1
0.8
0.6
0.4
0.2
0
4
5
6
7
8
9
ln l (meter)
ln l (meter)

Conclusions générales

L'utilisation d'images satellitaires pour l'étude des surfaces terrestres et des phénomènes naturels devient de plus en plus incontournable. Ces images sont très diverses, allant de basses résolutions (e.g., TERRA MODIS, 1 km), à des hautes résolutions (e.g., TERRA ASTER, 15 m). La quantité de données fournies par les satellites est immense et représente un défi quant au classement, à la caractérisation, et à l'intégration de toutes les informations disponibles. La nécessité de développer des moyens pour faciliter l'analyse de ces images est pressante. La grande variété de morphologies et des phénomènes associés est observée sur la surface de la Terre sur une gamme d'échelles étendue, pouvant aller au moins du millimètre à plusieurs milliers de kilomètres.

Les analyses statistiques incorporant une approche invariante d'échelle, donc indépendantes de l'échelle d'observation, se prêtent bien à la caractérisation de la variabilité observée et sont bien adaptées à l'étude de champs de données télédétectées. Elles permettent de mieux caractériser les propriétés statistiques des différentes surfaces analysées d'une échelle à une autre. La connaissance de ces propriétés nous permet de mieux expliquer l'évolution des mécanismes sous-jacents.

Dans cette étude, nous avons montré que les variations des propriétés invariantes d'échelle isotrope calculées à partir des spectres de puissance (β), particulièrement dans la région du visible, sont associées à la densité du réseau de drainage. La valeur de β étant liée à la distribution relative des grandes et petites structures, un réseau très dense présentant des fines structures remplissant l'espace démontrera un β plus faible. À l'inverse, une image de réseau de drainage présentant une dominance de grandes structures par rapport aux petites, telles que des rivières majeures, aura un β plus élevé. Ainsi, nous suggérons que le β est relié au degré d'érosion d'un réseau de drainage, ou d'une partie de ce réseau. Cependant, nous avons observé que dans certains cas, les propriétés invariantes d'échelle isotrope ne permettent pas de distinguer des réseaux présentant morphologies distinctes, telles que certaines portions du réseau de drainage du Plateau de Loess en Chine et de celui de Desolation Canyon dans l'Utah. Dans ces situations, la méthode de l'anisotropie invariante d'échelle est particulièrement pertinente à utiliser. Nous avons observé dans le spectre du visible une association entre les variations de l'anisotropie invariante d'échelle et le degré de maturité du réseau de drainage. Ceci nous a permis de distinguer adéquatement les portions du réseau Chinois entre-elles, les plus développées présentant des variations plus élevées de l'anisotropie avec l'échelle. Enfin, les variations d'anisotropie à une échelle donnée dans le visible nous permis de distinguer les réseaux de l'Utah et la Chine et de mettre ainsi en valeur les différences de tectonique régionale de ces deux régions.

Si l'on considère maintenant la variation des propriétés statistiques en fonction des longueurs d'ondes spectrales pour une même surface terrestre, des similitudes, ou au contraire des divergences de propriétés sont observées selon le types ou le degré d'érosion présent. Grâce aux propriétés statistiques obtenues des images satellitaires, les variations topographiques ou plutôt les variations minéralogiques des images seront révélées.

Les propriétés invariantes d’échelle des surfaces ont été observées sur une gamme d'échelles allant de 120 m à 15 360 m pour le réseau éthiopien et allant de 240 m à 3840 m pour les réseaux de Chine et de l'Utah. Une recherche de l’anisotropie sur des données acquises à des résolutions plus grandes (inférieures à 120 m) ou plus petites (supérieures à 15 km) sera nécessaire pour trouver les limites des gammes d'échelle des processus d'érosion anisotropes. L'utilisation d'autres types d'images, telles que des données radar, serait intéressante du point de vue des champs de données étudiés. Effectivement, une image dans le visible ou l'infrarouge procure des informations reliées à la réflexion solaire ou à l’émission des surfaces observées. Quant à elle, une image radar produit des données issues de la rétrodiffusion du signal radar. Ceci a pour résultats de créer des images surtout reliées à l'élévation et incluant une composante directionnelle importante associée à la direction préférentielle des structures (les structures orientées parallèlement à la direction du faisceau seront peu observées). Les distinctions entre les statistiques des images radar et visible ont été abordées de façon sommaire dans le premier chapitre. Cependant, il y aurait avantage à poursuivre cette étude plus en profondeur.

Dans la présente recherche, nous interprétons l'anisotropie dans le cadre du GSI linéaire (Generalized Scale Invariance, Schertzer and Lovejoy, 1985 et Lovejoy and Schertzer, 1985). Hors, l'anisotropie invariante d'échelle peut varier dans l’espace. L'aspect non linéaire des variations anisotropes des structures devra être envisagé. Il serait également pertinent de mieux comprendre les effets des manipulations statistiques effectuées régulièrement sur les champs de données tels que le lissage ou la soustraction de tendance moyenne ("detrend") sur un système possédant de l'anisotropie invariante d'échelle.

Les résultats statistiques actuels nous ont permis de suggérer l'existence de processus distincts agissant sur une gamme d'échelles et expliquant les morphologies observées. Dans son étude sur la modélisation et l'analyse de l'aspect géométrique de réseaux fluviatiles, Pelletier (1999) montre qu'il ne trouve pas de différences statistiques entre plusieurs réseaux analysés. L'usage d'images satellitaires et d'analyses statistiques du GSI sur des champs de données plutôt que des ensembles géométriques nous a permis au contraire de trouver des distinctions entre les réseaux en combinant leur aspect d'invariance d'échelle à leur caractère anisotrope. Les informations contenues dans une image satellitaire nous permettent de valoriser différentes propriétés d'une même morphologie. En effet, l'information contenue dans chaque bande spectrale est la projection d'une surface différente reliée à la signature spectrale des objets observés. Par exemple, la végétation réfléchit fortement le rayonnement solaire dans le proche infrarouge et fournit ainsi une image très différente de la même surface observée dans le visible.

La recherche effectuée dans cette thèse a permis de répondre à plusieurs questions sur l'existence de l'anisotropie invariante d'échelle. Nous avons aussi développé une méthode statistique pour caractériser cette propriété qui nous a permis d'obtenir les premiers résultats d'invariance d'échelle anisotrope sur des réseaux de drainage dans des régions spectrales différentes. L'utilisation des nouveaux paramètres statistiques de l'anisotropie nous a permis de quantifier des observations qualitatives de morphologies. Cette étude ouvre la voie à plusieurs avenues de recherche sur les propriétés statistiques de champs de données anisotropes.

Références

Lovejoy, S. and Schertzer, D., Generalized scale invariance in the atmosphere and fractal models of rain, Water Ressources Res., 21, 1233-1250, 1985.

Pelletier, J.D., Self-organisation and scaling relationships of evolving river networks, J. Geophys. Res., 104, 7395-7375, 1999.

Schertzer, D. and Lovejoy, S., Generalised scale invariance in turbulent phenomena, Phys. Chem. Hydrodyn. J., 6, 623-635, 1985.

APPENDICE A

MÉTHODOLOGIE POUR LA CARACTÉRISATION DE L'ANISOTROPIE INVARIANTE D'ÉCHELLE

1- Pour caractériser l'anisotropie invariante d'échelle on doit tout d'abord utiliser une représentation de l'image soit en Fourier ($P(k)$) soit en fonction de structure ($S_q(l)$) (voir le chapitre 2). Plusieurs logiciels permettent de produire des représentations en Fourier (matlab, mathematica, FORTRAN, etc.). Pour la représentation en fonction de structures, nous fournissons un programme en appendice B sur CD-ROM.

2- À partir de ces représentations, il est possible de tracer des contours fermés de taille variable autour du centre de l'image. Pour ce faire, on peut encore utiliser plusieurs logiciels tels que matlab ou mathematica. Dans la présente étude, deux méthodes différentes ont été employées. La première a consisté à utiliser le logiciel GMT sur UNIX pour créer les contours, puis ImageJ (http://rsb.info.nih.gov/ij/), logiciel gratuit, pour l'évaluation de l'ellipticité de chaque contour. Cependant, une routine de ImageJ, IsoPhotContour produite par Gabriel Landini (http://www.dentistry.bham.ac.uk/landinig/software/software.html), permet de tracer les contours fermés directement dans ImageJ, on peut ainsi sauver plusieurs manipulations. On obtient de cette opération les grand (A) et petit (B) axes de l'ellipse qui approximent le mieux le contour ainsi que l'angle de cette ellipse.

3- Les résultats de l'évaluation de l'ellipticité des contours dans chaque représentation sont ensuite compilés dans un tableur (excel) et les équations du GSI (voir chapitre 2) y sont appliquées.

- L'échelle spatiale pour chaque contour est calculée en Fourier ($P(k)$):

  l = (Taille de la représentation $P(k)$/racine carré(grand axe * petit axe))*resolution de l'image, exemple: $(1024/(A*B)^{0.5})*30$ mètres.

- Pour les fonctions de structures, elle est calculée de cette façon:

  l = Racine carré(grand axe/2 * petit axe/2)*resolution de l'image, exemple: $((A/2*B/2)^{0.5})*30$ mètres.

- L'ellipticité est dans les deux cas (Fourier et fonction de structures) calculée selon:

  Racine carré(racine carré(B/A) –racine carré(A/B)), voir chapitre 2.

4- Un graphique de l'ellipticité de chaque contour en fonction du log népérien de l'échelle est produit et nous permet d'estimer les variations d'anisotropie et de rotation de l'anisotropie avec l'échelle. À partir de ce graphique, les paramètres invariants d'échelle ζ_1, θ_1 et l_s sont recueillis. On peut aussi évaluer l'anisotropie à une échelle fixe ($\zeta(l)$) (voir chapitre 2 pour plus de détail).

APPENDICE B

FICHIERS SUR LE CD-ROM

Les fichiers sur le CD-ROM sont classés comme suit:

Premièrement en trois chapitres, ensuite les programmes principaux en fortran et enfin les noms des images satellites choisies pour chaque chapitre.

Le dossier Chapitre1 comprend les images et les analyses diverses effectuées (fractales et multifractales) sur le Plateau Éthiopien. La nomenclature est basée sur le nom des images choisies, da, db et pla, qui correspondent respectivement à BNC, BNS et PLA dans les articles 1 et 3. Le dossier d'analyse appelé «Landsat-subimages» contient les analyses des images da, db et pla divisées en 16 images plus petites utilisées pour la figure 6 du chapitre 1 (chaque image de 1024 par 1024 pixels a été divisée en 16 images 256 par 256 pixels puis analysée).

Le dossier Chapitre2 comprend les images et les analyses d'invariance d'échelle isotropes et anisotropes et les résultats des calculs pour divers réseaux fluviaux. La nomenclature est basée sur le numéro des fichiers (1 à 96) et est expliquée dans le fichier «nomenclature» dans le dossier Chapitre2, les images choisies pour les interprétations y sont aussi indiquées.

Le dossier Chapitre3 comprend les images et les analyses d'invariance d'échelle anisotropes effectuées sur le Plateau Éthiopien. La nomenclature est similaire à celle du Chapitre1.

GLOSSAIRE

Anisotropie (anisotropique, anisotrope): Qualité d'un milieu dont les propriétés varient suivant la direction selon laquelle on les évalue.

Note(s): À la différence des substances vitreuses, les cristaux sont anisotropes pour l'ensemble, ou au moins pour une partie, de leur propriétés. L'anisotropie est dite continue, si le paramètre considéré varie progressivement selon la direction, toutes les valeurs intermédiaires existant entre une valeur maximale et une valeur minimale; c'est p. ex. le cas de l'indice de réfraction des cristaux, excepté ceux du système cubique qui sont isotropes. L'anisotropie est dite discontinue dans le cas contraire, p. ex. celui du développement des faces et des plans de clivage des cristaux, qui a lieu selon des orientations bien définies, les positions intermédiaires n'existant pas.

Antonyme : isotropie.

Du gr. anisos, inégal, et tropos, tour, de trepein, tourner.

Ainsi, certains milieux transparents ont des indices de réfraction différents suivant l'orientation de la vibration lumineuse (c'est le cas de divers cristaux). Il peut en résulter un dédoublement des faisceaux dont des images.

Provenance:

http://www.granddictionnaire.com/btml/fra/r_motclef/index1024_1.asp

Anisotropie invariante d'échelle: Propriété qui relie les transformations anisotropes que subissent les objets mathématiques ou physiques avec l'échelle.

Autoaffine (autoaffinité): Propriété d'un objet fractal complexe subissant une transformation affine où les coordonnées évoluent différemment selon les directions (aplatissement, allongement)

Autosimilaire (autosimilarité): Propriété d'un objet fractal complexe subissant une même transformation dans toutes les directions. L'objet a les mêmes propriétés (ou forme) à toutes les échelles.

Dimension fractale: Nombre qui sert à quantifier le degré d'irrégularité et de fragmentation d'un ensemble géométrique, d'un objet naturel ou d'un système dynamique. Ce nombre, qui mesure la manière dont ces entités remplissent l'espace dans lequel elles se trouvent, n'est pas nécessairement un entier. NOTA Par exemple, la dimension des courbes de Koch est D = 1,26..., celle des nuages varie entre 2,2 et 2,3, celle des montagnes se trouve entre 2,1 et 2,3. Il existe plusieurs définitions de la dimension fractale qui ne sont pas formellement équivalentes et qui conduisent à des valeurs numériques différentes aussi bien du point de vue mathématique que pour des cas concrets. Certaines définitions soulignent la connectivité intrinsèque d'un objet (dimension d'étalement, ou chimique), d'autres considèrent plutôt la façon dont l'objet emplit l'espace ambiant (dimension d'empilement, de tortuosité, dimension spectrale). Les recherches en cours étudient des aspects très importants pour la description des systèmes dynamiques tels l'élasticité sous déformation et l'intermittence. D'autre part, il existe déjà des méthodes très simples pour construire des lignes, des surfaces et des volumes à dimension fractale.

Provenance: www.translationbureau.gc.ca/pwgsc_internet/fr/publications/documents/fractal.pdf

Invariance d'échelle (scaling): Propriété des objets mathématiques et physiques de rester inchangés lors de transformations des grandeurs d'échelle.

NOTA C'est une invariance d'homothétie : les parties de l'objet restent semblables à l'ensemble sous une transformation par dilatation, contraction ou translation. Ainsi, les équations des systèmes dynamiques sont invariantes par translation dans le temps.

Provenance: www.translationbureau.gc.ca/pwgsc_internet/fr/publications/documents/fractal.pdf

Invariance d'échelle généralisée (GSI): Théorie selon laquelle les transformations d'échelle d'un système prennent en considération les variations anisotropes avec l'échelle.

Isotrope (isotropie): Qualifie un corps qui possède les mêmes propriétés physiques et mécaniques dans toutes les directions, par exemple l'acier.

Provenance:

http://www.granddictionnaire.com/btml/fra/r_motclef/index1024_1.asp

Multifractal (multiscaling, multifractalité): Existence d'une hiérarchie de singularités et de dimensions fractales.

Orientation préférentielle: Caractéristique relative à la dimension, la forme, la disposition des formes et des objets dans un ensemble. Dans les matériaux, l'orientation préférentielle est une cause d'anisotropie et peut être produite par un travail mécanique (laminage, filage, étirage, etc.). Par exemple, l'orientation préférentielle des cristaux dans une roche produit l'anisotropie.

Rotation différentielle: Rotation des structures (formes, textures, objets) d'un système qui varie en fonction de l'échelle. Par exemple, les petites structures subissent une rotation plus forte que les grandes structures. L'orientation préférentielle des structures est différente selon la taille des objets.

Sphéro-échelle: Échelle dans un système à laquelle les formes, textures, objets ou structures ont des propriétés isotropes.

Stratification différentielle: Stratification ou aplatissement des structures (formes, textures, objets) d'un système qui varie en proportion avec l'échelle. Par exemple, les petites structures subissent une stratification plus forte que les grandes structures. L'aplatissement des structures est différent selon la taille des objets.